Non-invasive Profiling of Molecular Markers in Brain Gliomas using Deep Learning and Magnetic Resonance Images

by

Chandan Ganesh Bangalore Yogananda

Presented to the Faculty of the Graduate School of

The University of Texas at Arlington

in Partial Fulfillment of the Requirements for the Degree of

DOCTOR OF PHILOSOPHY

THE UNIVERSITY OF TEXAS AT ARLINGTON

May 2021

Acknowledgements

Throughout the writing of this dissertation, I have received a great deal of support and assistance.

First and foremost, I would like to thank my advisors Prof. Joseph A Maldjian and Prof. Hanli Liu for their continuous support throughout my Ph.D. study and related research, for their patience, motivation, and immense knowledge. Their guidance has helped me at all the times of research and writing of this dissertation. Their professional guidance and powerful encouragement has made my dissertation even possible. I could not have imagined having better advisors and mentors for my Ph.D. study.

Besides my advisors, I would like to sincerely thank the rest of my committee members including Dr. Ananth J Madhuranthakam, and Dr. Baowei Fei for believing in me and guiding me with their insightful comments and encouragement throughout my Ph.D. journey. I would also like to thank their hard questions which incented me to widen my research from various perspectives. I appreciate all my committee members for their willingness to be on my doctoral committee.

Furthermore, I would especially like to thank Drs. Shah, Yu, Pinho, Patel, Mickey, and Vejdani-Jahromi for helping me combine a medical problem with engineering solutions. Their professional experience and knowledge has guided me in finding an optimized path to reach the goal in research.

On top of that, I would like to express my appreciation to my colleagues Benjamin C Wagner, Dr. Gowtham Krishnan Murugesan, Dr. Elizabeth Davenport, Sahil S Nalawade, and Dr. Yin Xi for providing me with a lot of useful ideas and suggestions in data analysis and manuscript writing. Benjamin, Sahil and Dr. Murugesan have always extended their hands in my need, introduced me to new data analysis techniques, new algorithms, and debugging a code for better data interpretation. While Dr. Xi and Sahil helped me with statistical analysis, Dr. Murugesan provided me with the initial help in understanding clinical problems and using standardized deep learning approaches for medical data analysis.

Apart from those aforementioned, I thank my past and current lab colleagues Dr. Xinlong Wang, Dr. Yudhajith Das, Divya Reddy, James Holcomb, Ryan Fisicaro, Jason Bowerman, and Asim Hassan for sharing their experience with me without any reservation.

Last but not the least, I would like to thank my mom, dad, brother, sister, brother-in-law, my coach, grandparents, my uncle & his family, and my friends for their constant emotional support that has kept me going to solve challenging problems during every day and night!

May 13, 2021.

Abstract

Non-invasive Profiling of Molecular Markers in Brain Gliomas using Deep Learning and Magnetic Resonance Images

Chandan Ganesh Bangalore Yogananda, Ph.D.

The University of Texas at Arlington, 2021

Supervising Professors: Dr. Joseph A. Maldjian & Dr. Hanli Liu

Gliomas account for the most common malignant primary brain tumors in both pediatric and adult populations. They arise from glial cells and are divided into low grade and high-grade gliomas with significant differences in patient survival. Patients with aggressive high-grade gliomas have life expectancies of less than 2 years. Glioblastoma (GBM) are aggressive brain tumors classified by the world health organization (WHO) as stage IV brain cancer. The overall survival for GBM patients is poor and is in the range of 12 to 15 months. These tumors are typically treated by surgery, followed by radiotherapy and chemotherapy.

Gliomas often consist of active tumor tissue, necrotic tissue, and surrounding edema. Magnetic Resonance Imaging (MRI) is the most commonly used modality to assess brain tumors because of its superior soft tissue contrast. MRI tumor segmentation is used to identify the subcomponents as enhancing, necrotic or edematous tissue. Due to the heterogeneity and tissue relaxation differences in these subcomponents, multi-parametric (or multi-contrast) MRI is often used for accurate segmentation. Manual brain tumor segmentation is a challenging and tedious task for human experts due to the variability of tumor appearance, unclear borders of the tumor and the need to evaluate multiple MR images with different contrasts simultaneously. In addition, manual

segmentation is often prone to significant intra- and inter-rater variability. To address these issues, Chapter 2 of my dissertation aims at designing and developing a highly accurate, 3D Dense-Unet Convolutional Neural Network (CNN) for segmenting brain tumors into subcomponents that can easily be incorporated into a clinical workflow.

Primary brain tumors demonstrate broad variations in imaging features, response to therapy, and prognosis. It has become evident that this heterogeneity is associated with specific molecular and genetic profiles. For example, isocitrate dehydrogenase 1 and 2 (IDH 1/2) mutated gliomas demonstrate increased survival compared to wild-type gliomas with the same histologic grade. Identification of the IDH mutation status as a marker for therapy and prognosis is considered one of the most important recent discoveries in brain glioma biology. Additionally, 1p/19q co-deletion and O6-methyl guanine-DNA methyltransferase (MGMT) promoter methylation is associated with differences in response to specific chemoradiation regimens. Currently, the only reliable way of determining a molecular marker is by obtaining glioma tissue either via an invasive brain biopsy or following open surgical resection. Although the molecular profiling of gliomas is now a routine part of the evaluation of specimens obtained at biopsy or tumor resection, it would be helpful to have this information prior to surgery. In some cases, the information would aid in planning the extent of tumor resection. In others, for tumors in locations where resection is not possible, and the risk of a biopsy is high, accurate delineation of the molecular and genetic profile of the tumor might be used to guide empiric treatment with radiation and/or chemotherapy. The ability to non-invasively profile these molecular markers using only T2w MRI has significant implications in determining therapy, predicting prognosis, and feasible clinical translation. Thus, Chapters 3, 4 and 5 of my dissertation focuses on developing and evaluating deep learning algorithms for non-invasive profiling of molecular markers in brain gliomas using T2w MRI only. This includes

developing highly accurate fully automated deep learning networks for, (i) classification of IDH mutation status (Chapter 3), (ii) classification of 1p/19q co-deletion status (Chapter 4), and (iii) classification of MGMT promoter status in Brain Gliomas (Chapter 5).

An important caveat of using MRI is the effects of degradation on the images, such as motion artifact, and in turn, on the performance of deep learning-based algorithms. Motion artifacts are an especially pervasive source of MR image quality degradation and can be due to gross patient movements, as well as cardiac and respiratory motion. In clinical practice, these artifacts can interfere with diagnostic interpretation, necessitating repeat imaging. The effect of motion artifacts on medical images and deep learning based molecular profiling algorithms has not been studied systematically. It is likely that motion corruption will also lead to reduced performance of deep-learning algorithms in classifying brain tumor images.

Deep learning based brain tumor segmentation and molecular profiling algorithms generally perform well only on specific datasets. Clinical translation of such algorithms has the potential to reduce interobserver variability, and improve planning for radiation therapy, improve speed & response to therapy. Although these algorithms perform very well on several publicly available datasets, their generalization to clinical datasets or tasks have been poor, preventing easy clinical translation. Thus, Chapter 6 of my dissertation focuses on evaluating the performance of the molecular profiling algorithms on motion corrupted, motion corrected and clinical T2w MRI. This includes, (i) evaluating the effect of motion corruption on the molecular profiling algorithms, (ii) determining if deep learning-based motion correction can recover the performance of these algorithms to levels similar to non-corrupted images, and (iii) evaluating the performance of these algorithms on clinical T2w MRI before & after motion correction. This chapter is an investigation on the effects of induced motion artifact on deep learning-based molecular classification, and the

relative importance of robust correction methods in recovering the accuracies for potential clinical applicability.

Deep-learning studies typically require a very large amount of data to achieve good performance. The number of subjects available from the TCIA database is relatively small when compared to the sample sizes typically required for deep learning. Despite this caveat, the data are representative of real-world clinical experience, with multiparametric MR images from multiple institutions, and represents one of the largest publicly available brain tumor databases. Additionally, the acquisition parameters and imaging vendor platforms are diverse across the imaging centers contributing data to TCIA. This study provides a framework for training, evaluating, and benchmarking any new artifact-correction architectures for potential insertion into a workflow. Although our results show promise for expeditious clinical translation, it will be essential to train and validate the algorithms using additional independent datasets. Thus, Chapter 7 of my dissertation discusses the limitations and possible future directions for this work.

Table of Contents

List of Illustrations

List of Tables

Chapter 1

Introduction

1.1. Brain Gliomas & Magnetic Resonance Imaging (MRI)

Gliomas are the most common primary brain malignancy and represent a heterogenous set of tumors.[1] They arise from glial cells and are classically divided into high-grade and low-grade tumors based on their histopathology, genetic subtyping, and immunohistochemistry.[1] Magnetic Resonance (MR) imaging is the most commonly used modality to assess brain tumors because of its superior soft tissue contrast.[2] It is routinely used in the clinical work-up of patients for brain tumor diagnosis, monitoring progression and treatment planning. Each MR imaging contrast provides specific information about different tissue sub-components of gliomas.[2] For example, T1-weighted images with intravenous contrast highlight the most vascular regions of the tumor, called 'enhancing tumor', along with the 'tumor core' that does not involve peri-tumoral edema. Conventional T2-weighted (T2W) and T2W-Fluid Attenuation Inversion Recovery (FLAIR) images are used to evaluate the tumor and peri-tumoral edema together defined as the 'whole tumor'.[2,3] Due to heterogeneity and tissue relaxation differences in these subcomponents, multi-parametric (multi-contrast) MR images are often used simultaneously for precise segmentation.[4] Accurate image-based segmentation depends significantly on the ability to differentiate MRI signal of these subcomponents. Current MR image segmentation of gliomas is largely based on imaging correlates of histopathologic findings.[1] MR images often contain complex imaging features and patterns making manual evaluation tedious and a time intensive task requiring a human expert to delineate components.[1] As a result, manual tumor segmentation is often fraught with intra-rater and inter-rater variability, resulting in imprecise boundary demarcation.[5,6] An intra-

rater variability of 20% and an inter-rater variability of 28% has been reported for manual segmentation of brain tumors.[3,7]

1.2. Genetic subtyping and molecular profiling

Genetic subtyping and molecular profiling of gliomas have revolutionized the ability to determine optimal therapy and various strategies to enhance prognostic accuracy.[8] The most compelling evidence supporting this paradigm is the 2016 revision of the World Health Organization's (WHO) classification of gliomas.[9] The glioma reclassification based on molecular profiling has subsequently been studied and three genetic alterations have been extensively validated: Isocitrate dehydrogenase (IDH) mutation status, 1p/19q co-deletion status and methylation status of O-6-methylguanine-DNA methyltransferase (MGMT) promoter.[10] Identifying these statuses as important markers for therapy & prognosis has been a major discovery in brain glioma biology.[8] Currently, the only reliable way to profile a molecular marker requires the analysis of a glioma tissue obtained either via an invasive brain biopsy or following open surgical resection.[11] A major limitation to the current approach is a brain glioma that is inaccessible for biopsy or resection due to a high risk of severe post-operative complications and impairment.[11]

1.3. Deep Learning in Medical Imaging

Recent advances in deep learning have achieved great success in several applications including brain tumor segmentation.[12,13] This has led to a significant interest in advancing deep learning techniques for non-invasive, image-based molecular profiling of brain gliomas as well.[8] The goal of this study is to develop and evaluate advanced deep learning algorithms that use MR images for (a) multi-class brain tumor segmentation and (b) non-invasive profiling of molecular markers in brain gliomas. Clinical implementation of brain tumor segmentation and non-invasive molecular profiling has significant implications in determining therapy and predicting prognosis.[11] This

represents an important milestone towards using deep learning and MR images to predict glioma histology, prognosis, and appropriate treatment. Thus, developing deep learning algorithms for automatic feature extraction and segmentation has the potential to analyze large datasets while exploring important and meaningful insights to impact treatment decisions and patient care beyond the realm of research.

1.4. Rationale of This Thesis

One of the most important recent discoveries in brain glioma biology has been the use of molecular profiling as markers for therapy and prognosis. 1p/19q co-deletion status is the defining genomic marker for oligodendrogliomas and confers a better prognosis and treatment response than gliomas without it. Similarly, the IDH mutated form of a gene confers a better prognosis and treatment response than gliomas with the non-mutated or IDH wild-type form. Methylation of the O6-Methylguanine-DNA Methyltransferase (MGMT) promoter results in epigenetic silencing of the MGMT enzyme and confers improved prognosis and treatment response in gliomas. Currently, the only reliable way of determining the molecular profile requires analysis of glioma tissue obtained either via an invasive brain biopsy or following open surgical resection. The ability to non-invasively profile the molecular markers has significant implications in determining therapy and predicting prognosis.

The first aim was to design, develop & evaluate a deep learning algorithm for multi-class brain tumor segmentation using MR Images. The second aim was to design, develop & evaluate deep learning algorithms for non-invasive profiling of molecular markers in brain gliomas. This second aim of developing highly accurate fully automated deep learning networks has three parts including, (i) classification of IDH mutation status in Brain Gliomas, (ii) classification of 1p/19q co-deletion status in Brain Gliomas, and (iii) classification of MGMT promoter status in Brain

Gliomas. The third aim has two parts including (i) evaluating the effect of motion corruption and deep learning-based motion correction on the molecular profiling algorithms, and (ii) clinical translation of the molecular profiling algorithms.

The innovation of this study includes, (i) developing deep learning networks (3D Dense-Unet) for image segmentation, (ii) implementing the 3D networks as a classification problem instead of a segmentation problem, (iii) implementing the networks to use minimal pre-processing steps preserving native image information without the need for any region-of-interest or tumor pre-segmentation procedures, (iv) implementing the 3D networks as voxel-wise classifiers, providing a classification for each voxel in the image, and (v) using only T2w MR images making clinical translation much more straightforward.

1.5. Organization of This Thesis

This dissertation has 7 chapters, which consist of four peer reviewed publications (1 publication each from Chapter 2, 3, 4 and 5), and one submitted manuscript (Chapter 6). Chapter 1 is a brief introduction on Brain Gliomas & Magnetic Resonance Imaging, genetic subtyping & molecular profiling, and Deep Learning in medical imaging. Chapter 2 details the design, development, and evaluation of a deep learning algorithm for multi-class brain tumor segmentation using MR Images. Chapters 3, 4 and 5 details the design, development & evaluation of the molecular profiling algorithms for classification of IDH mutation status, classification of 1p/19q co-deletion status and classification of MGMT-promoter status, respectively. Chapter 6 evaluates the effect of motion corruption & deep learning-based motion correction on the molecular profiling algorithms, and clinical translation of all the molecular profiling algorithms. Chapter 7 discusses the limitations and possible future directions in non-invasive molecular profiling using deep learning.

Chapter 2

To develop and evaluate a deep learning algorithm for multi-class brain tumor segmentation using MR Images

This chapter is published at the journal Tomography, vol 6, issue 2, p. 186–193, 2020.

Authorship: *Chandan Ganesh Bangalore Yogananda, Bhavya R. Shah, Maryam Vejdani-Jahromi, Sahil S. Nalawade, Gowtham K. Murugesa[1], Frank F. Yu, Marco C. Pinho, Benjamin C. Wagner, Kyrre E. Emblem, Atle Bjørnerud, Baowei Fei, Ananth J. Madhuranthakam, Joseph A. Maldjian*

2.1. Introduction

Brain tumor segmentation of MR images is a critical step in providing objective measures of predicting aggressiveness and response to therapy in gliomas. It has valuable applications in diagnosis, monitoring, and treatment planning of brain tumors. Manual brain tumor segmentation is a challenging and tedious task for human experts due to the variability of tumor appearance, unclear borders of the tumor and the need to evaluate multiple MR images with different contrasts simultaneously.[5] In addition, manual segmentation is often prone to significant intra and inter-rater variability.[5,6] Hence, machine learning algorithms have been developed for tumor segmentation with high reproducibility and efficiency.[5,6,14] Following the early success of Convolutional Neural Networks (CNNs)[14,15], they are used as one of the major machine learning methods to achieve great success in clinical applications.[12,13]

To address these shortcomings, automated machine learning algorithms have been developed to segment gliomas. Machine learning algorithms have been shown to improve glioma segmentation by decreasing variability and the time required for manual segmentation.[5,6,14] Glioma segmentation is essentially a voxel-level classification task. Algorithms for voxel-level

classification can be broadly divided into classic machine learning techniques such as support vector machines (SVMs), and deep learning methods such as convolutional neural networks (CNNs). CNN-based methods have been shown to outperform classic machine learning methods.[6,16-21]

The Multimodal Brain Tumor Image Segmentation Benchmark (BraTS) challenge was established in 2012 to gauge and facilitate the progress of automated glioma segmentation.[22,23] The BraTS data set represents a valuable, publicly available data set for developing and evaluating tumor segmentation algorithms. The BraTS data set consists of multi-parametric MR scans of low- and high-grade glioma patients that have been manually segmented by expert raters. The BraTS data is provided with three ground truth labels including a) enhancing tumor (ET), b) non-enhancing tumor including necrosis (NEN), and c) edema (ED). Evaluation of the various algorithms in the BraTS challenge is done based on label outputs of whole tumor (WT), tumor core (TC), and enhancing tumor (ET). Whole tumor consists of enhancing components, non-enhancing components including necrosis, and edema (ET + NEN + ED). Tumor core (TC) consists of enhancing components and non-enhancing components including necrosis (ET + NEN). Enhancing tumor consists of just the enhancing component. To evaluate the performance of an algorithm, data can be uploaded to the BraTS validation server which reports back DICE coefficients for TC, WT, and ET.[24]

For the 2017 BraTS challenge, there were 46 cases provided in the BraTS validation dataset. In 2018, the validation set was expanded to 66 cases, including the previous 46. The training dataset remained the same between 2017 and 2018. As such, the BraTS 2018 data set allows developers to compare results to the top performers from 2017 and 2018. The BraTS validation server calculates DICE scores for WT, TC, and ET, but does not provide DICE scores for ED and

NEN. Although ED and NEN DICE scores are not reported by the BraTS server, they can be of value in comparing algorithmic performance. The BraTS challenge also evaluates performance on a held-out test data set, however this data is only available for a brief time period during the challenge.

In this work, we developed a 3D Dense UNet CNN for glioma segmentation that can easily be incorporated into clinical workflow. The algorithm's performance was evaluated using the BraTS validation server for WT, TC, and ET. The algorithm was also tested on an independent clinical dataset from Oslo University Hospital, Oslo, Norway and DICE scores for WT, TC, and ET are reported using expert segmentation as the ground truth. In addition, we also report DICE scores for ED and NEN for both datasets.

2.2. Material and Methods

2.2.1. BraTS Dataset

Multi-parametric MRI data (T2w, T2w-FLAIR, T1, and T1 post-contrast) were obtained from the BraTS2018 dataset. The BraTS2018 dataset consisted of a total of 285 subjects: 210 subjects with high grade glioma (HGG) and 75 subjects with low grade glioma (LGG).[3,7] The dataset included three ground truth labels for a) enhancing tumor, b) non-enhancing tumor including necrosis and c) edema. The BraTS data was already reoriented to the LPS (left posterior-superior) coordinate system, co-registered to T1C, registered to the SR124 template and resampled to 1 mm, skull stripped and N4bias corrected.[23,25] The intensities were normalized to zero mean and unit variance before using the data.

2.2.2. Oslo Dataset

Multi-parametric MRI data (T2w, T2w-FLAIR, T1, and T1c/T1 post-contrast) were obtained from Oslo University Hospital.[26,27] It consisted of 52 preoperative low- and high-grade glioma subjects

(age >18 years) scanned from 2003-2012. Most of the images were acquired with anisotropic voxels, typically used in routine clinical 2D images, characterized by high in-plane resolution (0.7 – 0.9 mm) and low through-plane resolution (slice thickness varying between 5-6 mm).

The original DICOM images were converted to NifTI format for ease of processing. The Oslo dataset was manually segmented by an in-house neuroradiologist for the same three labels used in the BraTS data set (ED, NEN, and ET). Images from the Oslo dataset were pre-processed following the same steps used in the BraTS dataset. The pre-processing pipeline was developed using ANTS[28], and included co-registration to the T1 post-contrast, registering to the SRI24 template,[23,25] resampling to 1 mm^3 isotropic resolution, skull stripping, N4BiasCorrection,[29] and intensity normalization to zero-mean and unit variance.

2.2.3. Network Architecture

The histologic complexity of gliomas poses a challenge to automated tumor segmentation methods. In order to simplify the segmentation problem, a triple network architecture was designed (Figure 1). Each model was trained separately to predict whole tumor (WT-net), tumor core (TC-net), and enhancing tumor (EN-net) as a binary task. The networks used a 3D patch-based approach. Multi-parametric images were passed through the Dense UNet (Figure 2A). The initial convolution generated 64 feature maps that were subsequently used to create dense blocks. Each dense block consisted of five layers (Figure 2B). Each layer included four sequentially connected sublayers: i) batch normalization, ii) rectified linear unit (ReLu), iii) 3D Convolution and iv) 3D spatial dropout. The first layer in dense block 1 had 32 features maps as its input. At each layer, the input was used to generate k feature maps which were then concatenated to the next layer input, which was then applied to create another k feature map. To generate the final dense block output, inputs from each layer were concatenated with the output of the last layer. At the end of each dense

block, the input to the dense block was also concatenated to the output of that dense block. The output of each dense block followed a skip connection to the adjacent decoder part. In addition, each dense block output went through a transition down block until the bottle neck block (Figure 2C). With this connecting pattern, all feature maps were reused such that every layer in the architecture received a direct supervision signal.[30] On the decoder side, a transition up block preceded each dense block until the final convolution layer, which was followed by a sigmoid activation layer.

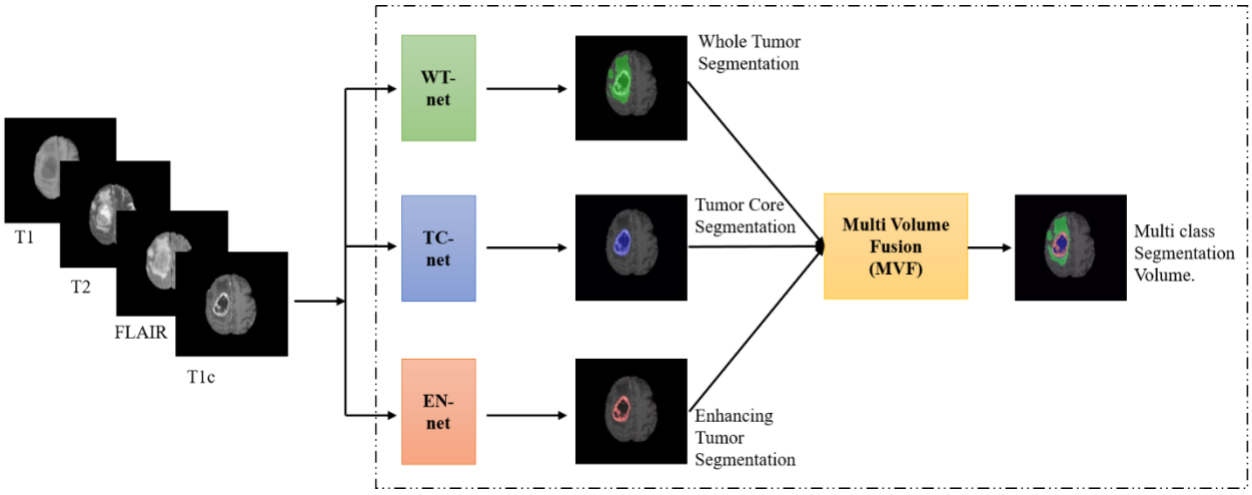

Figure 1: Schematic representation of the developed algorithm.
The input images included T1, T2, T2-FLAIR, and T1 post-contrast (T1C). Whole tumor (WT-net) segments the WT, tumor core (TC-net) segments the TC, and enhancing tumor (EN-net) segments the ET. The output segmented volumes from each of these networks are combined using a triple volume fusion to generate a multiclass segmentation volume.

In order to preserve a high number of convolution layers and fit the complex model into GPU memory, three additional steps were employed. (1) If a layer generated feature maps exceeding the initial number of convolution feature maps, then it was reduced to $1/4^{th}$ of the total number of feature maps generated by that layer. (2) The total number of feature maps generated at the end of every dense block was reduced by a compression factor of 0.75. (3) A bottle neck block (Dense block 4 in Fig. 2A) was used to connect the encoder part of the network to the decoder part of the network. This bottle neck block reduced the feature maps generated by the encoder part of the

network by the same compression factor of 0.75. Due to the large number of high-resolution feature-maps, a patch-based 3D Dense UNet approach was implemented. However, the higher resolution information was passed through the standard skip connections.

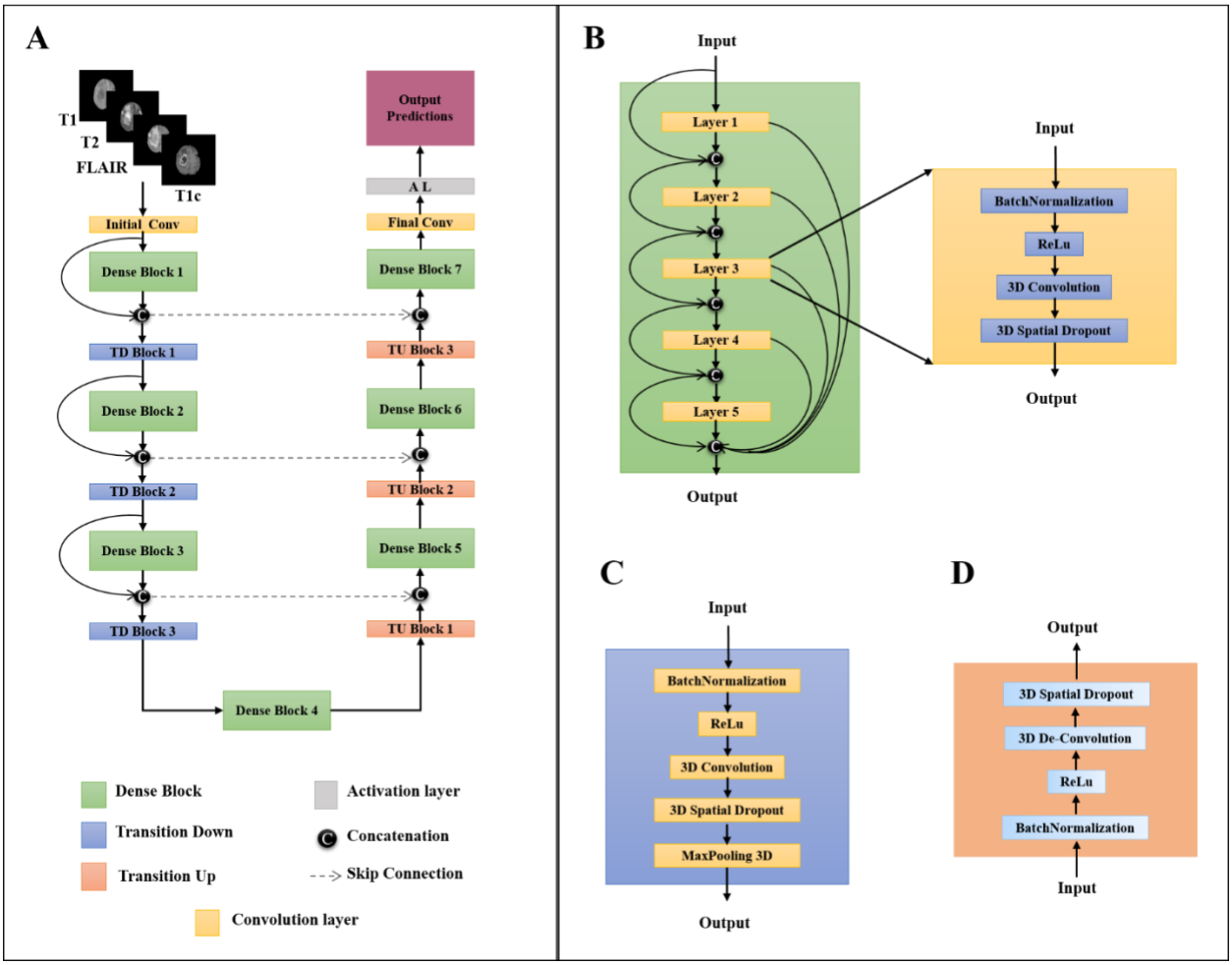

Figure 2: Schematic of the Dense UNet Architecture.

Each network consisted of 7 dense blocks, 3 transition down blocks, and 3 transition up blocks (A). Each dense block was made of 5 layers connected to each other, with every layer having 4 sublayers connected sequentially (B). The transition-down block consisted of 5 layers connected sequentially (C). The transition-up block was a sequential connection of 4 layers (D).

2.2.4. Network Implementation & Cross-validation

2.2.4.1. Cross-validation

To generalize the network's performance and evaluate its reliability, a 3-fold cross validation was performed on the BraTS2018 dataset (210 HGG and 75 LGG subjects). The data was randomly

shuffled and equally split into three groups as training, in-training validation and held-out testing (70 HGG and 25 LGG cases in each group). The in-training validation data set is used by the algorithm to test performance after each round of training, and update model parameters. Each fold of the cross-validation procedure represents a new training phase on a unique combination of the 3 groups. Network performance is only reported on the held-out testing group for each fold.

2.2.4.2. Training

The 3-fold cross-validation procedure uses a relatively small sample of cases from the BraTS2018 data set for training each fold (95 cases). Prior to evaluation of the independent dataset, the networks were retrained on a larger sample of the BraTS2018 data set using ~70% of the cases for training (200 cases including 150 HGG and 50 LGG), ~20% for in-training validation (65 cases including 48 HGG and 17 LGG) and ~10% (20 cases including 12 HGG and 8 LGG) held out for testing. 75% overlapping patches were extracted from multi-parametric brain MR images that had at least one non-zero pixel on the corresponding ground truth patch. Subsequently, 20% of patches were used for in-training validation. Data augmentation steps included horizontal flipping, vertical flipping, random rotation, and translational rotation. Down sampled data (128x128x128) was also provided in the training as an additional data augmentation step. To eliminate the data leakage problem, no patch from the same subject was mixed in training, validation or testing.[31,32] Labels of edema, enhancing tumor and non-enhancing tumor including necrosis were fused to create a whole tumor mask to train WT-net. A tumor core mask was created by fusing the labels of enhancing tumor and non-enhancing tumor including necrosis to train TC-net. Enhancing tumor labels were used separately to train EN-net. The networks were trained using Tensorflow[33], the Keras[34] python package and Pycharm IDEs with adaptive moment estimation (Adam)[35] as the

optimizer. The initial learning rate was set to 10^{-5} with a batch size of 4 and maximal iteration of 100. Training was implemented on Tesla P100, P40 or K80 NVIDIA-GPUs.

2.2.4.3. Testing

The final network was tested on the 20 held out cases. Patches of 32x32x32 were extracted and provided to the network for testing. All of the prediction patches were then reconstructed to obtain a full segmentation volume. After obtaining the three separate segmentation output volumes from the 3 networks, they were fused in two steps. First, a 3D connected components algorithm was applied to the WT-net output to generate a whole tumor mask. Next the outputs from TC-net and EN-net were multiplied by the output from WT-net. This procedure, referred to as multi-volume fusion (MVF), was designed to improve the prediction accuracy by removing false positives. The final network was also tested on 46 cases from BraTS2017 validation dataset, 66 cases from BRATS 2018 validation dataset and 52 cases from the Oslo dataset without any fine-tuning.

2.2.4.4. Statistical Methods

The performance of each network was evaluated using the Dice co-efficient [24], which determines the amount of spatial overlap between the ground truth segmentation (X) and the network segmentation (Y), as:

$$Dice = \frac{2|X_1 \cap Y_1|}{|X_1| + |Y_1|}$$

These output labels are defined as follows:

WT = Edema + Enhancing Tumor + Non-Enhancing Tumor + Necrosis
TC = Enhancing Tumor + Non-Enhancing Tumor + Necrosis
ET = Enhancing Tumor

Dice coefficients were also computed for:

Edema = WT – TC
Non-enhancing Tumor and Necrosis = TC – ET

2.3. Results

2.3.1. Cross-validation

Average dice-scores for the 3-fold cross validation using 75% overlapping patches were 0.90, 0.82 and 0.79 for WT, TC and ET respectively. Average dice-scores for the 3-fold cross validation using 85% overlapping patches were 0.92, 0.84 and 0.80 for WT, TC and ET respectively. Detailed dice-scores are provided in the supplemental material section.

2.3.2. Testing on 20 Held-out cases from BraTS2018

The network achieved dice scores of 0.90, 0.84 and 0.80 with Hausdorff distance of 3.9 mm, 5.9 mm and 3.5 mm for WT, TC and ET, respectively, on the 20 held-out cases (Figure 3). Sensitivities were 0.91, 0.85, and 0.81 for WT, TC, and ET, respectively with 100% specificity for all subcomponents. Dice-scores of 0.85 & 0.80 were obtained for edema, and non-enhancing tumor with necrosis, respectively. The MVF procedure increased accuracies across all assessments by 1-2% (Table 1).

2.3.3. BraTS2017 Validation dataset

The network achieved dice scores of 0.90, 0.80 and 0.78 with Hausdorff distance of 6.5 mm, 8.7 mm and 5.5 mm for WT, TC and ET respectively, on the BraTS2017 validation dataset (Table 2). Sensitivities were 0.90, 0.80, and 0.78 for WT, TC, and ET, respectively with 100% specificity for all subcomponents.

2.3.4. BraTS2018 Validation dataset

The network achieved dice scores of 0.90, 0.82 and 0.80 with Hausdorff distance of 6.0 mm, 7.5 mm and 4.4 mm for WT, TC and ET respectively, on the BraTS2018 validation dataset (Table 2). Sensitivities were 0.91, 0.81, and 0.81 for WT, TC, and ET, respectively with 100% specificity for all subcomponents.

Table 1: Cross-Validation results & Mean dice-scores (across subjects) on 20 subjects held out dataset

Cross-Validation Results				
	Fold 1	**Fold 2**	**Fold 3**	**AVERAGE**
Whole tumor	0.93	0.94	0.90	0.92
Tumor Core	0.89	0.84	0.80	0.84
Enhancing tumor	0.84	0.80	0.77	0.80
Non-enhancing and Necrosis	0.80	0.81	0.80	0.80
Edema	0.85	0.86	0.85	0.85
Results on 20 subjects held out dataset				
	Before TVF		**After TVF**	
Whole tumor	0.89		0.90	
Tumor Core	0.82		0.84	
Enhancing tumor	0.78		0.80	
Non-enhancing and Necrosis	0.79		0.80	
Edema	0.83		0.85	

Table 2: Comparison with best performers of BraTS 2017 and BraTS 2018 Challenge

Comparison to Best performers on BraTS 2017 Validation data			
Network type	**Whole Tumor**	**Tumor Core**	**Enhancing Tumor**
EMMA (val)	0.901	0.797	0.738
Wang et.al (val) (Cascaded network)	0.905	0.837	0.785
Dense UNet (ours) (val)	0.907	0.804	0.787
Comparison to Best performers on BraTS 2018 Validation data			
Network type	**Whole Tumor**	**Tumor Core**	**Enhancing Tumor**
NVIDIA (val)	0.910	0.866	0.823
No New-Net (val)	0.908	0.854	0.810
McKinley et. al (val)	0.900	0.853	0.794
Dense Unet (ours) (val)	0.900	0.820	0.800

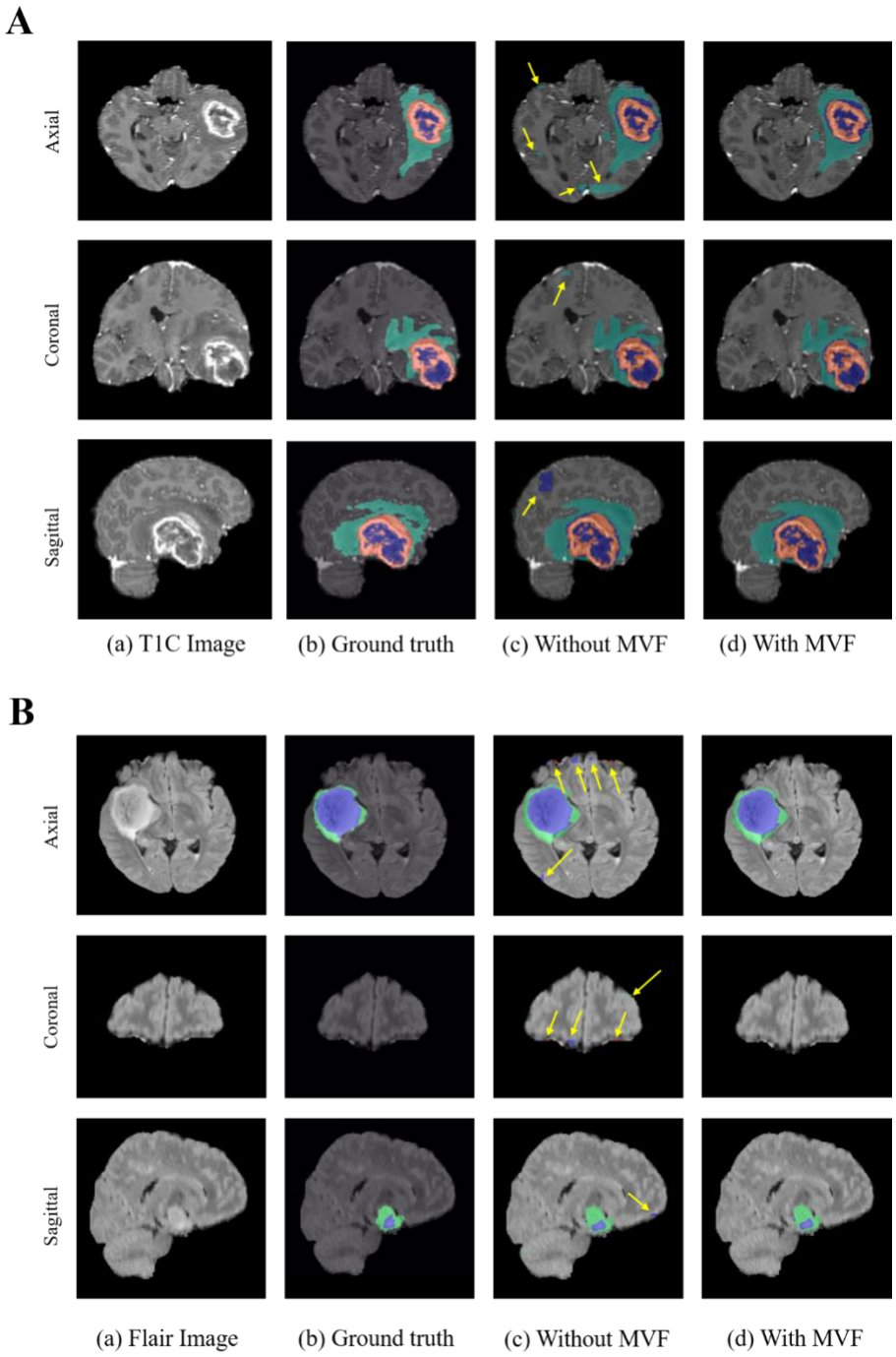

Figure 3: Example Segmentation results.

High-grade glioma (HGG) and (A) low-grade glioma (LGG) (B). (a) A 2D slice of a postcontrast image, (b) ground truth image, (c) network output without multivolume fusion (MVF), and (d) network output with MVF. The arrows in (c) represent false positives that are successfully eliminated after MVF (d). Color Codes: red = ET, blue = TC (ET + NEN), green = ED; whole tumor = green + blue + red.

2.3.5. Clinical validation dataset

The network achieved dice scores of 0.85, 0.80 and 0.77 with Hausdorff distance of 5.74 mm, 5.94 mm and 4.06 mm for WT, TC and ET respectively, on the Oslo clinical dataset (Table 3). Sensitivities were 0.86, 0.79, and 0.77 for WT, TC, and ET, respectively with 100% specificity for all subcomponents.

Table 3: Mean dice-scores (across subjects) on clinical dataset

Tumor type or sub-component	Dice Scores
Whole tumor	0.85
Tumor Core	0.80
Enhancing tumor	0.77
Edema	0.80
Necrosis	0.74

2.4. Discussion

Gliomas are the most common primary brain tumor. Currently, the vast majority of clinical and research efforts to evaluate response to therapy rely on gross geometric measurements. Manual tumor segmentation is a tedious, time intensive task that requires a human expert. Quantitative evaluations of manual tumor segmentations have revealed considerable disagreement reflected in Dice scores in the range 74%–85%.[22] To address these shortcomings, automated machine learning algorithms have been developed to segment gliomas.[5,6,14]

MRI-based glioma segmentation algorithms represent a method to reduce subjectivity and provide *quantitative* analysis. Accurate, reproducible, and efficient tumor segmentation has the potential to improve glioma management by being able to differentiate active tumor from necrotic tissue and edema. As a result, a significant effort has been made to facilitate the progress of automated glioma segmentation.

Our algorithm performed similarly to previously published high-performing algorithms in segmenting ET and WT (Table 2) on the BraTS2017 data set and was one of the top 3 performers in segmenting TC. The algorithm was also one of the top 3 performers in segmenting WT and ET on the BraTS 2018 dataset (Table 2).

To generalize the network's performance and evaluate its reliability, we also performed 3-fold cross validation, which demonstrated mean accuracies of 0.92, 0.84 and 0.80 for WT, TC and ET respectively. The results of this cross-validation are not comparable to the accuracies reported by the BraTS challenge, as our cross validation used one-third of the data for training, whereas most developers use all 285 cases to train their algorithm and cross-validation is not reported.

The entire pipeline including all the pre-processing steps took approximately 5 minutes per subject for testing. The Dice scores were slightly reduced when validated on the clinical data set. This decrease in performance was expected due to practical considerations when utilizing clinical scans. For example, differences in field strength (1.5T vs 3T), clinical imaging sequence parameters and variability in post processing may account for the decreased performance. Despite these limitations our deep learning network was able to segment tumors and sub-components with excellent results without any fine-tuning and shows promise for incorporation into clinical workflow.

Variable performance among CNNs can also be due to differences in the underlying network architecture. The triple network architecture described here has several advantages when compared to multi-label CNNs. Training three separate networks for individual binary segmentation tasks is less complex and less computationally challenging than training one network to perform multi-class segmentations. Additionally, since all three networks are trained separately as binary segmentation problems, misclassification is also highly reduced, thereby reducing over-fitting.

The dense architecture also reduces false positives, because all feature maps are reused such that every layer in the architecture receives a direct supervision signal [30]. The *vanishing gradient problem* is a challenge when using gradient-based learning methods to train neural networks. If the gradient is too small, the neural network weight will not change in value. As more layers with activation functions are added to the network, the gradient can approach zero, making it difficult to train the network. Our algorithm diminished the vanishing gradient problem by using dense networks, which use feature propagation through the dense connection to the subsequent layers. In order to overcome computational considerations when using a full size image, our algorithm used a patch based 3D Dense-Unet [30]. An additional unique feature of our network was the procedure for TVF which effectively eliminated false positives (Figure 3). TVF improved network performance across all segmentations. Compared to previously published work on tumor segmentation, our networks employed minimal pre- and post-processing steps.

2.5. Limitations

A general limitation of deep-learning methods is the need for a large number of subjects to train the network. The BraTS server validation dataset does not provide dice coefficients for "non-enhancing tissue + necrosis," and edema labels. Even though our network was able to identify these components, the performance for these labels could not be evaluated using the BraTS validation server data set. Memory and computation power limitations remain a consideration in deep learning methods. For instance, when overlapping patches were increased from 75% to 85% for our algorithm, the 3-fold cross validation results increased to 0.92, 0.84 and 0.80 for WT, TC and ET respectively. However, due to memory limitations, the 85% overlapping patches could not be implemented for training using all the 265 subjects. This suggests that the network has room for improvement with additional memory and computational power advancements.

2.6. Conclusion

A 3D Dense UNet was developed for MRI-based segmentation of gliomas. The algorithm can easily be incorporated into a clinical workflow. Our algorithm outperformed the best performers for segmenting whole tumor and enhancing tumor.

Chapter 3

A Novel Fully Automated MRI-based Deep Learning Method for Classification of IDH Mutation Status in Brain Gliomas

This work is published at the journal Neuro Oncology, vol 22, issue 3, p. 402–411, Mar 5th,2020.

Authorship: *Chandan Ganesh Bangalore Yogananda, Bhavya R. Shah, Maryam Vejdani-Jahromi, Sahil S. Nalawade, Gowtham K. Murugesan, Frank F. Yu, Marco C. Pinho, Benjamin C. Wagner, Bruce Mickey, Toral R. Patel, Baowei Fei, Ananth J. Madhuranthakam, Joseph A. Maldjian*

3.1. Importance of the study

One of the most important recent discoveries in brain glioma biology has been the identification of the isocitrate dehydrogenase (IDH) mutation status as a marker for therapy and prognosis. The mutated form of the gene confers a better prognosis and treatment response than gliomas with the non-mutated or wild-type form. Currently, the only reliable way to determine IDH mutation status is to obtain glioma tissue either via an invasive brain biopsy or following open surgical resection. The ability to non-invasively determine IDH mutation status has significant implications in determining therapy and predicting prognosis. We developed a highly accurate, deep learning network that utilizes only T2-weighted MR images and outperforms previously published methods. The high IDH classification accuracy of our T2w image only network (T2-net) marks an important milestone towards clinical translation. Imminent clinical translation is feasible because T2-weighted MR imaging is widely available and routinely performed in the assessment of gliomas.

3.2. Introduction

Isocitrate dehydrogenase (IDH) mutation status has emerged as one of the most important markers for glioma diagnosis and therapy. Gliomas with this mutant enzyme have a better prognosis than tumors of the same grade with wild-type IDH. This observation led the World Health Organization (WHO) to revise their classification of gliomas in 2016.[9] IDH mutated tumors also have different management and therapeutic approaches than tumors with wild-type mutation status. At the present time, the only way to definitively identify an IDH mutated glioma is to perform immunohistochemistry or gene sequencing on a tissue specimen, acquired through biopsy or surgical resection. Because the differences between IDH mutated and IDH wild-type gliomas may have critical treatment implications, there is great interest in attempting to distinguish between these two tumor types prior to surgery. This becomes even more important for brain tumors that are inaccessible for biopsy or resection due to a high risk of severe post-operative complications and impairment.

MR spectroscopy can potentially be used to determine IDH mutation status. The mutant IDH enzyme catalyzes the production of the oncometabolite 2-hydroxyglutarate (2-HG).[36] MR spectroscopic methods have been developed for identification of 2-HG[37-40] noninvasively in brain tumors. While these methods appear to work well in a research setting, in the busy clinical environment, the spectroscopic imaging data are frequently uninterpretable due to artifact, patient motion, poor shimming, small voxel sizes, non-ideal tumor location, or presence of hemorrhage or calcification affecting measurements. Even in the setting of good quality spectra, reliable clinical implementation using 2-HG spectroscopy is further compounded by the recently described high false positive rate of over 20% using this technique in the best hands.[41]

Early determination of IDH mutation status directly impacts treatment decisions. Tumors that appear to be low-grade gliomas, but are IDH wild-type, are typically treated with early intervention rather than observation. Specific chemotherapeutic interventions are more effective in IDH-mutated gliomas (e.g., temozolomide).[42-46] Additionally, surgical resection of non-enhancing tumor volume (beyond gross total resection of enhancing tumor components) in Grade III-IV IDH-mutated tumors has been demonstrated to have a survival benefit.[47] However, the determination of IDH mutation status continues to be performed using direct tissue sampling. Obtaining tumor-rich tissue samples for determining IDH status can be a challenge. A TCGA report suggests that only 35% of biopsy samples contained sufficient tumor content for appropriate molecular characterization.[48] The development of a robust non-invasive approach would be beneficial in the care of these patients.

Advances in deep-learning methods are outperforming traditional machine-learning methods in predicting the genetic and molecular biology of tumors based on MRI. For example, Zhang et al. used a radiomics approach integrating a support vector machine (SVM)-based model and multimodal MRI features with an accuracy of 80% for IDH detection.[49] In another study using multimodal MRI, clinical features, and a random forest machine learning algorithm, Zhang et al was able to obtain 86% accuracy in predicting IDH mutation status.[50] In that study, the highest predictive features included age, parametric intensity, texture and shape features. Recent studies by Chang et al., have used deep learning techniques to noninvasively determine IDH mutation status based on MRI, with accuracies of 94% using the TCIA database.[51] Unfortunately, none of these methods are clinically viable, requiring either manual pre-segmentation of the tumor, extensive pre-processing, or multi-contrast acquisitions that are frequently affected by patient motion due to the long scan times. Additionally, these existing methodologies use a 2D (slice-

wise) classification approach. A known limitation in designing and developing a slice-wise classification model is the *data-leakage problem.*[31,32] 2D slice-wise models working with cross-sectional imaging data are particularly prone to data-leakage because they perform slice randomization across all subjects to generate the training, validation, and testing slices. As a result, adjacent slices from the same subject may be found in the training, validation, or testing data subsets. Because adjacent slices often share considerable information, this methodology may artificially boost accuracies by introducing bias in the testing phase. Previously reported studies do not appear to adhere to this caveat, potentially resulting in artificially boosted accuracies.

The purpose of this study is to develop a highly accurate fully automated deep learning IDH-classification 3D network using T2-weighted images only and compare its performance to a multi-contrast 3D network. The use of T2 images only provides strong clinical translation capability. T2 images are routinely acquired as part of any MRI brain tumor evaluation. These images are robust to motion and can be obtained within 2 minutes. On modern MRI scanners available in most clinical settings, high quality T2w images can be obtained even in the presence of active patient motion using commonly available motion resistant acquisition techniques.[52]

3.3. Material and Methods

3.3.1. Data and Pre-processing

Multi-parametric brain MRI data of glioma patients were obtained from the Cancer Imaging Archive (TCIA)[53] database. Genomic information was provided from TCGA (the cancer genome atlas) database.[54] Only pre-operative studies were used. Studies were screened for the availability of IDH status and T2w, T2w-FLAIR, and contrast enhanced T1-weighted (T1c) image series. The final dataset included 214 subjects (94 IDH-mutated, 120 IDH wild-type). TCGA subject IDs, IDH

mutation status, 1p/19q co-deletion status, histology, and clinical variables including age, gender, survival months, and Karnofsky performance scores are listed in Table 1 of the supplementary data. The average age of the cohort was 52 ± 15 years with 48% female subjects. Histologically, 49% of tumors were glioblastomas, 22% were oligodendrogliomas, 15% were astrocytomas, and 14% were oligoastrocytomas, with 48% of tumors Grade IV, 27% grade III, and 24% grade II. In this cohort 56% of tumors were IDH wild-type, 42% were IDH-1 mutant, and 1.9% were IDH-2 mutant. Since the vast majority of IDH mutations were IDH-1, both IDH-1 and IDH-2 mutants were considered as one group. 86% of the IDH mutated cases did not have 1p/19q codeletions, while 14% did. IDH mutation status provided in the TCGA database was determined using Sanger sequenced DNA methods and exome sequencing of whole genome amplified DNA. The Sanger method is considered the gold-standard in genetic analysis.[55,56]

Tumor masks for 87 subjects were available through previous expert segmentation.[3,7] Tumor masks for the remaining 127 subjects were manually drawn and validated by in-house neuro-radiologists. The tumor masks were used as the ground truth for the tumor segmentation in the training step. Ground truth whole tumor masks for IDH mutated type were labelled with 1s and the ground truth tumor masks for IDH wild-type were labelled with 2s (Figure 4). Data preprocessing was minimal, including (a) N4BiasCorrection to remove RF inhomogeneity, (b) co-registration of the multi-contrast data to the T1c (for TS-net only), and (c) intensity normalization to zero-mean and unit variance.[29] The pre-processing was developed using the Advanced Normalization Tools (ANTS) software routines[28] and took less than 5 minutes per dataset.

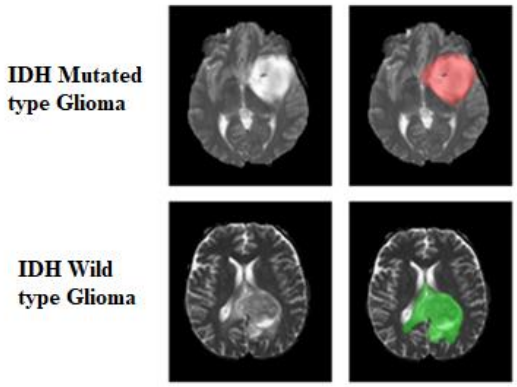

Figure 4: Ground truth whole tumor masks.
Red voxels represent IDH mutated (value of 1) and green voxels represent IDH wild-type (value of 2). The ground truth labels have the same mutation status for all voxels in each tumor.

3.3.2. Network Details

Two separate networks were developed. These included a T2w image only network (T2-net) trained only on the T2w images (Figure 5A), and a 3-sequence network (TS-net) trained on multi-contrast MR data including T2w images, T2w-FLAIR, and T1c. A 3D 32×32×32 patch-based training and testing approach was implemented for both networks. Dense-UNets were designed and trained for a voxel-wise dual-class segmentation of the whole tumor with Classes 1 and 2 representing IDH-mutated and IDH-wild-type, respectively. The schematics for the network architecture is shown in Figure 5B. Each network consisted of seven dense blocks: three transition down blocks, three transition up blocks, an initial convolution layer, and a final convolution layer followed by an activation layer at the end. Each dense block was made up of five layers. Each layer was connected to every other layer in that particular dense block. This dense connection was implemented by concatenating the feature maps from one layer with feature maps from every other layer of that dense block. The input to a dense block was also concatenated with the output of that dense block. Every dense block on the encoder part of the network was followed by a transition down block, while every dense block on the decoder part of the network was preceded by a

transition up block. The bottleneck block was used to keep the convolution layers to a smaller number in order to avoid having large convolution layers. With these connecting patterns, all feature maps were reused such that every layer in the architecture received a direct supervision signal.[30] A detailed description of the network is depicted in Figure 6.

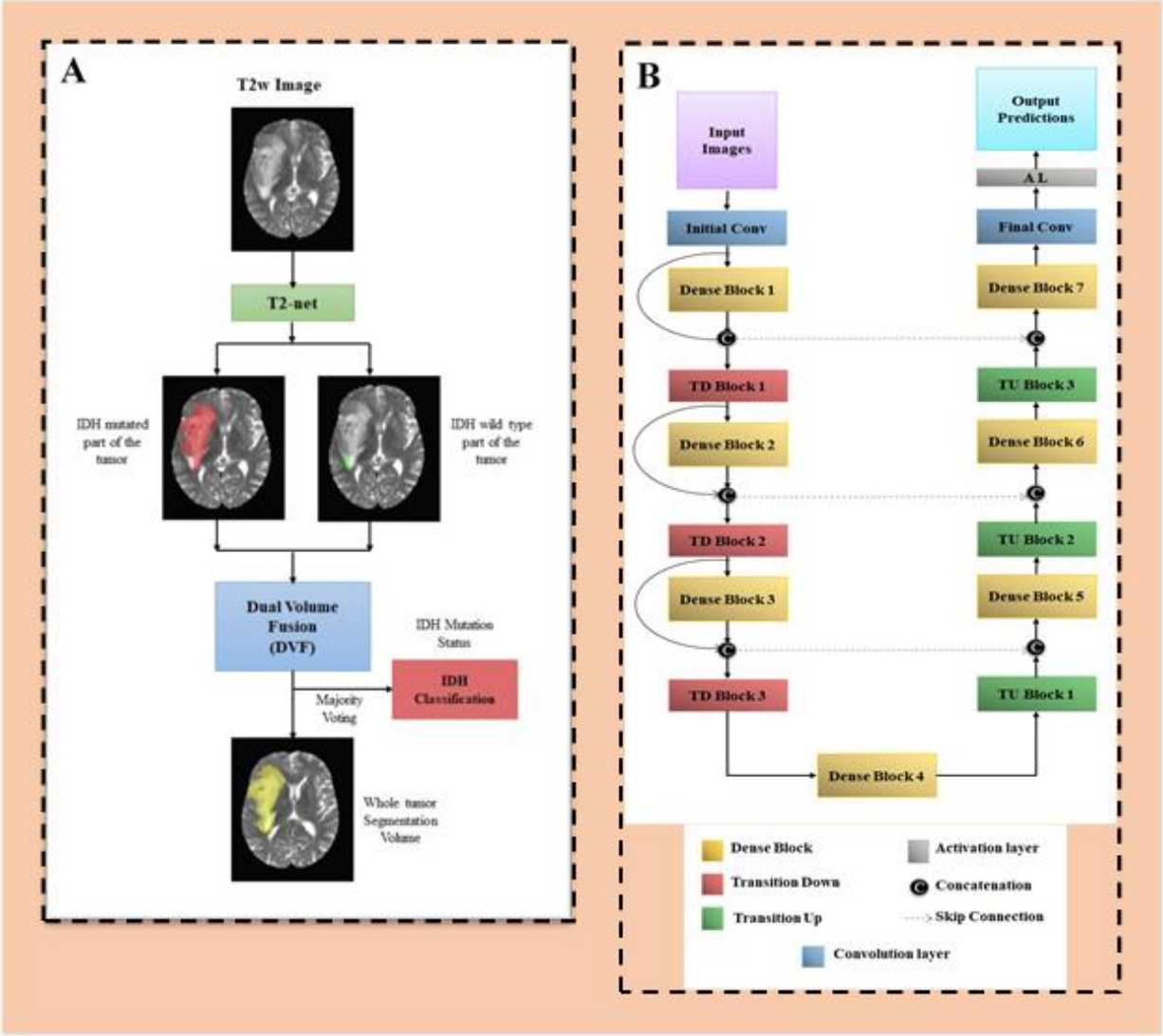

Figure 5: (A) T2-net overview. *Voxelwise classification of IDH mutation status is performed to create 2 volumes (IDH mutated and IDH wild-type). Volumes are combined using dual volume fusion to eliminate false positives and generate a tumor segmentation volume. Majority voting across voxels is used to determine the overall IDH mutation status.* ***(B) Network architecture for T2-net and TS-net.*** *3D Dense-UNets were employed with 7 dense blocks, 3 transition down blocks, and 3 transition up blocks.*

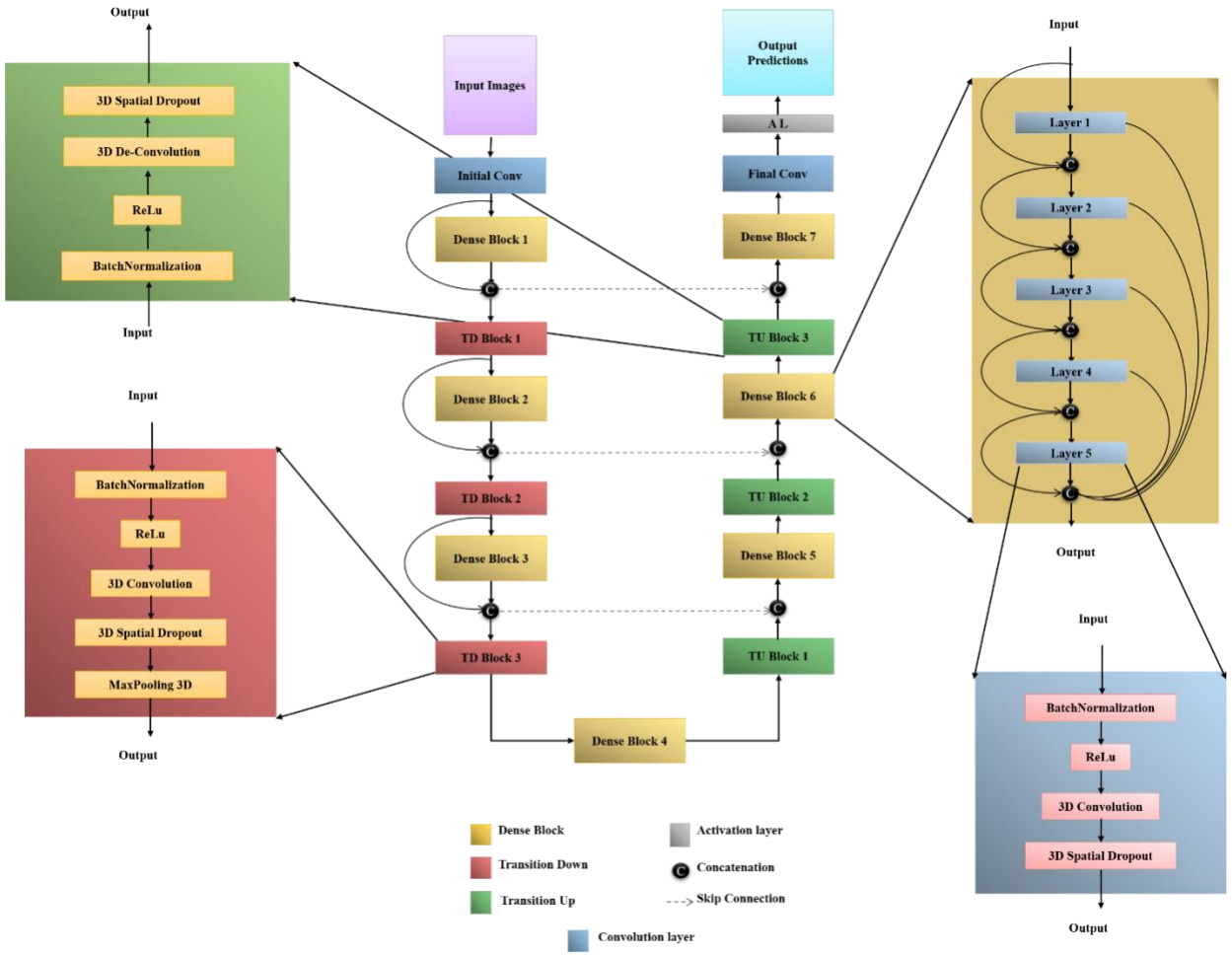

Figure 6: Detailed network architecture for T2-net and TS-net.

3D-Dense-UNets were employed with 7 dense blocks, 3 transition down blocks, and 3 transition up blocks. Each dense block was made of 5 layers connected to each other with every layer having 4 sublayers connected sequentially. The transition down block consisted of 5 layers connected sequentially while the transition up block was a sequential connection of 4layers.

3.3.3. Network Implementation and Cross-validation

To generalize the reliability of the networks, a 3-fold cross-validation was performed on the 214 subjects by randomly shuffling the dataset and distributing it into 3 groups (approximately 70 subjects for each group). During each fold of the cross-validation procedure, the 3 groups are alternated between training, in-training validation, and held-out testing. Group 1 had 72 subjects (32 IDH mutated, 40 IDH wild-type), Group 2 had 71 subjects subjects (31 IDH mutated, 40 IDH wild-type), and Group 3 had 71 subjects (31 IDH mutated, 40 IDH wild-type). The in-training

validation set helps improve network performance during training. Note that each fold of the cross-validation procedure represents a new training phase on a unique combination of the 3 groups. Network performance is only reported however, on the held-out testing group for each fold (which is never seen by the algorithm during training for that fold). Table 1 of the supplementary data lists the group membership for each fold of the cross-validation. The in-training validation data set is used by the algorithm to test performance after each round of training, and update model parameters. It is not a true held-out data set because the algorithm adjusts its performance based on the results in each round from the in-training validation data set. Once the algorithm has completed all rounds of training, it is evaluated on the true held-out data set to determine performance.

Seventy-five percent overlapping patches were extracted from the training and in-training validation subjects. To avoid the data leakage problem, no patch from the same subject was mixed with the training, in-training validation or testing datasets.[31,32] The data augmentation steps included horizontal flipping, vertical flipping, random and translational rotation. Data augmentation provided a total of approximately 150,000 patches for training and 150,000 patches for in-training validation. Networks were implemented using Keras[34] and Tensorflow[33] with an Adaptive Moment Estimation optimizer (Adam).[35] The initial learning rate was set to 10^{-5} with a batch size of 4 and maximal iterations of 100. Initial parameters were chosen based on previous work with Dense-UNets using brain imaging data and semantic segmentation.[30,57]

Each network yields two segmentation volumes. Volume 1 provides the voxel-wise prediction of IDH mutated tumor and Volume 2 identifies the predicted IDH wild-type tumor voxels. A straightforward dual-volume fusion (DVF) approach was developed to combine the 2 segmentation volumes. Both the volumes were combined, and the largest connected component

was obtained using a 3D connected component algorithm in MATLAB(R). The combined volumes provided a single tumor segmentation map. Majority voting over the voxel-wise classes of IDH-mutated or IDH-wild-type provided a single IDH classification for each subject. Networks were implemented on Tesla P100, P40 and K80 NVIDIA-GPUs. The IDH classification process developed is fully automated, and a tumor segmentation map is a natural output of the voxel-wise classification approach.

3.3.4. Statistical Analysis

Statistical analysis was performed in MATLAB(R) and R for T2-net and TS-net separately. The accuracy of the two networks was evaluated with majority voting (*i.e.* voxel-wise cutoff of 50%). This threshold was then used to calculate the accuracy, sensitivity, specificity, positive predictive value (PPV), negative predictive value (NPV) of the model for each fold of the cross-validation procedure. To evaluate the performance of the networks for tumor segmentation, the Dice-score was used. The Dice-score determines the amount of spatial overlap between the ground truth and the network segmentation. A Receiver Operating Characteristic (ROC) curve was calculated for each fold. A detailed description of the ROC methodology is provided in the supplementary data.

3.3.4.1. ROC methodology

The network output classifies voxels in the tumor as IDH mutated or IDH wild-type. The percent of IDH-mutated voxels was computed for the network output for each subject in the test set by dividing the predicted IDH mutated voxels by the total number of predicted voxels in each tumor. The percent mutated voxels can be viewed as a network output prediction likelihood of the tumor being IDH-mutated. Note that, majority voting (the 50% threshold) was used to determine IDH prediction. For the ROC analysis, the percent of IDH mutated voxels was sorted and used as separate thresholds (cut-points) to determine IDH mutation status for the subjects across the test

set for each new cut-point. The resulting predicted IDH class membership was compared to the ground truth values to determine sensitivity (true positive rate) and 1- specificity (false positive rate) at each threshold. The resulting values were plotted using R program & Matlab routines to obtain an ROC curve and determine the area under the curve (AUC). This procedure was repeated for each of the 3 test folds from the cross-validation procedure for T2-net & TS-net separately. Smoothed curves were used to facilitate display for the figure.

3.4. Results

3.4.1. T2-net

T2-net achieved a mean cross-validation testing accuracy of 97.14% across the 3 folds (97.18%, 97.14%, and 97.10%, standard dev=0.04). Mean cross-validation sensitivity, specificity, PPV, NPV and AUC for T2-net was 0.97 ±0.03, 0.98 ±0.01, 0.98 ±0.01, 0.97 ±0.01 and 0.98 ±0.01, respectively. The mean cross-validation Dice-score for tumor segmentation was 0.85 ± 0.009. T2-net misclassified 2 cases for each fold (6 total out of 214 subjects). Three subjects were misclassified as IDH mutated, and 3 as IDH wild-type.

3.4.2. Multi-contrast TS-net

The multi-contrast TS-net achieved a mean cross-validation testing accuracy of 97.12% across the 3 folds (97.22%, 97.10%, and 97.05%, standard dev=0.09). Mean cross-validation sensitivity, specificity, PPV, NPV and AUC for TS-net was 0.98 ±0.02, 0.97 ±0.001, 0.97 ±0.002, 0.97 ±0.001 and 0.99 ±0.01, respectively. The mean cross-validation Dice-score for tumor segmentation was 0.89 ± 0.006. TS-net also misclassified 2 cases for each fold (6 total out of 214 subjects). Three subjects were misclassified as IDH mutated, and 3 as IDH wild-type. The misclassified subjects were not the same as those misclassified by T2-net. Classification accuracies and Dice scores for T2-net and TS-net are presented in Table 4.

Table 4: T2-net and TS-net cross-validation results

Fold Description	T2-net		TS-net	
Fold Number	**% Accuracy**	**Dice score**	**% Accuracy**	**Dice Score**
Fold 1	97.18	0.843	97.22	0.88
Fold 2	97.14	0.86	97.10	0.883
Fold 3	97.10	0.857	97.05	0.892
Average	**97.14 ± 0.04**	**0.853 ± 0.009**	**97.12 ± 0.09**	**0.885 ± 0.006**

3.4.3. ROC analysis

The ROC curves for each cross-validation fold for T2-net and TS-net are provided in Figure 7. T2-net and TS-net demonstrated near identical performance curves with extremely high sensitivities and specificities.

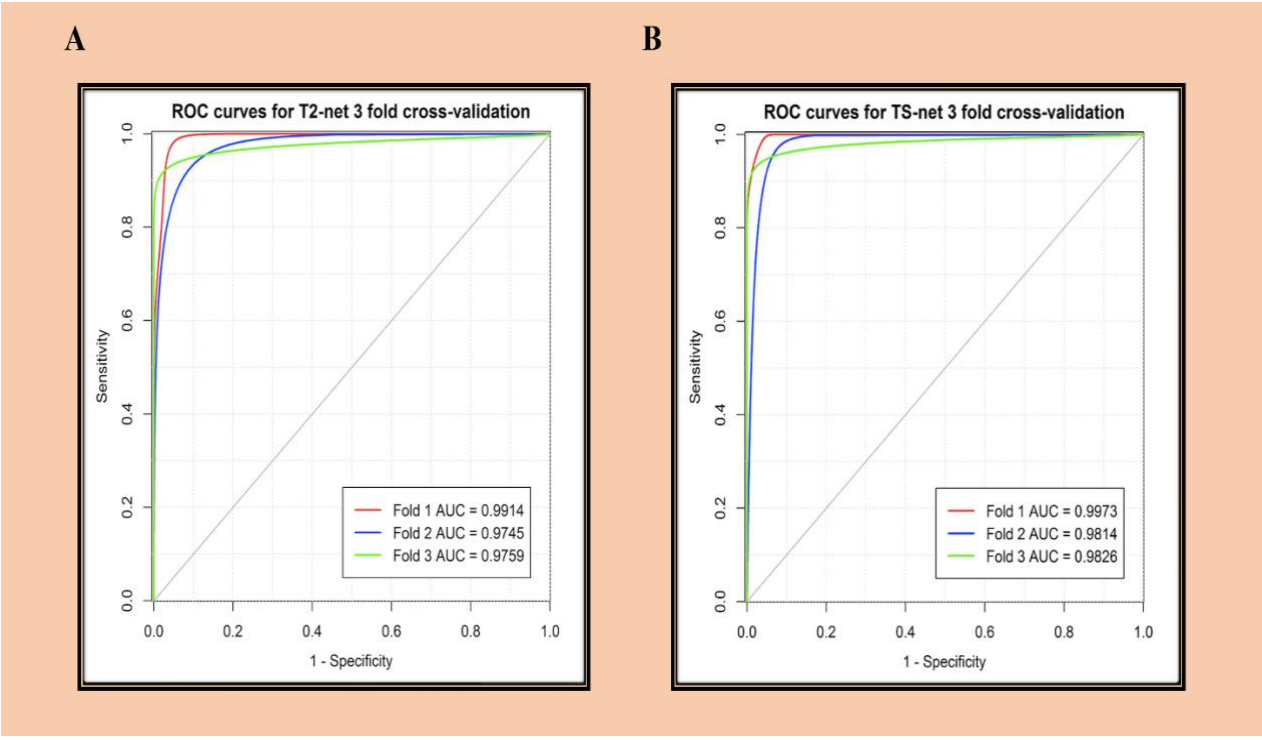

Figure 7: (A) ROC analysis for T2-net. (B) ROC analysis for TS-net.
Separate curves are plotted for each cross-validation fold along with corresponding AUC value.

3.4.4. Voxel-wise classification

Since these networks are voxel-wise classifiers, they perform a simultaneous tumor segmentation. Figures 8A and 8B show examples of the voxel-wise classification for an IDH wild-type, and IDH mutated case using T2-net. The DVF procedure was effective in removing false positives to increase accuracy. The DVF procedure removed approximately 16% and 17% of the classified voxels for T2-net and TS-net respectively. This procedure improved the dice-scores by approximately 3% for each network. We also computed the voxel-wise accuracy for each network. The performance on the IDH wild-type subjects was very similar between the two networks, while for IDH mutated, the voxel-wise accuracies were better for TS-net. For T2-net, the mean voxel-wise accuracies were 84.9% ±0.05 for IDH wild-type and 76.4% ±0.03 for IDH mutated. For TS-net, the mean voxel-wise accuracies were 85.7% ±0.04 and 84.7% ±0.01 for IDH wild-type and IDH mutated, respectively.

3.4.5. Training and segmentation times

Each network took approximately 2 weeks to train. The trained networks took approximately 3 minutes to segment the whole tumor, implement DVF & predict the IDH mutation status for each subject.

3.5. Discussion

We developed two deep-learning MRI networks for IDH-classification of gliomas based on imaging features alone. Both our T2-network and the multi-contrast network outperformed IDH classification algorithms previously reported in the literature.[49,51,58,59] When comparing the T2-network with the multi-contrast network, our results suggest that similar performance can be achieved by using T2-weighted images only. The ability to use only T2-weighted images makes clinical translation much more straightforward and less prone to failures from image acquisition

artifacts. The preprocessing used to prepare the data is also minimal. The time required for T2-net to segment the whole tumor, implement DVF, and predict the IDH mutation status for one subject is approximately 3 minutes on a K80 or P40 NVIDA-GPU.

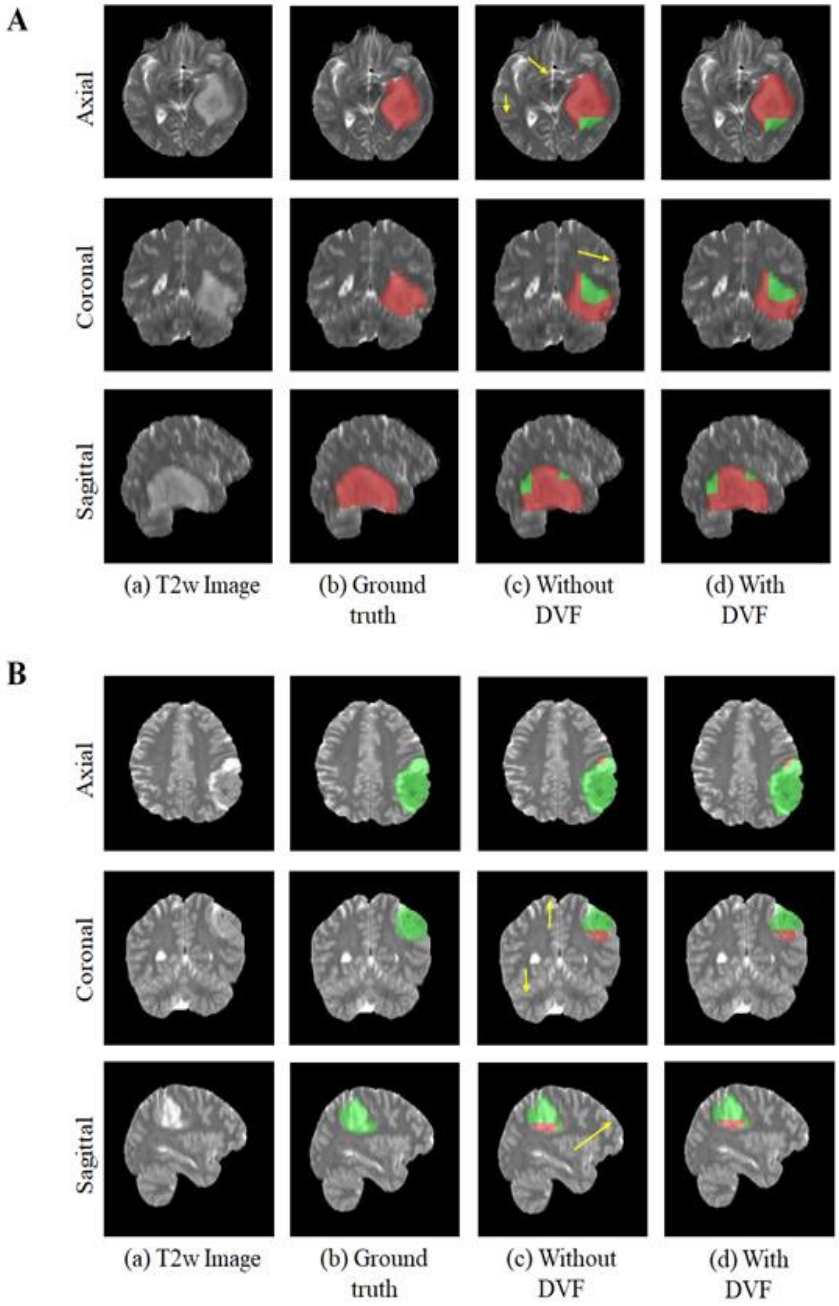

Figure 8: (A) Example voxelwise segmentation for an IDH mutated tumor. *Native T2 image (a). Ground truth segmentation (b). Network output without DVF (c) and after DVF (d). Yellow arrows in (C) indicate false positives. Red voxels correspond to IDH mutated class and green voxels correspond to IDH wild-type.* ***(B) Example voxelwise segmentation for an IDH wild-type tumor.*** *The sharp borders visible between IDH mutated and wild-type result from the patchwise classification approach.*

There are several factors that may explain the higher performance achieved by our networks when compared to previously published results. First and foremost is the use of 3D networks, compared to previously reported 2D networks. Additionally, the 3D network architecture is advantageous as the dense connections carry information from all the previous layers to the following layers.[30] These types of networks are easier to train and can reduce over-fitting.[14] The Dual Volume Fusion (DVF) post-processing step also helps in effectively eliminating false positives while increasing the segmentation accuracy by excluding extraneous voxels that are not connected to the tumor. DVF improved the dice-scores by approximately 3% for each network. The 3D networks interpolate between slices to maintain inter-slice information more accurately. The networks use minimal preprocessing without any requirement for extraction of pre-engineered features from the images or histopathological data.[58]

The 3D networks used here are voxel-wise classifiers, providing a classification for each voxel in the image. This provides a simultaneous single-label tumor segmentation (e.g. the sum of voxels classified as IDH mutated and non-mutated provide the tumor label). The cross validation single label whole tumor segmentation performance for these networks provided excellent Dice-scores of 0.85 and 0.89 for T2-net and the multi-contrast TS-net, respectively. These tumor segmentation Dice-scores are similar to the top performers from BraTS2017 tumor segmentation challenge.[14]

Both T2-net and TS-net achieved similar overall subject classification accuracies. This suggests that the information from the T2w images alone can provide a high classification confidence. For the IDH wild-type tumors, both networks incorrectly classified 2 subjects per fold. These 6 subjects were not the same between the networks. In reviewing these cases, there were no discriminating imaging features. The majority of these cases had heterogeneous enhancement, with mixed T2 and FLAIR signal, and surrounding edema. Although T2-net and TS-net

demonstrated similar performance on subject-wise IDH classification, the voxel-wise performance was different between the networks. TS-net demonstrated similar accuracies in predicting IDH wild-type voxels (85.7% vs 84.9%), and slightly higher accuracies in predicting IDH mutated voxels (84.7% vs 76.4%).

Since these networks are voxel-wise classifiers, there are portions within each tumor that are classified as IDH mutated, and other areas as IDH-wild-type. Heterogeneous genetic expression can occur in gliomas over time and result in varied tumor biology.[51,60] In the clinical setting, immunohistochemistry (IHC) evaluations are primarily used. IHC uses monoclonal antibodies to detect the most frequent IDH mutations (e.g. IDH1-R132H). Different cutoff values have been proposed to determine the IDH status of a tissue sample using IHC methods. While some advocate staining of more than 10% of tumor cells to confer IDH positivity, others suggest that one "strongly" staining tumor cell is sufficient. [61] Heterogeneity of staining with IHC has been reported where up to 46% of subjects showed partial uptake.[62] In 2011 Perusser et al. reported that IDH1-R132H expression may occur in only a fraction of tumor cells.[63] Heterogeneity of the sample can also affect the sensitivity of genetic testing.[64] IDH heterogeneity and reported false negativity in some gliomas have been explained by monoallelic gene expression, wherein only one allele of a gene is expressed even though both alleles are present. According to Horbinski, sequencing may not always be adequate to identify tumors that are functionally IDH1/2 mutated.[63,65] Although heterogeneity of IDH status has been reported in histochemical and genomic evaluations of gliomas, we do not make the claim that the deep learning networks are detecting heterogeneous IDH mutation status in these tumors. Rather, the morphologic expression of the IDH mutation status is likely heterogeneous and reflected in the mixed classification outputs of IDH-mutated and

IDH-wild-type within a particular tumor. Regardless, the accuracies using this voxel-wise approach well outperform other methods.

Although IHC methods are routinely used in the clinic, several exome sequencing studies have demonstrated that up to 15% of *IDH*-mutated gliomas remain undetected by traditional IDH1 antibody testing.[55,56] There are several molecular methods that can be used to determine IDH mutation status from tissue. The current gold-standard is the whole genome Sanger DNA sequencing method. This method, however, is limited by the amount of time, cost, and volume of tissue required to perform the genetic analysis. Next generation sequencing methods such as whole exome sequencing (WES) are able to determine mutation status much more rapidly, at decreased cost, and with reduced tissue volumes. However, these methods have false negative rates up to 6% and error rates approximately nine times that of whole genome sequencing.[66] To further understand the cases that had been misclassified by T2-net, we reviewed the data from these cases in the Cancer Genome Atlas website (CGA). There were 3 cases from the cross-fold validation sets that were misclassified by T2-net as IDH mutated. Two of these three (TCGA-CS6669, TCGA-020069) demonstrated small tissue volumes obtained during biopsy, limiting molecular characterization. This raises the possibility that the ground-truth determination of wild-type for these tumors may have been subject to tissue sampling bias (e.g., lack of an appropriate tissue sample or location of sampling).

Another factor that may explain the higher performance achieved by our networks is that previous approaches required multi-contrast input which can be compromised due to patient motion from lengthier examination times, and the need for gadolinium contrast. High quality T2-weighted images are almost universally acquired during clinical brain tumor diagnostic evaluation. Clinically, T2w images are typically acquired within 2 minutes at the beginning of the exam and

are relatively resistant to the effects of patient motion. On modern MRI scanners, high quality T2w images can even be obtained in the presence of patient motion.[52] As such, the ability to use only T2w images is a significant advantage when considering clinical translatability. This method was inspired by a similar approach used for the identification of the O6–methylguanine-DNA methyltransferase (MGMT) methylation status and prediction of 1p/19q chromosomal arm deletion.[67] Furthermore, our preprocessing steps preserve native image information without the need for any region-of-interest or tumor pre-segmentation procedures. Previous deep learning algorithms for MRI-based IDH classification use explicit tumor pre-segmentation steps. These were accomplished either by manual delineation of the tumor, or by adding a separate deep learning tumor segmentation network. The use of these pre-segmentation steps adds unnecessary complexity to the classification process, and in the case of manual pre-segmentation, makes them unworkable as a robust automated clinical workflow. Our network uniquely performs a simultaneous tumor segmentation as a natural consequence of the voxel-wise segmentation process.

3.6. Conclusion

We developed two deep-learning MRI networks for IDH-classification of gliomas: i) a T2-network and ii) a multi-contrast network with high accuracy. Both networks outperformed the state-of-the-art algorithms. We also demonstrate similar performance when comparing the T2-network with the multi-contrast network. The high accuracy of our network which utilizes only T2-weighted images will facilitate imminent clinical translation for this approach.

Acknowledgements

We thank Yin Xi, PhD, statistician for help with the ROC and AUC.

Chapter 4

A novel fully automated MRI-based deep-learning method for classification of 1p/19q co-deletion status in brain gliomas

This work is published at the journal Neuro Oncology Advances, vol 2, issue 1, doi:10.1093/noajnl/vdaa066, 2020.

Authorship: *Chandan Ganesh Bangalore Yogananda, Bhavya R Shah, Frank F Yu, Marco C Pinho, Sahil S Nalawade, Gowtham K Murugesan, Benjamin C Wagner, Bruce Mickey, Toral R Patel, Baowei Fei, Ananth J Madhuranthakam, Joseph A Maldjian*

4.1. Importance of the study

One of the most important recent discoveries in brain glioma biology has been the identification of the isocitrate dehydrogenase mutation and 1p/19q co-deletion status as markers for therapy and prognosis. 1p/19q co-deletion is the defining genomic marker for oligodendrogliomas and confers a better prognosis and treatment response than gliomas without it. Currently, the only reliable way to determine 1p/19q mutation status requires analysis of glioma tissue obtained either via an invasive brain biopsy or following open surgical resection. The ability to noninvasively determine 1p/19q co-deletion status has significant implications in determining therapy and predicting prognosis. We developed a highly accurate, deep-learning network that utilizes only T2-weighted MR images and outperforms previously published image-based methods. The high classification accuracy of our T2w image-only network (1p/19q-net) in predicting 1p/19q co-deletion status marks an important step toward image-based stratification of brain gliomas. Imminent clinical translation is feasible because T2-weighted MR imaging is widely available and routinely performed in the assessment of gliomas.

4.2. Introduction

Genetic profiling and molecular subtyping of glial neoplasms has revolutionized our ability to optimize therapeutic strategies and enhance prognostic accuracy. Perhaps the most compelling evidence supporting this paradigm is the 2016 revision of the World Health Organization's (WHO) classification of gliomas which now includes genetic analysis. The impact of glioma reclassification based on molecular profiling has subsequently been studied and three genetic alterations have been extensively validated: O-6-methylguanine-DNA methyltransferase (MGMT), Isocitrate dehydrogenase (IDH), and 1p/19q co-deletion status.[10]

MGMT is a DNA repair enzyme that protects normal and glioma cells from alkylating chemotherapeutic agents. Mutations that result in methylation of the MGMT promoter result in loss of function of the enzyme and its protective effect. Mutations of IDH alter the function of the enzyme to produce D-2-hydroxyglutarate instead of α-ketoglutarate. This altered function results in increased sensitivity of the glioma to radiation and chemotherapy. Gliomas that are IDH mutated can be further divided into gliomas with or without a 1p/19q co-deletion. The 1p/19q co-deletion is defined as the combined loss of the short arm of chromosome 1 (1p) and the long arm of chromosome 19 (19q). According to the 2016 WHO classification of gliomas, an IDH mutated glioma with a 1p/19q co-deletion is classified as an oligodendroglioma, whereas an IDH mutated glioma without a 1p/19q co-deletion is classified as a diffuse astrocytoma. Oligodendrogliomas have a better prognosis when compared to diffuse astrocytomas. Additionally, even patients with an IDH-mutated *anaplastic* oligodendroglioma (WHO grade III) have a longer median overall survival than IDH-wild type, 1p/19q non co-deleted, WHO grade II astrocytomas and are more responsive to chemotherapy.[68] Therefore, determination of 1p/19q status in IDH mutated gliomas is critical for guiding therapy and predicting prognosis. Currently, the only reliable way to

determine 1p/19q mutation status requires analysis of glioma tissue obtained either via an invasive brain biopsy or following open surgical resection. These diagnostic procedures carry the burden of implicit risk. Therefore, considerable attention has been dedicated to developing non-invasive, image-based diagnostic methods.

Recent advances in deep-learning have led to a significant interest in advancing techniques for non-invasive, image-based molecular profiling of gliomas. Our group has previously demonstrated a highly-accurate, MRI-based, voxel-wise deep-learning IDH-classification network using only T2-weighted (T2w) MR images.[69] T2w images facilitate clinical translation because they are routinely acquired, they can be obtained within 2 minutes, and high quality T2w images can even be obtained in the presence of active patient motion. Because the current standard of care for IDH mutated gliomas is heavily influenced by 1p/19q co-deletion status, the purpose of this study was to develop a highly accurate, fully automated deep-learning 3D network for 1p/19 co-deletion classification using T2-weighted images only.

4.3. Material and Methods

4.3.1. Data and Pre-processing

Multi-parametric brain MRI data of glioma patients were obtained from the Cancer Imaging Archive (TCIA) database.[53,70] Genomic information was provided from both the TCIA and TCGA (the cancer genome atlas) databases.[53,54,70] Only pre-operative studies were used. Studies were screened for the availability of 1p/19q status and T2w image series. The final dataset of 368 subjects included 268 low grade glioma (LGG, 130 co-deleted, 138 non co-deleted) and 100 high grade glioma (HGG, all non co-deleted) subjects. TCGA subject IDs, 1p/19q co-deletion status, and tumor grade are listed in Table 1 of the supplementary data.

Tumor masks for 209 subjects were available through previous expert segmentation. [3,7,69] Tumor masks for the remaining 159 subjects were generated by the 3D-IDH network[69] and validated by in-house neuro-radiologists. The tumor masks were used as ground truth for tumor segmentation in the training step. Ground truth whole tumor masks for 1p/19q co-deleted type were labelled with 1s and the ground truth tumor masks for 1p/19q non co-deleted type were labelled with 2s (Figure 9). Data preprocessing steps included (a) co-registering the T2w image to SRI24 T2 template[71] using ANTs affine registration[28], (b) skull stripping using Brain Extraction Tool (BET)[72] from FSL[72-75], (c) N4BiasCorrection to remove RF inhomogeneity[29], and (d) intensity normalization to zero-mean and unit variance. The pre-processing took less than 5 minutes per dataset.

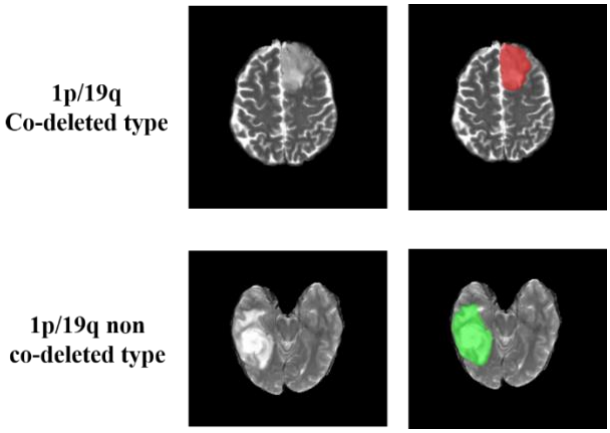

Figure 9: Ground truth whole tumor masks.
Red voxels represent 1p/19q co-deletion status (values of 1) and green voxels represent 1p/19q non-co-deletion status (values of 2). The ground truth labels have the same co-deletion status for all voxels in each tumor.

4.3.2. Network Details

Transfer learning was performed with the previously trained 3D-IDH network for 1p/19q classification.[69] The decoder part of the network was fine-tuned for a voxel-wise dual-class segmentation of the whole tumor with Classes 1 and 2 representing 1p/19q co-deleted and 1p/19q

non co-deleted type respectively. The schematics for the network architecture are shown in Figure 10B. A detailed description of the network is given in Figure 11.

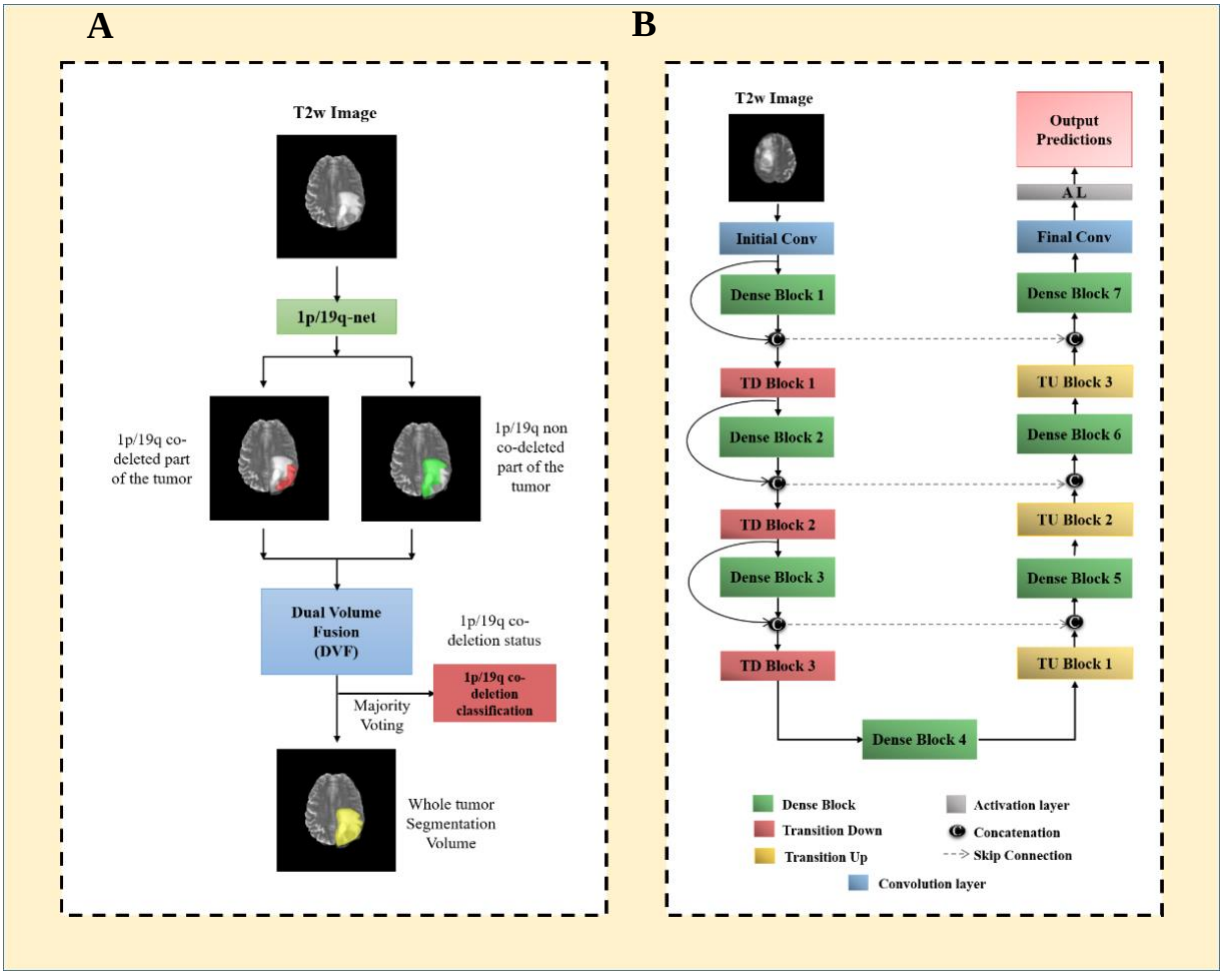

Figure 10: (A) 1p/19q-net overview.

Voxel-wise classification of 1p/19q co-deletion status is performed to create 2 volumes (1p/19q co-deleted and 1p/19q non-co-deleted). Volumes are combined using dual volume fusion to eliminate false positives and generate a tumor segmentation volume. Majority voting across voxels is used to determine the overall 1p/19q co-deletion status.

(B) Network architecture for 1p/19q-net.

3D-Dense-UNets were employed with 7 dense blocks, 3 transition down blocks, and 3 transition up blocks.

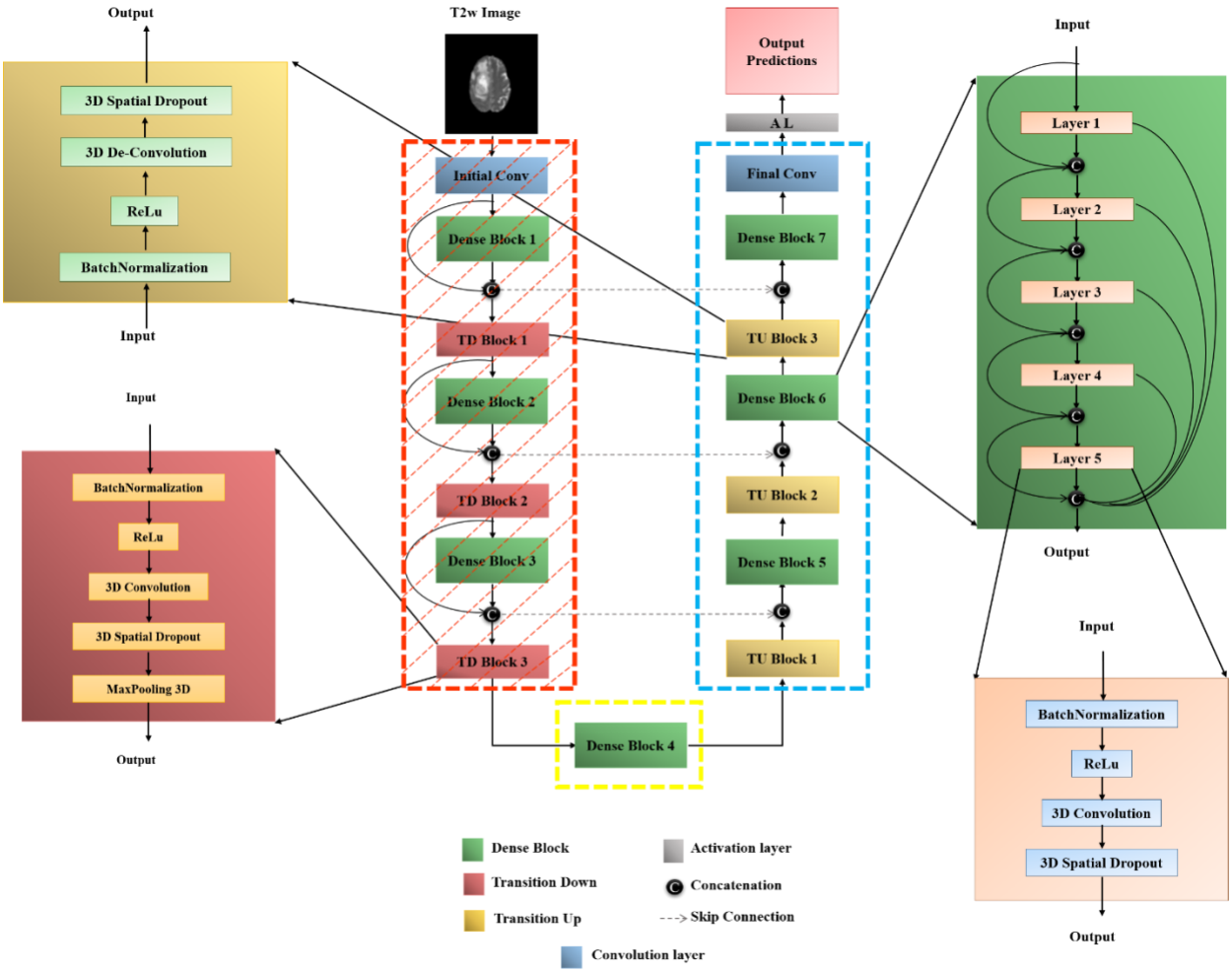

Figure 11: A Detailed network architecture for the 1p/19q-net.

The previously trained 3D IDH network was used. The left arm of the Dense U-net (striped red box) is the encoder part of the network, the right arm of the network (blue box) is the decoder part and the dense block (yellow box) is the bottle neck block. The encoder part of the network was frozen to retain the pre-trained weights from the 3D IDH network. The bottleneck block and the decoder part of the network was fine-tuned for a dual class segmentation with class 1 representing 1p/19q co-deleted type and class 2 representing 1p/19q non co-deleted type.

4.3.3. Network Implementation and Cross-validation

To generalize the reliability of the networks, a 3-fold cross-validation was performed on the 368 subjects by randomly shuffling the dataset and distributing it into 3 groups (approximately 122 subjects for each group). During each fold of the cross-validation procedure, the 3 groups were alternated between training, in-training validation and held-out testing. Group 1 had 122 subjects (43 co-deleted, 79 non co-deleted), Group 2 had 124 subjects (44 co-deleted, 80 non co-deleted),

and Group 3 had 122 subjects (43 co-deleted, 79 non co-deleted). An in-training validation dataset helps the network improve its performance during training. Each fold of the cross-validation is a new training phase based on a unique combination of the 3 groups. However, network performance is only reported on the held-out testing group for each fold as it is never seen by the network. The group membership for each cross-validation fold is listed in table 2 of the supplementary data.

Seventy-five percent overlapping patches were extracted from the training and in-training validation subjects. No patch from the same subject was mixed with the training, in-training validation or testing datasets in order to avoid the data leakage problem.[31,32] The Data augmentation steps included vertical flipping, horizontal flipping, translation rotation, random rotation, addition of Gaussian noise, addition of salt & pepper noise and projective transformation. Additionally, all images were down-sampled by 50% and 25% (reducing the voxel resolution to 2mm x 2mm x 2mm & 4mm x 4mm x 4mm) and added to the training and validation sets. Data augmentation provided a total of approximately 300,000 patches for training and 300,000 patches for in-training validation for each fold. Networks were implemented using Keras[76] and Tensorflow[33] with an Adaptive Moment Estimation optimizer (Adam).[35] The initial learning rate was set to 10^{-5} with a batch size of 15 and maximal iterations of 100. Initial parameters were chosen based on previous work with Dense-UNets on brain imaging data & semantic segmentation.[57,69,77]

1p/19q-net yields two segmentation volumes. Volume 1 provides the voxel-wise prediction of 1p/19q co-deleted tumor and Volume 2 identifies the predicted 1p/19q non co-deleted tumor voxels. A single tumor segmentation map is obtained by fusing the two volumes and obtaining the largest connected component using a 3D connected component algorithm in MATLAB(R). Majority voting over the voxel-wise classes of co-deleted type or non co-deleted type provided a single 1p/19q classification for each subject. Networks were implemented on Tesla V100s, P100,

P40 and K80 NVIDIA-GPUs. The 1p/19q classification process developed is fully automated, and a tumor segmentation map is a natural output of the voxel-wise classification approach.

4.3.4. Statistical Analysis

MATLAB(R) and R were used for statistical analysis of the network's performance. Majority voting (*i.e.* voxel-wise cutoff of 50%) was used to evaluate the accuracy of the network. The accuracy, sensitivity, specificity, positive predictive value (PPV), and negative predictive value (NPV) of the model for each fold of the cross-validation procedure were calculated using this threshold. A Dice-score was used to evaluate the performance of the networks for tumor segmentation. The Dice-score calculates the amount of spatial overlap between the ground truth segmentation and the network segmentation. A Receiver Operating Characteristic (ROC) curve was also generated for each fold.

4.3.4.1. ROC methodology

The network output classifies voxels in the tumor as 1p/19q co-deleted or non co-deleted type. The percent of co-deleted voxels was computed for the network output for each subject in the test set by dividing the predicted co-deleted voxels by the total number of predicted voxels in each tumor. The percent co-deleted voxels can be viewed as a network output prediction likelihood of the tumor being 1p/19q co-deleted. Note that majority voting (the 50% threshold) was used to determine 1p/19q co-deletion status prediction. For the ROC analysis, the percent of co-deleted voxels was sorted and used as separate thresholds (cut-points) to determine 1p/19q co-deletion status for the subjects across the test set for each new cut-point. The resulting predicted 1p/19q class membership was compared to the ground truth values to determine sensitivity (true positive rate) and 1- specificity (false positive rate) at each threshold. The resulting values were plotted using Matlab to obtain an ROC curve (true positive rate against false positive rate). Matlab routines

were used to fit the curves and determine the area under the curve (AUC). This procedure was repeated for each of the 3 test folds from the cross-validation procedure for the 1p/19q-net, providing a total of 3 ROC curves from the cross-validation.

4.4. Results

4.4.1. 1p/19q-net

The network achieved a mean cross-validation testing accuracy of 93.46% across the 3 folds (93.4%, 94.35%, and 92.62%, standard dev=0.8). Mean cross-validation sensitivity, specificity, PPV, NPV and AUC for 1p/19q-net was 0.90 ±0.003, 0.95 ±0.01, 0.91 ±0.02, 0.95 ±0.0003 and 0.95 ±0.01 respectively (Table 5). The mean cross-validation Dice-score for tumor segmentation was 0.80 ± 0.007. The network misclassified 8, 7 and 9 cases for each fold respectively (24 total out of 368 subjects). Twelve subjects were misclassified as non co-deleted, and 12 as co-deleted.

Table 5: 1p/19q-net Cross-Validation Results

Fold Description	**1p/19q-net**		
Fold Number	**%Accuracy**	**AUC**	**Dice-score**
Fold 1	93.4	0.9571	0.8151
Fold 2	94.35	0.9688	0.8057
Fold 3	92.62	0.9351	0.8000
AVERAGE	**93.46 +/- 0.86**	**0.953 +/- 0.01**	**0.801 +/- 0.007**

4.4.2. ROC Analysis

The ROC curves for each cross-validation fold for the network is provided in Figure 12. The network demonstrated very good performance curves with high sensitivities and specificities.

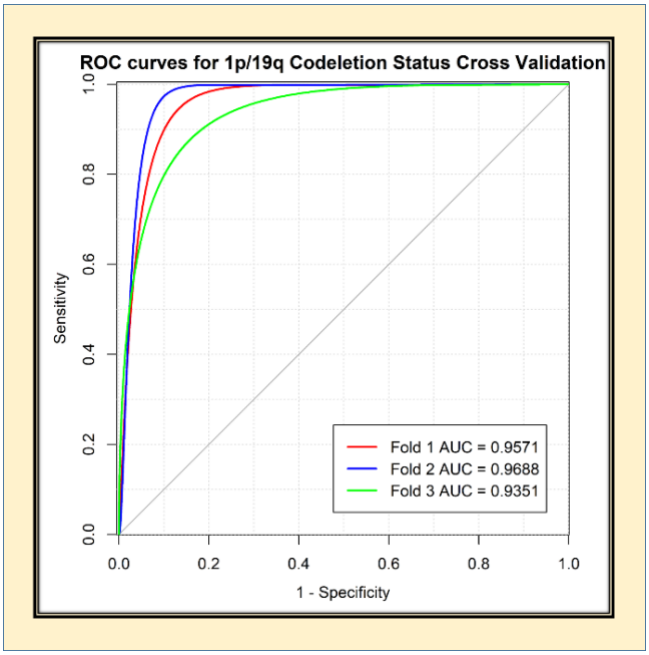

Figure 12: ROC analysis for 1p/19q-net.
Separate curves are plotted for each cross-validation fold along with corresponding area under the curve value

4.4.3. Voxel-wise classification

Since the network is a voxel-wise classifier, it performs a simultaneous tumor segmentation. Figures 13A and 13B show examples of the voxel-wise classification for a co-deleted type, and non co-deleted type respectively using the network. The volume fusion procedure was effective in removing false positives to increase accuracy. This procedure improved the dice-scores by approximately 4% for the network. We also computed the voxel-wise accuracy for the network. The mean voxel-wise accuracies were 85.86% ±0.01 for non co-deleted type and 80.51% ±0.01 for co-deleted type.

4.4.4. Training and Segmentation times

It took approximately 1 week to fine-tune the decoder portion of the network. The trained network took approximately three minutes to segment the whole tumor and predict the 1p/19qco-deletion status for each subject.

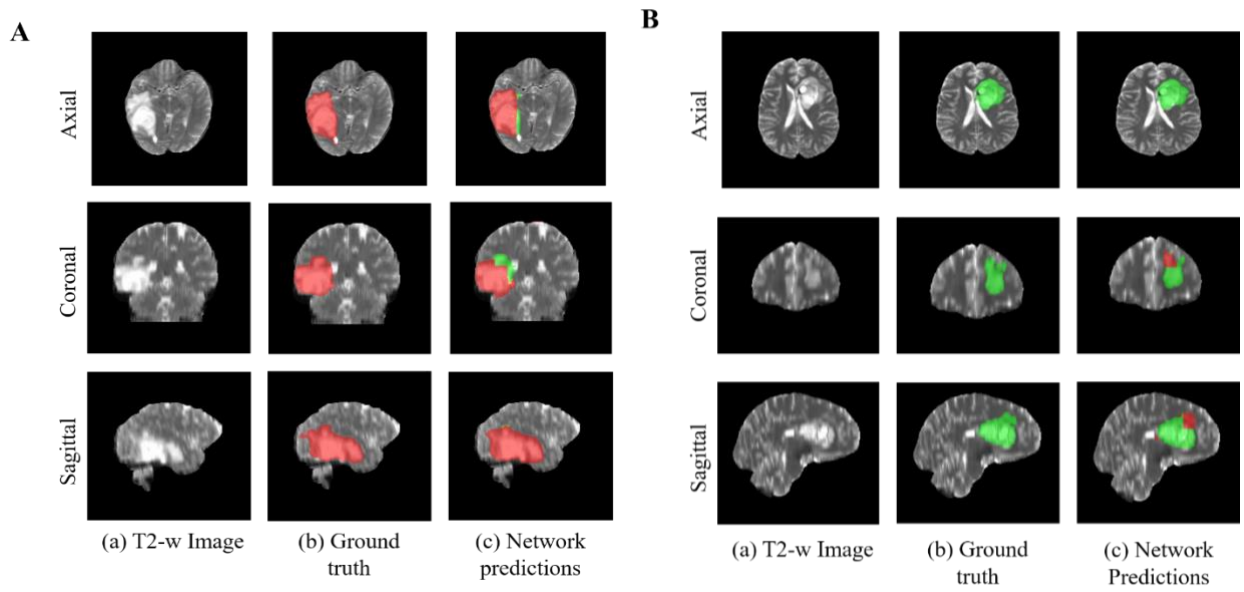

Figure 13: (A) Example of voxel-wise segmentation for a 1p/19q co-deleted tumor: *native T2 image (a), ground truth segmentation (b), and network output after DVF (c). Red voxels correspond to 1p/19q co-deleted class and green voxels correspond to 1p/19q non-co-deleted class.* ***(B) Example of voxel-wise segmentation for a 1p/19q non-co-deleted tumor.*** *The sharp borders visible between co-deleted and non-co-deleted types result from the patch-wise classification approach.*

4.5. Discussion

We developed a fully-automated, highly accurate, deep-learning network that outperforms previously reported 1p/19q co-deletion status classification algorithms.[51,78-80] When comparing our T2-network with previous work, our results suggest that algorithm accuracy can be improved by using T2-weighted images only. Clinical translation becomes much simpler using only T2 weighted images because these images are routinely acquired and are robust to motion. When compared to previously published algorithms, our methodology is fully-automated. The time required for 1p/19q-net to segment the whole tumor and predict the 1p/19q co-deletion status for one subject is approximately 3 minutes on a K80, P40, P100 or V100s NVIDA-GPU.

The higher performance achieved by our network when compared to previous work is likely due to several factors. Similar to our IDH classification network we employed 3D networks whereas prior attempts at 1p/19q co-deletion status classification have relied on 2D networks.[78]

The dense connections in a 3D network architecture are advantageous because they carry information from all the previous layers to the following layers.[77] Additionally, 3D networks are easier to train and can reduce over-fitting.[81] As we previously reported, the Dual Volume Fusion (DVF) post-processing step helps in effectively eliminating false positives while improving the segmentation accuracy by excluding extraneous voxels not connected to the tumor. DVF improved the dice-scores by approximately 4% for the network. The 3D networks interpolate between slices to maintain inter-slice information more accurately. The network does not require extraction of pre-engineered features from the images or histopathological data.[58] Our approach also uses voxel-wise classifiers and provides a classification for each voxel in the image. This provides a simultaneous single-label tumor segmentation. Another factor that may explain the higher performance achieved by our network is that previous approaches required multi-contrast input which can be compromised due to patient motion from lengthier examination times, and the need for gadolinium contrast. High quality T2-weighted images are almost universally acquired during clinical brain tumor diagnostic evaluation. Clinically, T2w images are typically acquired within 2 minutes at the beginning of the exam and are relatively resistant to the effects of patient motion. Several of the previous 1p/19q deep learning studies were trained and tested on only low-grade gliomas achieving accuracies ranging from 65.9% - 87.7%.[78-80] Our algorithm was trained and evaluated on a mix of high grade and low-grade gliomas, which is a better representative of real-world performance and potential clinical utilization.

In the clinical setting, histologic evaluation remains the gold standard for genetic profiling of gliomas. Several different methods to detect 1p/19q co-deletion have been employed: fluorescence in-situ hybridization (FISH), array comparative genomic hybridization, multiplex ligation dependent probe amplification, and PCR-based loss of heterozygosity analysis.[82] FISH is the most

routinely performed method.[83] FISH relies on fluorescent labeled DNA probes to directly detect chromosomal abnormalities on a tissue slide in interphase nuclei.[84] The fraction of nuclei that demonstrate a deletion or relative deletion (in cases with polysomy) are summed and a percentage is calculated.[85] When the percentage of "deleted" nuclei exceeds a pre-determined cut-off, the tumor is classified as 1p/19q co-deleted.[85] A drawback of FISH is that it lacks standardized criteria for analysis of 1p/19qco-deletion status.[83] For example, there is no consensus on what cut-off level to use when classifying co-deletion status. As a result, variability in institutional-based cut-off values can span from 20% to 70% and can affect accurate diagnosis.[85] This limitation affects the sensitivity, specificity, PPV, and NPV of 1p/19q detection by FISH based on the cut-off value selected.[85]

There are interesting parallel considerations when studying our deep-learning method of 1p/19q determination. Our network is a voxel-wise classifier and as a result some portions within each glioma are classified as 1p/19 co-deleted while other areas are 1p/19q non co-deleted. The overall determination of 1p/19q co-deletion status is based on the majority of voxels in the tumor. Given the variability in the cut-off values for FISH detection of 1p/19q co-deletion, we performed a Youden's statistical index analysis to determine if the optimal cut-off for our deep learning algorithm was different than majority voting (>50%). The analysis demonstrated that maximum accuracy, sensitivity, specificity, PPV, and NPV were obtained at an optimal cut-off of 50%, the same as majority voting.

The algorithm misclassified 24 cases: 12 subjects were misclassified as non co-deleted and 12 as co-deleted. Despite these misclassifications, our network achieved a mean cross-validation testing accuracy of 93.46% which is similar to what is reported for FISH.[85] However, our sensitivity, specificity, PPV, and NPV were significantly better than when compared to FISH.[30]

While FISH requires tissue to be obtained from an invasive procedure and subsequent tissue processing for at least 48 hours, our deep learning algorithm can segment the entire glioma and provide a 1p/19q co-deletion status in 3 minutes. The deep learning algorithm can also be fine-tuned to variations in institutional MRI scanners, while FISH analysis currently lacks standardization as mentioned above.

The limitations of our study are that deep learning studies require large amounts of data and the relative number of subjects with 1p/19q co-deletions is small. Additionally, acquisition parameters and imaging vendor platforms vary across imaging centers that contribute data. Despite these caveats our algorithm demonstrated high 1p/19q co-deletion classification accuracy.

4.6. Conclusion

We demonstrate high 1p/19q co-deletion classification accuracy using only T2-weighted MR images. This represents an important milestone toward using MRI to predict glioma histology, prognosis, and response to treatment.

Acknowledgements

We thank Yin Xi, PhD, statistician for help with the ROC and AUC.

Chapter 5

MRI Based Deep Learning Method for Determining Glioma MGMT promoter Methylation Status

This work is published at the American journal of Neuroradiology, ISSN: 1936-959X, doi: 10.3174/ajnr.A7029, 2021.

Authorship: *Chandan Ganesh Bangalore Yogananda, Bhavya R. Shah, Sahil S. Nalawade, Gowtham K. Murugesan, Frank F. Yu, Marco C. Pinho, Benjamin C. Wagner, Bruce Mickey, Toral R. Patel, Baowei Fei, Ananth J. Madhuranthakam, Joseph A. Maldjian*

5.1. Introduction

O^6-methylguanine-DNA methyltransferase (MGMT) promoter methylation is a molecular biomarker of gliomas that has prognostic and therapeutic implications. Unlike isocitrate dehydrogenase (IDH) mutations and 1p/19q co-deletions, MGMT promoter methylation is an *epigenetic* event. Epigenetic events are functionally relevant but do not involve a change in the nucleotide sequence. Therefore, while MGMT promoter methylation is an important prognostic marker, it does not define a distinct subset of gliomas. MGMT is a DNA repair enzyme that protects normal and glioma cells from alkylating chemotherapeutic agents. The methylation of the MGMT promoter is an example of *epigenetic silencing* which results in loss of function of the MGMT enzyme and its protective effect on glioma cells. The survival benefit incurred by MGMT promoter methylation in patients treated with temozolomide (TMZ) was determined in 2005.[86] Subsequent work by Stupp et al. has shown that in patients who received both radiation and temozolomide, *MGMT* promoter methylation improved median survival as compared to patients with unmethylated gliomas (21.7 months vs 12.7 months).[87,88] Long-term follow-up from that

initial study has further substantiated the survival benefit.[87,88] As a result, determining MGMT promoter methylation status is an important step in predicting survival and determining treatment.

Currently, the only reliable way to determine MGMT promoter methylation status requires analysis of glioma tissue obtained either via an invasive brain biopsy or following open surgical resection. Surgical procedures carry the risk of neurologic injury and complications. Therefore, considerable attention has been dedicated to developing non-invasive, image-based diagnostic methods to determine MGMT promoter methylation status. A meta-analysis of MRI features demonstrated that glioblastomas with methylated MGMT promoters were associated with less edema, high apparent diffusion coefficient (ADC), and low perfusion. However, the summary sensitivity and specificity of these clinical features was only 79% and 78% respectively.[89] Although multiple radiomic approaches have also been attempted for MGMT prediction, none to date have achieved accuracies sufficient for clinical viability.[67,90-93] Sasaki et al. attempted to establish an MRI-based radiomic model for predicting MGMT promoter status of the tumor but only reached a predictive accuracy of 67%.[94] Wei et al. extracted radiomic features from the tumor and peritumoral edema using multi-sequence, post-contrast MRI but only achieved an accuracy of 51-74% in predicting MGMT promoter methylation status in astrocytomas.[95] Drabycz performed texture analysis on MRI images to predict MGMT promoter methylation status in glioblastoma but only reached an accuracy of 71%.[90] Korfiatis combined texture features with supervised classification schemes as potential imaging biomarkers for predicting the MGMT methylation status of GBM but only achieved a sensitivity and specificity of 0.803 and 0.813 respectively.[67] Ahn used dynamic contrast-enhanced MRI and diffusion tensor imaging to predict MGMT promoter methylation in glioblastoma but this method only achieved a sensitivity and specificity of 56.3% and 85.2% respectively.[92]

Recent advances in deep-learning methods have also been used for non-invasive, image-based molecular profiling. Our group has previously demonstrated highly-accurate, MRI-based, voxel-wise deep-learning networks for determining IDH-classification and 1p/19q co-deletion status using only T2-w MR images.[69,96] The benefits of using T2-w images are that they are routinely acquired, they can be obtained quickly, and high quality T2-w images can even be obtained in the setting of motion degradation. Because MGMT promoter methylation in gliomas is such an important biomarker, we sought to develop a highly accurate, fully automated deep-learning 3D network for MGMT promoter methylation status determination using T2-w images only.

5.2. Material and Methods

5.2.1. Data and Pre-processing

Multi-parametric MR Images of brain glioma patients were obtained from the TCIA (The Cancer Imaging Archive) database.[53,97] The genomic information was obtained from both TCGA (the cancer genome atlas) and TCIA databases.[53,54,70] Subject datasets were screened for the availability of pre-operative MR images, T2-w images and known MGMT promoter status. The final dataset of 247 subjects included 163 methylated cases and 84 unmethylated cases. TCGA subject IDs, MGMT status, and tumor grade are listed in Table 1 of the supplementary data.

Tumor masks for 179 subjects were available through previous expert segmentation.[3,7,69] Tumor masks for the remaining 68 subjects were generated by our previously trained 3D-IDH network and were reviewed by 2 neuroradiologists for accuracy.[69] These tumor masks were used as ground truth for tumor segmentation in the training step. Ground truth whole tumor masks for methylated and unmethylated MGMT promoter type were labelled with 1s & 2s respectively (Figure 14). Data preprocessing steps included (a) ANTs affine co-registration[28] to the SRI24 T2 template[71], (b) skull stripping using the Brain Extraction Tool (BET)[72] from FSL[72-75], (c)

Removing RF inhomogeneity using N4BiasCorrection[29], and (d) normalizing intensity to zero-mean and unit variance. The pre-processing took less than 5 minutes per dataset.

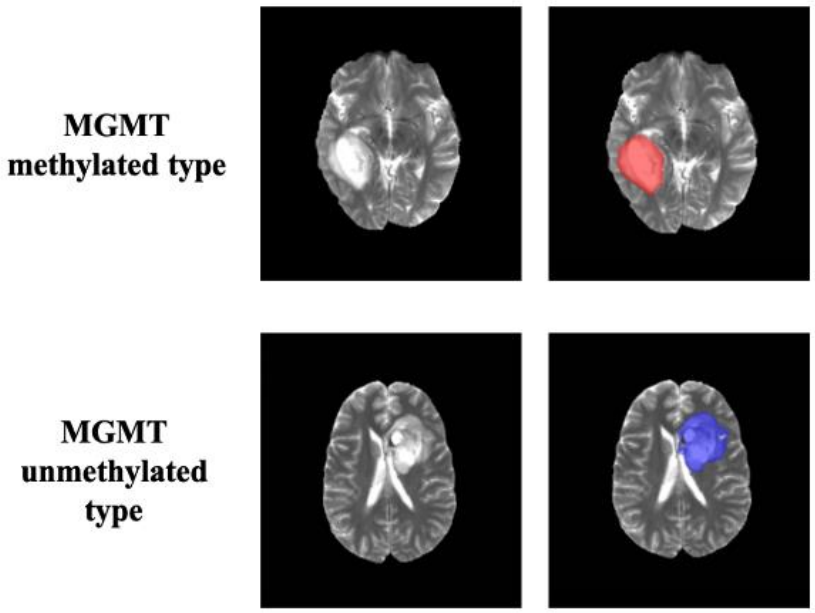

Figure 14: Ground truth whole tumor masks.
Red voxels represent methylated MGMT promoter status (values of 1) and blue voxels represent unmethylated MGMT promoter status (values of 2). The ground truth labels have the same MGMT promoter status for all voxels in each tumor.

5.2.2. Network Details

Transfer learning for MGMT promoter status determination was implemented using our previously trained 3D-IDH network.[69] The decoder part of the network was fine-tuned for a voxel-wise dual-class segmentation of the whole tumor with Classes 1 and 2, representing methylated & unmethylated MGMT promoter type, respectively. The network architecture is shown in Figure 15B. A detailed schematic of the network is provided in Figure 16.

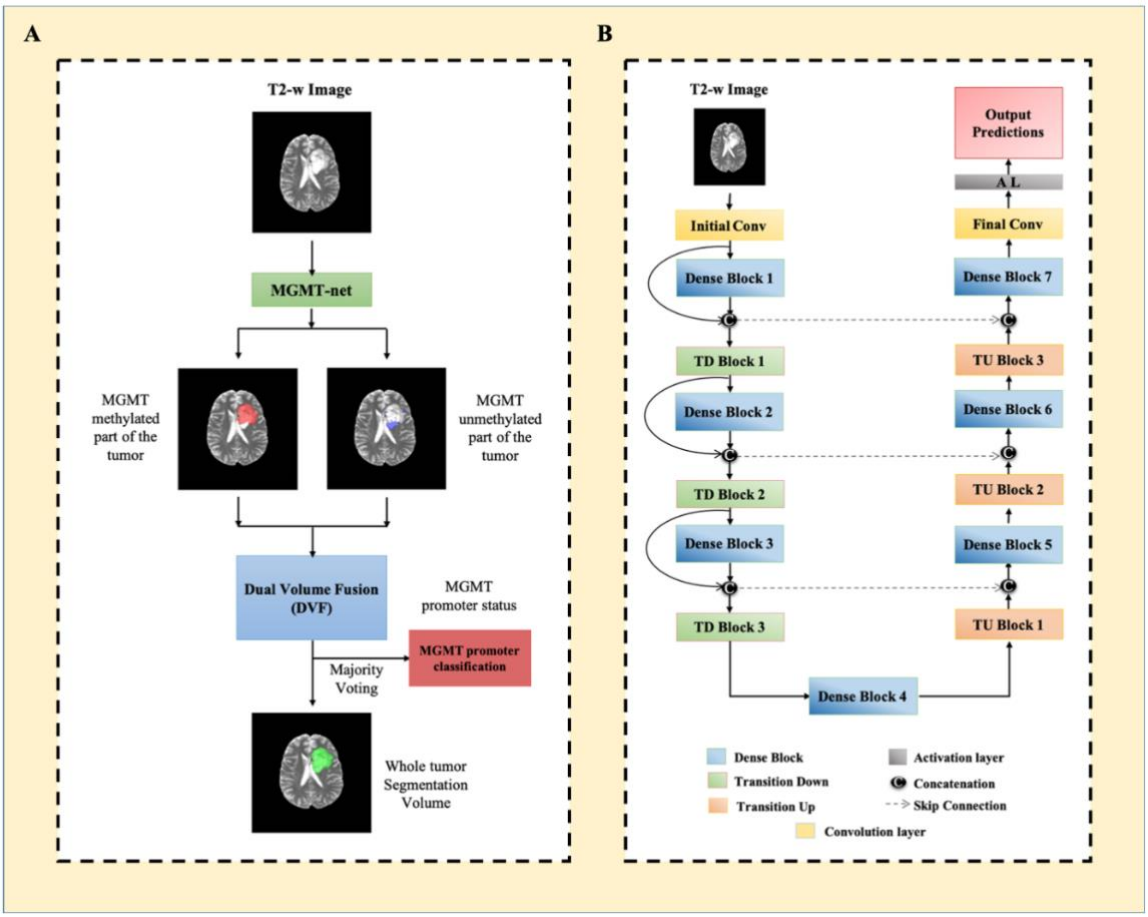

Figure 15: (A) MGMT-net overview. *Voxel-wise classification of MGMT promoter status is performed to create 2 volumes (methylated and unmethylated MGMT promoter). Volumes are combined using dual volume fusion to eliminate false positives and generate a tumor segmentation volume. Majority voting across voxels is used to determine the overall MGMT promoter status.*

(B) Network architecture for MGMT-net. *3D-Dense-UNets are employed with 7 dense blocks, 3 transition down blocks, and 3 transition up blocks.*

5.2.3. Network Implementation and Cross-validation

To generalize the network's performance, a 3-fold cross-validation was performed. The dataset of 247 subjects was randomly shuffled and distributed it into 3 groups (approximately 82 subjects for each group). Group 1 had 82 subjects (54 methylated, 28 unmethylated), Group 2 had 83 subjects (55 methylated, 28 unmethylated), and Group 3 had 82 subjects (54 methylated, 28 unmethylated). The 3 groups were alternated between training, in-training validation, and held-out testing groups such that each fold of the cross-validation was a new training phase based on a unique combination

of the 3 groups. The network uses the in-training validation dataset to evaluate its learning after each training round and update model parameters to improve performance. However, the network performance is only reported on the held-out testing group for each fold as it is never seen by the network. The group membership for each cross-validation fold is listed in table 3 of the supplementary data.

Seventy-five percent overlapping 3D patches (size: 32x32x32) were extracted from the training and in-training validation dataset. The patch extraction was performed as a translation in the x-y-z plane. During training, only patches with at least 1 tumor voxel were included, thus the number of patches included per training case varied depending on the size of the tumor. For testing however, the entire image was sampled including background masked voxels (of value 0). To prevent the problem of data leakage, no patch from the same subject was mixed with the training, in-training validation or testing datasets.[31,32] Data augmentation steps included horizontal & vertical flipping, random & translational rotation, addition of salt & pepper noise, addition of Gaussian noise, and projective transformation. Additional data augmentation steps included down-sampling images by 50% and 25% (reducing the voxel resolution to $2mm^3$ and $4mm^3$). The data augmentation provided a total of approximately 300,000 patches for training and 300,000 patches for in-training validation for each fold. The networks were implemented using Tensorflow[33] backend engine, Keras[76] python package, and an Adaptive Moment Estimation optimizer (Adam).[35] The initial learning rate was set to 10^{-5} with a batch size of 15 and maximal epochs of 100 for each fold.

MGMT-net outputs two segmentation volumes (V1 and V2), which are combined to generate the voxel-wise prediction of methylated & unmethylated MGMT promoter tumor voxels, respectively. The two volumes are fused, and the largest connected component (3D-connected

component algorithm in MATLAB(R)) is obtained as the single tumor segmentation map. Majority voting over the voxel-wise classes of methylated or unmethylated type provided a single MGMT promoter classification for each subject. Tesla V100s, P100, P40 and K80 NVIDIA-GPUs were used to implement the networks. This MGMT promoter determination process is fully automated, and a tumor segmentation map is a natural output of the voxel-wise classification approach.

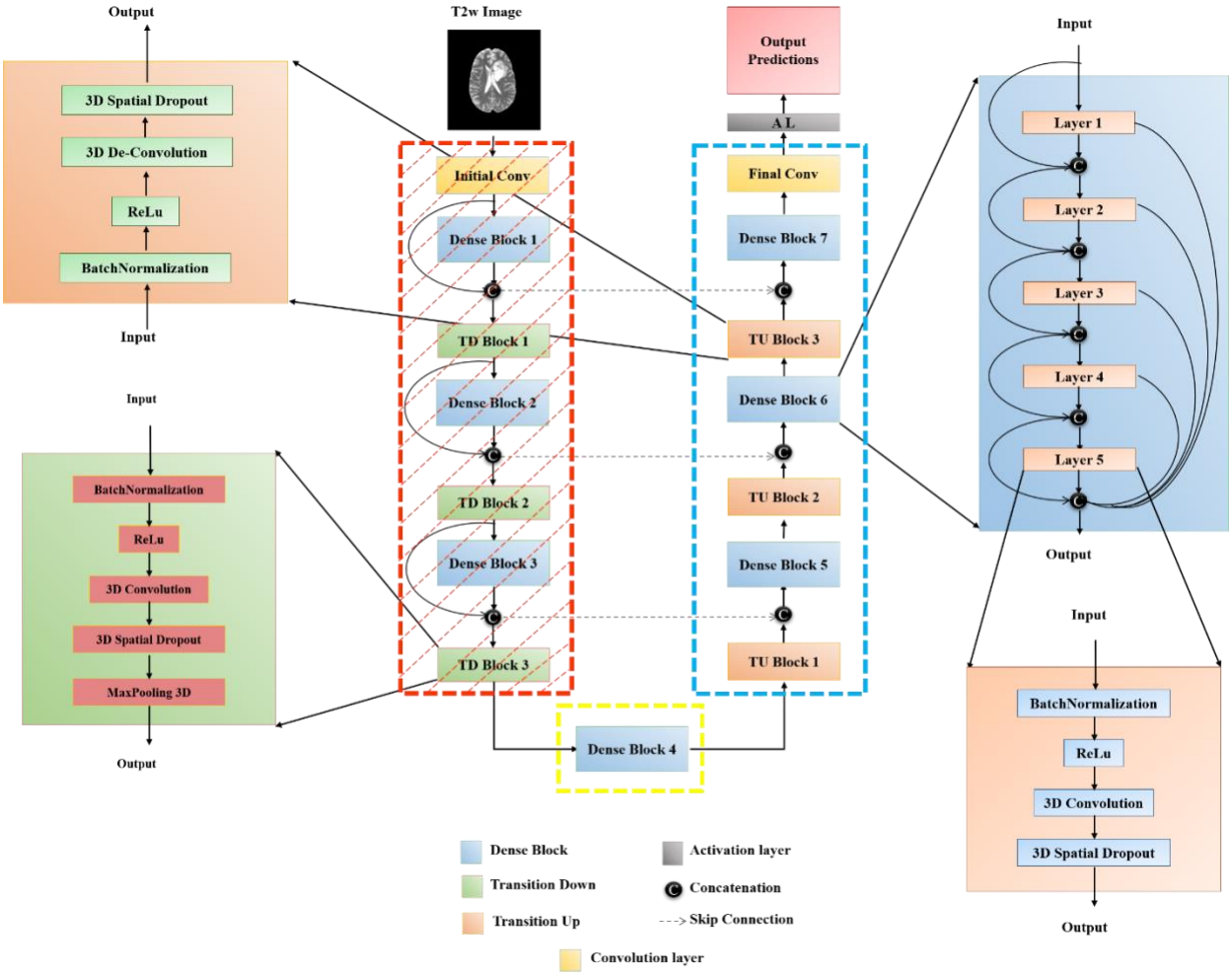

Figure 16: A Detailed network architecture for the MGMT-net.

The previously trained 3D IDH network was used. The left arm of the Dense U-net (striped red box) is the encoder part of the network, the right arm of the network (blue box) is the decoder part and the dense block (yellow box) is the bottle neck block. The encoder part of the network was frozen to retain the pre-trained weights from the 3D IDH network. The bottleneck block and the decoder part of the network was fine-tuned for a dual class segmentation with class 1& 2 representing methylated & unmethylated MGMT promoter status respectively.

5.2.4. Statistical Analysis

Statistical analysis of the network's performance was performed in MATLAB(R) and R. Network accuracies were evaluated using majority voting (*i.e.* voxel-wise cutoff of 50%). The accuracy, sensitivity, specificity, positive predictive value (PPV), and negative predictive value (NPV) of the model for each fold of the cross-validation procedure were calculated using this threshold. Dice-scores were calculated to evaluate the tumor segmentation performance of the networks. The Dice-score calculates the spatial overlap between the ground truth segmentation and the network segmentation. Receiver Operating Characteristic (ROC) curves for each fold were generated separately.

5.2.4.1. ROC methodology

The network output classifies voxels in the tumor as methylated or unmethylated MGMT promoter type. The percent of methylated voxels was computed for the network output for each subject in the test set by dividing the predicted methylated voxels by the total number of predicted voxels in each tumor. The percent methylated voxels can be viewed as a network output prediction likelihood of the tumor being MGMT methylated. Note that majority voting (the 50% threshold) was used to determine MGMT promoter status. For the ROC analysis, the percent of methylated voxels was sorted and used as separate thresholds (cut-points) to determine the MGMT promoter status for the subjects across the test set for each new cut-point. The resulting predicted MGMT promoter class membership was compared to the ground truth values to determine sensitivity (true positive rate) and 1- specificity (false positive rate) at each threshold. The resulting values were plotted using R to obtain an ROC curve (true positive rate against false positive rate). R routines were used to fit the curves and determine the area under the curve (AUC). This procedure was

repeated for each of the 3 test folds from the cross-validation procedure for the MGMT-net, providing a total of 3 ROC curves from the cross-validation.

5.3. Results

5.3.1. MGMT-net

The network achieved a mean cross-validation testing accuracy of 94.73% across the 3 folds (95.12%, 93.98%, and 95.12%, standard dev=0.66). Mean cross-validation sensitivity, specificity, PPV, NPV and AUC for MGMT-net was 96.31% ±0.04, 91.66% ±2.06, 95.74% ±0.95, 92.76% ±0.15 and 0.93 ±0.03 respectively. The mean cross-validation Dice-score for tumor segmentation was 0.82 ± 0.008 (Table 6). The network misclassified 4 cases for fold one, 5 cases for fold two, and 4 cases for fold three (13 total out of 247 subjects). Six subjects were misclassified as unmethylated, and 7 as methylated.

Table 6: MGMT-net Cross-validation results

Fold Description	**MGMT-net**		
Fold Number	**% Accuracy**	**AUC**	**Dice-score**
Fold 1	95.12	0.9574	0.8140
Fold 2	93.98	0.8978	0.8165
Fold 3	95.12	0.9390	0.8291
AVERAGE	**94.73 +/- 0.66**	**0.93 +/- 0.03**	**0.82 +/- 0.008**

5.3.2. ROC analysis

The ROC curves for each cross-validation fold for the network is provided in Figure 17. The network demonstrated very good performance with high sensitivities and specificities.

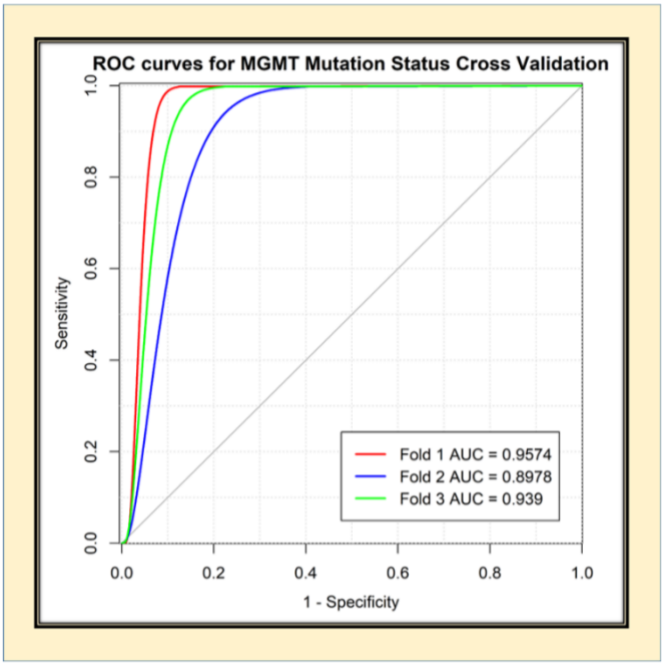

Figure 17: ROC analysis for MGMT-net.
Separate curves are plotted for each cross-validation fold along with corresponding AUC value.

5.3.3. Voxel-wise classification

The network is a voxel-wise classifier with the tumor segmentation map being a natural output. Figures 18A and 18B show examples of the voxel-wise classification for a methylated, and unmethylated MGMT promoter type respectively. The volume fusion procedure was effective in removing false positives and improving the dice-scores by approximately 6%. We also computed the voxel-wise accuracy for the network. The mean voxel-wise accuracies were 81.68% ±0.02 for methylated type and 70.83% ±0.04 for unmethylated type.

5.3.4. Training and segmentation times

Fine-tuning the network took approximately one week. The trained network took approximately three minutes to segment the whole tumor and determine the MGMT status for each subject.

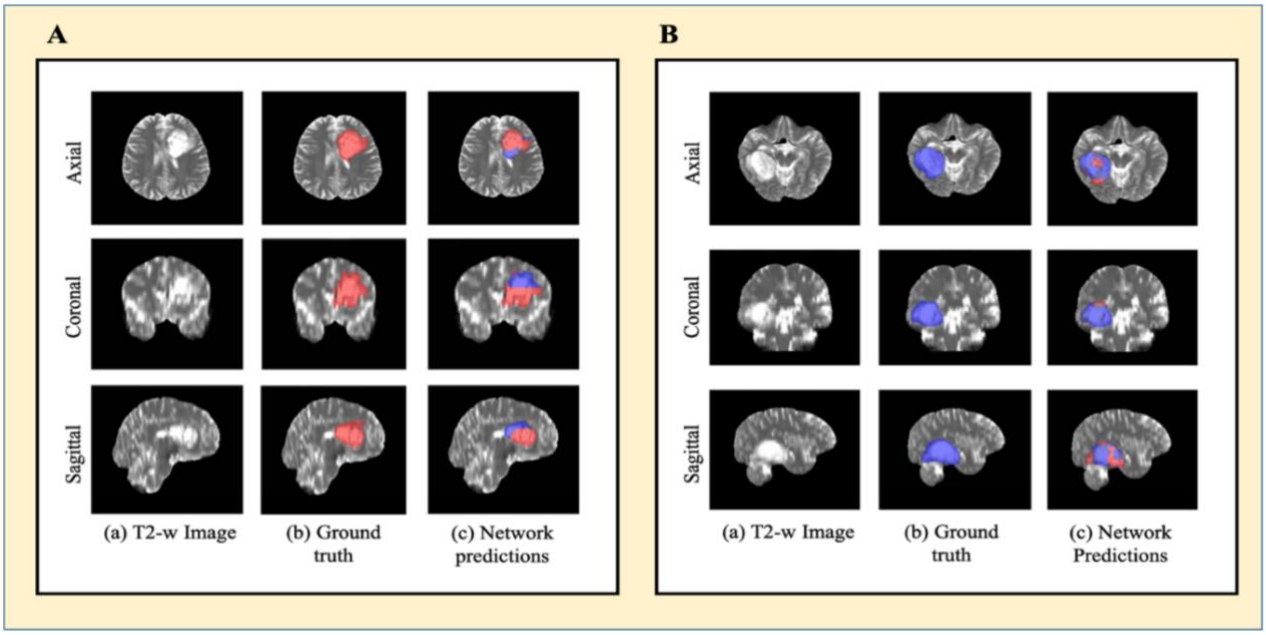

Figure 18: (A) Example of voxel-wise segmentation for a tumor with a methylated MGMT promoter. *Native T2-w image (a). Ground truth segmentation (b). Network output after DVF (dual volume fusion) (c). Red voxels correspond to MGMT methylated class and blue voxels correspond to MGMT unmethylated class.*

(B) Example of voxel-wise segmentation for a tumor with an unmethylated MGMT promoter. *The sharp borders visible between methylated and unmethylated type result from the patch-wise classification approach.*

5.4. Discussion

We developed a fully-automated, highly accurate, deep-learning network for determining the methylation status of the MGMT promoter that outperforms previously reported algorithms.[51,98,99] Our network is able to determine MGMT promoter methylation status from T2-w images alone. This eliminates potential failures from image acquisition artifacts and makes clinical translation straightforward because T2-w images are routinely obtained as part of standard clinical brain MRI. Previous approaches have required multi-contrast input which can be compromised due to patient motion from lengthier examination times, and the need for gadolinium contrast. Obviating the need for intravenous contrast makes our algorithm applicable to patients with contrast allergies and renal failure. When compared to previously published algorithms, our methodology is fully automated and utilizes minimal preprocessing. The time required for MGMT-net to segment the

whole tumor and predict the MGMT promoter methylation status for one subject is approximately 3 minutes on a K80 or P40 NVIDA-GPU.

Other groups have also proposed deep-learning methods for non-invasive, image-based MGMT molecular profiling but each of these has significant limitations. Korfiatis et al implemented a 2D-based slice-wise network, pre-selecting only GBM cases for training and prediction.[67] While they achieved a high slice-wise accuracy, their average subject-wise MGMT prediction accuracy was only 90%. Importantly, in clinical practice the tumor grade is unknown *a priori*. Thus, the Korfiatis approach is a non-viable clinical method from the outset. Our approach of using a mix of LGG and HGG is a better approximation of the real-work clinical workflow where tissue is not yet available.[67] Similar to the Korfiatis work, Chang et al. also implemented a 2D-network, but instead used a case mix like ours (LGG and HGG from the TCIA/TCGA). However, they were only able to achieve an MGMT prediction accuracy of 83% (range of 76%-88%) and their network required tumor pre-segmentation.[51] Our algorithm far outperformed the Chang approach on a similar data set without the need for pre-segmentation. Additionally, it is unclear if either the Korfiatis or the Chang 2D algorithms addressed the issue of "data leakage".[31,32] This is a potentially significant limitation for 2D networks that can occur during the slice-wise randomization process if different slices of the same tumor from the same subject are mixed between training, validation, and testing data sets. Unless this is explicitly addressed during the slice randomization procedure, the reported accuracies can be upwardly biased. Our approach outperforms all prior reports on noninvasive determination of MGMT status and is the first to achieve tissue-level performance, representing a milestone in the clinical viability of MRI-based MGMT promoter status prediction.

The higher performance achieved by our network compared to previous image-based classification studies can be explained by several factors. The dense connections in our 3D network architecture are easier to train, carry information from the previous layers to the following layers, and can reduce over-fitting.[77,81] 3D networks also interpolate between slices to maintain inter-slice information more accurately. The Dual Volume Fusion (DVF) post-processing step improved the dice-scores by approximately 6% by eliminating extraneous voxels not connected to the tumor. Our approach also uses voxel-wise classifiers and provides a classification for each voxel in the image. This provides a simultaneous single-label tumor segmentation. The cross validation single label whole tumor segmentation performance for the MGMT network provided excellent Dice-scores of 0.82 +/- 0.008.

The ability to determine MGMT promoter methylation status based on MR images alone is clinically significant because it helps determine whether the glioma will be susceptible to temozolomide (TMZ). Alkylating agents such as TMZ, damage DNA by methylating the oxygen at position 6 of the guanine nucleotide (O^6-methylguanine). The process by which many DNA repair enzymes remove O^6-methylguanine, results in DNA breaks culminating in cell death. However, MGMT works differently by restoring the normal guanine residue and rescuing the glioma cell. Therefore, MGMT activity leads to resistance to therapy. Methylation of the MGMT promoter leads to inactivation of MGMT and loss of resistance of glioma cells to alkylating agents. The MGMT protein is encoded on the long arm of chromosome 10 at position 26 (10q26). Transcription of the MGMT gene is regulated by several promoters.[29]

Although incompletely understood, at least nine specific regions within the promoter's gene determine whether a cell will express or not express MGMT.[29] However, some regions have been shown to be more important for loss of MGMT expression.[100] In the clinical setting, methods for

determining MGMT methylation focus on these regions in the promoter's gene. The four most prevalent methods to detect MGMT methylation are: immunohistochemistry (IHC), pyrosequencing (PYR), quantitative methylation-specific PCR (qMSP), and methylation-specific PCR (MSP). PYR is considered the theoretical "gold-standard" but is not readily available, and although it is quantitative, there is no agreement on what "cut-off" values to use when determining MGMT promoter methylation status.[30] Therefore, although it is not quantitative, MSP is the most widely used method.[101] Additionally, most centers perform MGMT methylation detection on formalin-fixed or paraffin embedded tissue specimens. These methods have several limitations. Evaluating multiple different methylation sites is technically challenging on a single tissue specimen.[101] Tumor heterogeneity poses a substantial limitation for these methods because sampling-bias can lead to inaccurate determinations. The presence of hemorrhage, necrosis, or nonmalignant cells contaminate the specimen[101]. Therefore, some institutions mandate that at least 50% of the sample to be analyzed contains tumor cells. Prior to PCR, several tissue processing steps are required. Bisulfite treatment is the most critical step because it will produce the modified DNA that will be used for PCR; however, it also degrades the amount of DNA available and incomplete treatments can lead to false-positive results.[101] The reported sensitivity and specificity of MSP is 91% and 75% respectively, while the reported sensitivity and specificity of PYR is 78% and 90%.[32]

Our non-invasive, MRI based deep learning algorithm outperformed these methods with a sensitivity and specificity of 96.3% and 91.6% respectively. The overall determination of MGMT promoter methylation status is based on the majority of voxels in the tumor. Given the variability in the cut-off values for pyrosequencing-based detection, we performed a Youden's statistical index analysis to determine if the optimal cut-off for our deep learning algorithm was different

than majority voting (>50%). The analysis demonstrated that maximum accuracy, sensitivity, specificity, PPV, and NPV were obtained at an optimal cut-off of 50%, the same as majority voting.

Our algorithm was trained on ground-truth obtained from the TCGA database. The TCGA uses Infinium assays to determine MGMT promoter methylation status.[102-104] Infinium assays are an immunofluorescence method that uses next generation high-throughput microchip arrays and probes. While these methods have been reported to be more sensitive and specific than the most widely available clinical assays, these methods require pre-existing probes to detect specific methylation sites.[104] The sensitivity and specificity values change depending on the probe and analytical model used to interpret the results.[104] The sensitivities for the best probes range from 87.5-90.6% while the specificity is 94.4%.[104] The overall accuracy of these probes with an optimized analytical model ranges from 91.24%-93.6%.[34] The accuracy of the commercially available Infinium assay with the best analytical model is 92%.[34] Our algorithm outperforms this assay with a mean cross-validation testing accuracy of 94.73%. While the algorithm appears to outperform the ground truth, there are additional factors that need to be considered for this dataset. The TCGA database used very stringent tissue screening prior to molecular testing, including review of tissue to ensure a minimum of 80% tumor nuclei and a maximum of 50% necrosis with additional quality control measurements of the extracted DNA and RNA prior to analyses. Additionally, the MGMT determinations made in the TCGA database were verified by a secondary test.[48] Thus, the reported Infinium assay accuracy is not necessarily comparable to the accuracy in the TCIA/TCGA dataset. It is also possible that the algorithm learns features that allow it to perform better than the single-site tissue-biopsy sample ground truth performance, since the algorithm "samples" the entire tumor and learns imaging features that are specific to MGMT mutation.

Tissue based methods for determining MGMT promoter methylation status remain a complex, multi-step process that is susceptible to failure and inaccuracy even after an adequate tissue sample has been obtained. As such, the ability to determine MGMT promoter methylation status based on routine T2-w images alone is highly desirable. Additionally, because our algorithm was trained and evaluated on the multi-institutional TCIA database it is a better representative of algorithm robustness, real-world performance, and potential clinical utilization than previously reported methods.[25]

The algorithm misclassified 13 cases: six subjects were misclassified as unmethylated and 7 as methylated. Despite these misclassifications, our network achieved a mean cross-validation testing accuracy of 94.73% which is higher than for the MSP, PYT, and Infinium assays.[104] While these tissue based methods require an invasive procedure and subsequent tissue processing for at least 48 hours, our deep learning algorithm can segment the entire glioma and determine MGMT promoter methylation status in 3 minutes. The deep learning algorithm can also be fine-tuned to variations in institutional MRI scanners, while other tissue-based methods currently lack standardization as mentioned above.

The limitations of our study are that deep learning studies require large amounts of data and the relative number of subjects with MGMT promoter methylation is small in the TCGA database. While the number of subjects may seem small, it should be noted that we used a patch-based algorithm with data augmentation, which provided well over 300,000 samples (patches) for training and validation. Additionally, acquisition parameters and imaging vendor platforms vary across imaging centers that contribute data, although this may also be a regarded as a desirable aspect for the generalizability of the approach. Our current classification approach uses a largest connected component step to limit false positives. As a consequence, multifocal tumors represent

a potential limitation. Despite these caveats our algorithm demonstrated high accuracy in determining MGMT promoter methylation status approaching tissue-level performance.

5.5. Conclusion

We demonstrate high accuracy in determining MGMT promoter methylation status using only T2-w MR images. This represents an important milestone toward using MRI to predict glioma histology, prognosis, and appropriate treatment.

Acknowledgements

We thank Yin Xi, PhD, statistician for help with the ROC and AUC.

Chapter 6

To evaluate the performance of molecular profiling algorithms on motion corrupted, motion corrected and clinical T2w Magnetic Resonance Images

6.1. To evaluate the effect of motion corruption and deep learning-based motion correction on the molecular profiling algorithms (IDH, 1p/19q and MGMT).

This chapter is currently under review at the Journal of Medical Imaging - SPIE.

6.1.1. Introduction

Primary brain tumors are known to demonstrate a broad diversity in their physical appearance, MR imaging features, response to therapy, and prognosis. This heterogeneity can be associated with specific genetic and molecular profiles. For example, isocitrate dehydrogenase 1 & 2 (IDH 1/2) mutated gliomas demonstrate increased survival compared to wild-type gliomas.[105] Additionally, 1p/19q codeletion status and O6-methyl guanine-DNA methyltransferase (MGMT) promoter methylation status are generally associated with differences in response to specific types of chemoradiation.[106,107]

Molecular profiling of gliomas has now become a routine part of the evaluation of specimens obtained via brain biopsy or surgical resection. However, obtaining this information prior to surgery can aid in planning the extent of tumor resection. In some cases, for tumors in locations where resection is not possible, and the risk of a biopsy is high, accurate delineation of the molecular profile of the tumor can be used to guide empiric treatment with radiation and/or chemotherapy.

Recently, there have been advances in classifying tumor profiles using non-invasive imaging.[11,108] These classification algorithms can be designed based on linear regression models, classical machine learning, and, deep learning networks.[109-112] Deep learning-based methods have shown promise, outperforming other approaches, including classical machine learning. Using tumor maps and molecular labels as ground truth, the imaging features that help classify the tumor molecular subtype are learned by the algorithm using convolutional layers.[113,114] Our 3D-IDH network achieved 97% accuracy for classifying IDH mutation status in primary brain tumors utilizing T2w MR images alone.[11] We extended this approach with T2w images to 1p/19q and MGMT, achieving accuracies of 93% and 95%, respectively, rivaling tissue characterization.[115]

An important caveat of using MRI is the effect of degradation on the input images, such as motion artifact. Motion artifacts are an extensive source of MR image quality degradation. They can be due to gross patient movements, as well as physiologic cardiac and respiratory motion.[116,117] In clinical practice, these artifacts can interfere with diagnostic interpretation, impacting image quality in 10-42% of brain MR examinations, and necessitating repeat imaging in up to 20% of cases.[118,119] It is also not guaranteed that a patient will be able to hold motionless during repeat imaging, and often the diagnostic quality remains impaired. This can incur substantial financial costs to the health care system. The effect of motion artifacts on the performance of deep learning-based classifiers has not been studied systematically. It is likely that motion corruption will also lead to reduced performance of deep-learning algorithms in classifying brain tumor images.,

The goals of this study were: 1) to evaluate the effect of motion corruption on deep learning-based molecular marker classification accuracy in gliomas, and 2) to determine if deep learning motion correction can recover classification accuracies to levels similar to non-corrupted images. A novel deep learning-based network for motion correction was developed to remove motion

artifact from T2w brain images across a broad range of motion corruption in glioma patients. To assess the effects of motion artifact corruption on classification accuracies, our three top-performing molecular profiling algorithms were used.[11,120] These networks use only T2w images and have provided the highest MRI-based classification accuracies reported to date, approaching invasive tissue-based methods. The purpose of this study is to perform an initial investigation on the effects of induced motion artifact on deep learning-based molecular classification, and the relative importance of robust correction methods in recovering the accuracies for potential clinical applicability.

6.1.2. Materials and Methods

6.1.2.1. Data and Pre-processing

Individual subject imaging data were retrieved from the TCIA database [121], while corresponding tumor genomic information was obtained from the TCGA database. [122] Only preoperative cases with T2w images were included. The final IDH dataset consisted of 214 subjects (94 IDH-mutated and 120 IDH wild-type). Imaging and genomic data from 368 subjects with 1p/19q co-deletion status (130 1p/19q co-deleted and 238 non-co-deleted) and 247 subjects with MGMT methylation status (163 MGMT methylated and 84 unmethylated) were also obtained from the TCIA and TCGA databases. The TCGA subject IDs, molecular profile, age, and sex are provided in the Supplementary Data (Tables 1, 2, and 3).

Minimal preprocessing was applied to the imaging datasets, consisting of (1) co-registration of the T2w images to the SR124 T2w template[25] using Advanced Normalization Tools (ANTS) software[123] (2) skull stripping of the T2w images using the Brain Extraction Toolkit (FMRIB software library) [124] (3) N4 Bias Field Correction to remove radiofrequency pulse inhomogeneity,

and (4) Image intensity normalization by performing zero mean and unit variance. The preprocessing steps required less than 5 minutes per subject.

6.1.2.2. Motion Simulation

K-space data were obtained after applying a 2D inverse Fourier transformation to the T2w image. Motion artifacts were simulated by incorporating additional phase to the k-space data along the phase encoding direction according to equation 1.[125]

$$SM_{xy}(ky) = M_{xy}(\mathrm{ky}) \times e^{(-i2\pi k_y \theta(k_y))}\ ; \begin{cases} k_y = -\frac{N_y}{2}\ to\ -\frac{(N_y - N)}{2} \\ k_y = +\frac{(N_y - N)}{2}\ to\ +\frac{N_y}{2} \end{cases} \qquad (1)$$

k_y represents the k-space data along the phase encoding direction, $M_{xy}(k_y)$ is the original k-space, $SM_{xy}(k_y)$ is the motion simulated k-space, and $\theta(k_y)$ is the phase induced by motion. This approach closely simulates the additional phase induced by translational patient movements.[126] The total number of corrupted k-space lines is given by N, such that the outermost N/2 lines on either side of k-space are corrupted. The corruption rate (CR) represents the percentage of corrupted k-space (Figure 19), where CR = N/N_y with N_y being the total number of phase encoding lines (e.g., N_y = 240). In our study, the number of corrupted k-space lines (N) ranged from 10, 20, 60, 80, 100, 120, 140, 150, 160, 180, 220, and 240 which corresponded to CRs of 4%, 8%, 25%, 33%, 42%, 50%, 58%, 63%, 67%, 75%, 83%, 92%, and 100%. These CR values were selected to represent a broad range of motion artifacts, from minimal to highly corrupted images.

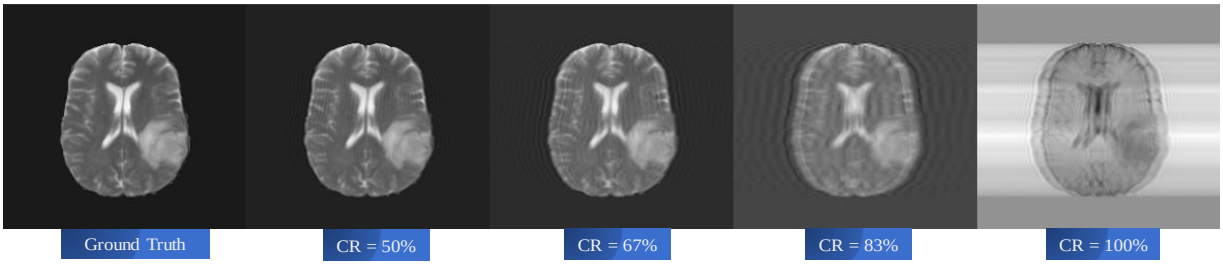

Figure 19: Example of simulated motion data.
From left to right, ground truth T2w image (column 1) and corrupted images for CR=50%, 67%, 83% and 100% (columns 2 -5)

6.1.2.3. Network Architecture

The motion correction algorithm is adapted from a 2D Dense-Unet architecture (Figure 20).[127] It consists of 4 transition down blocks, 4 transition up blocks with an initial and a final convolution layer. Each transition down block consists of a dense block and a pooling block, while each transition up block consists of an up-sampling block and dense block. Each dense block has 5 densely connected convolutional layers [128], where each layer is connected to every other layer in the dense block. The feature maps of all the convolutional layers in the dense block were concatenated to the output of the block, providing a dense connection. The output of the dense block was also concatenated with the input.

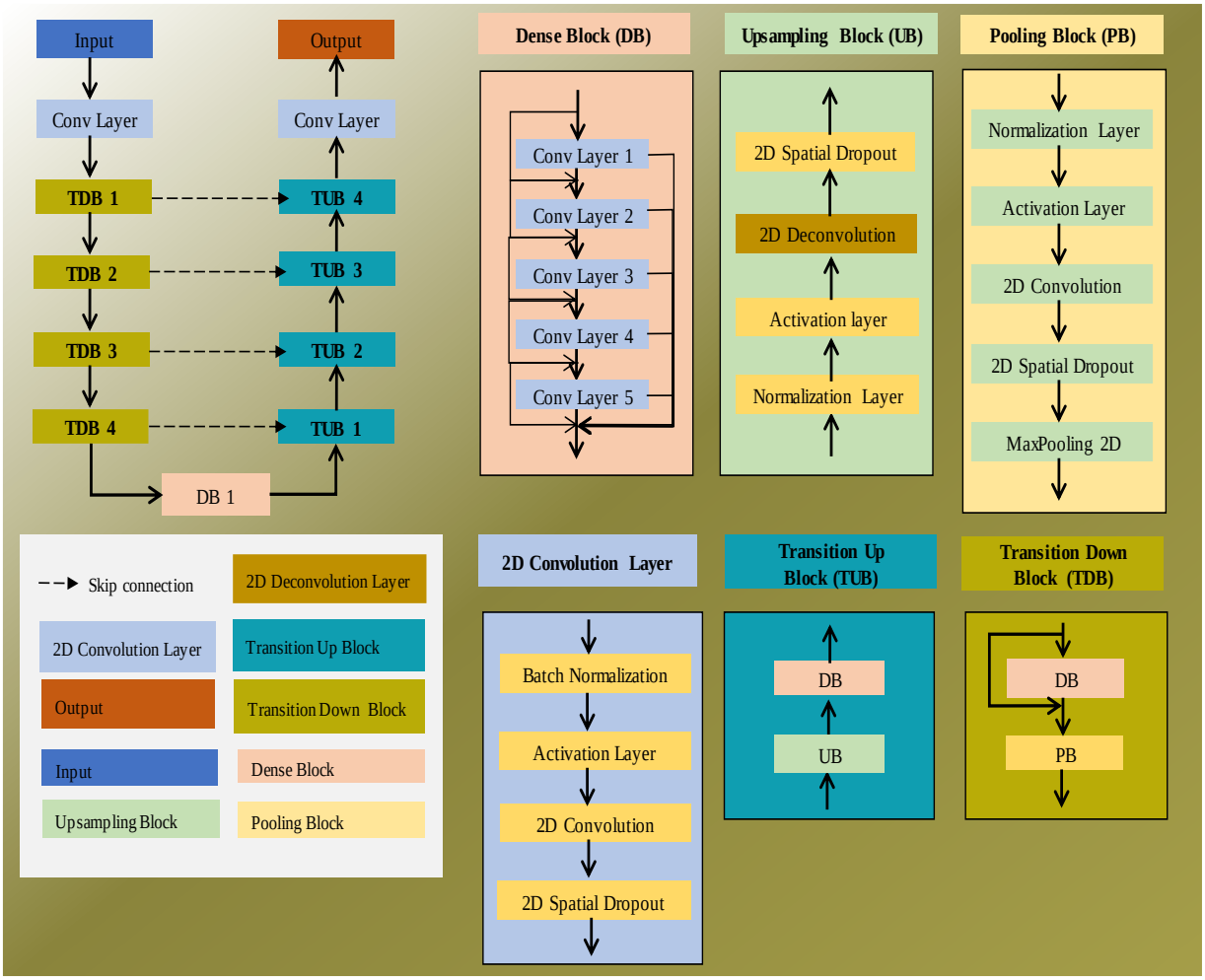

Figure 20: Network Architecture of the Motion correction algorithm.

6.1.2.4. Training

The network was trained using a combined dataset of 446 unique subjects from all three molecular marker groups (IDH, 1p/19q, and MGMT). This combined dataset was randomly shuffled into three groups to perform a 3-fold cross-validation. For each of the three folds, the groups were alternated between training, in-training validation, and held-out testing sets (~149 subjects per set). The 2D slices were separated by subject for each of the cross-validation folds to eliminate the problems of subject duplication and data leakage. [31,32]

Data augmentation was performed on the input T2w images, including horizontal and vertical flipping, to increase training quality and diversity, which helps for training models with limited data. The networks were implemented on NVIDIA Tesla V100 GPUs using Keras, a python package with Tensorflow[129] as the backend, with an adaptive moment optimizer. The initial learning rate of the optimizer was set at $1x10^{-5}$.

6.1.2.5. Testing

The performance of the models was evaluated using SSIM, PSNR, and normalized mean squared error (NMSE). The motion correction network retrained on the combined dataset was evaluated on the held-out testing set for each of the three cross-validation folds. The results from each fold were averaged across all subjects for each corruption level. The testing time for each subject was less than 60 seconds.

Molecular classification accuracies for IDH, 1p/19q, and MGMT promoter were then evaluated using the retrained best-performing motion correction network. Accuracies were determined using the ground truth uncorrupted images and at each of the image corruption levels (from 4% to 100% CR) for each cross-validation fold using our previously trained deep learning

molecular classification networks.[11] The results were averaged across folds to provide a mean classification accuracy for each molecular marker at each corruption level. This process was then repeated on the motion-corrected images for IDH, 1p/19q, and MGMT at each corruption level to determine if the ground truth accuracies could be recovered. Note that the cross-validation folds for the motion correction training network were designed to exclude the subjects in the molecular marker testing folds to avoid bias in determining accuracy recovery.

6.1.3. Results

6.1.3.1. Motion Correction

Table 7 shows the SSIM, PSNR, and NMSE metrics for the motion correction algorithm. Figure 21 shows the motion-corrected output images generated by the three networks for a single subject at high levels of motion corruption (corruption rate[104] = 83% and 100%).

Table 7: Motion correction algorithm performance averaged across 3-fold cross-validation

Model	**SSIM**	**PSNR**	**NMSE**	**SSIM**	**PSNR**	**NMSE**	**SSIM**	**PSNR**	**NMSE**
	Output for CR = 100%			*Output for CR = 92 %*			*Output for CR = 83 %*		
Motion correction algorithm	99.47	44.39	0.01	99.72	49.62	0.00	99.76	50.95	0.00

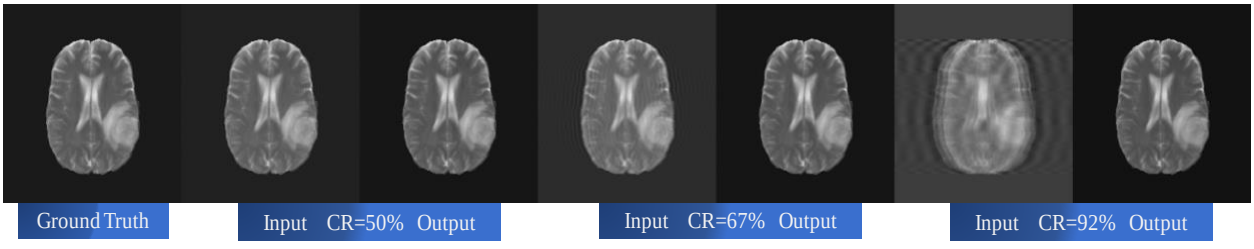

Figure 21: Example motion correction performance for a single subject.
From left to right, ground truth image (column 1), 50% CR input and corrected output (columns 2 and 3), 67% CR input and output (columns 4 and 5), 92% CR input and output (columns 6 and 7).

6.1.3.2. Classification of molecular markers.

The motion correction network was trained and tested on a larger combined dataset. The performance of all the molecular profiling algorithms (IDH, 1p/19q co-deletion, & MGMT) were evaluated on both the motion corrupted and motion corrected images.

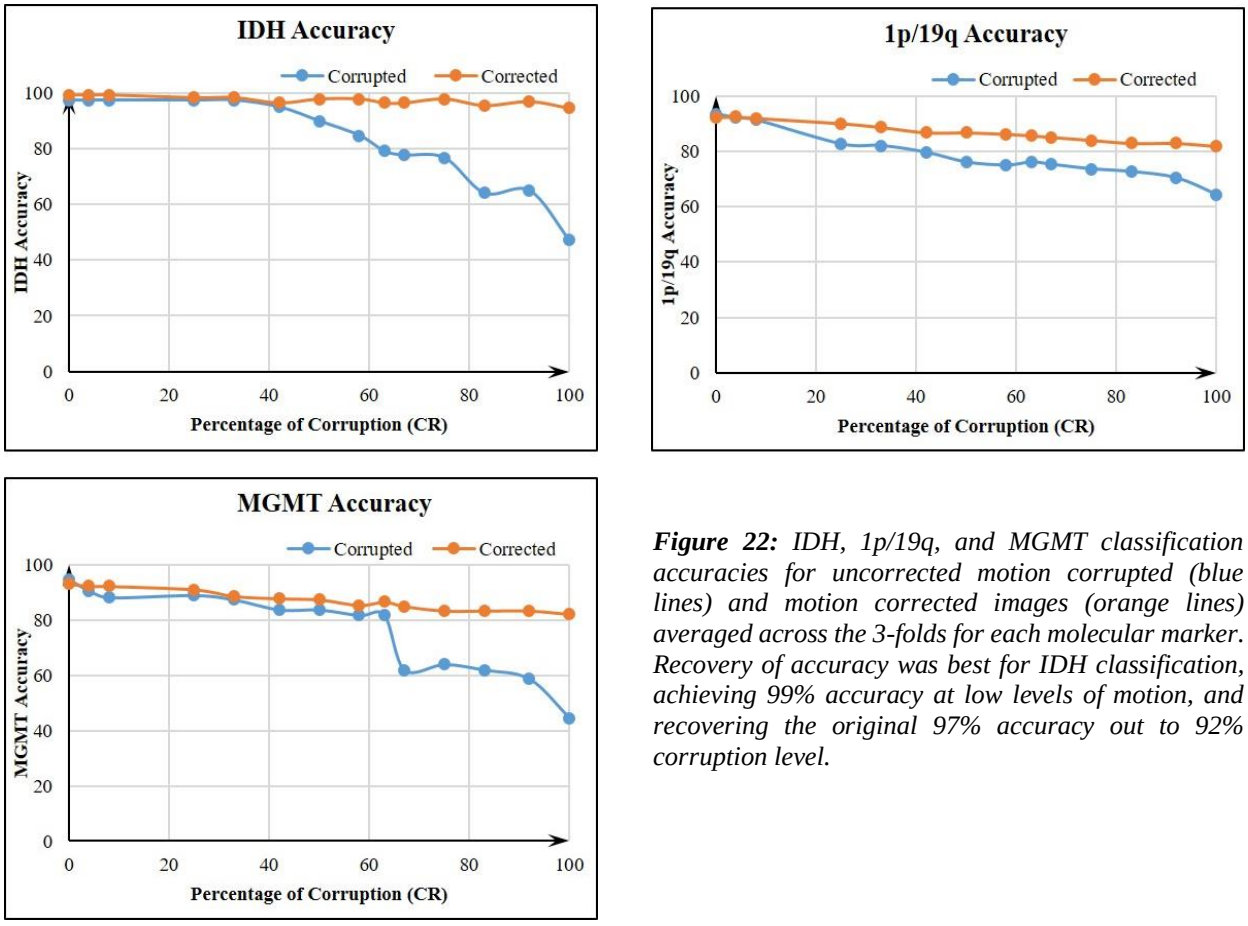

Figure 22: *IDH, 1p/19q, and MGMT classification accuracies for uncorrected motion corrupted (blue lines) and motion corrected images (orange lines) averaged across the 3-folds for each molecular marker. Recovery of accuracy was best for IDH classification, achieving 99% accuracy at low levels of motion, and recovering the original 97% accuracy out to 92% corruption level.*

Figure 22 depicts the IDH, 1p/19q co-deletion, and MGMT methylation status classification performance on the motion corrupted images, and recovery of accuracy using the motion corrected network after it was trained on the larger combined dataset. The classification accuracy on the corrupted images declined at 42% CR for both IDH and 1p/19q, while MGMT performance declined at 63% CR. For the corrected images, IDH classification was maintained at 97% accuracy out to 92% CR, and recovered to 94% accuracy even at 100% CR. More remarkably, for correction

of the native images and at lower levels of image corruption (0%-33%), IDH classification accuracy exceeded the performance of the uncorrupted images achieving up to 99% accuracy. For both 1p/19q and MGMT, 82% accuracy was recovered out to 100% CR.

In the case of IDH, we also investigated the change in voxel-wise Dice scores (Figure 23). The motion-corrected images demonstrated improved voxel-wise Dice scores across motion levels compared to the uncorrupted images. For the uncorrupted images, voxel-wise Dice scores were 0.86 and 0.87 for mutated and wild-type, respectively. Following correction, the IDH mutated Dice score increased to 0.88 at up to 25% corruption. Both IDH wild-type and IDH mutated dice scores were increased relative to the uncorrupted images even at 100% image corruption. Figure 23 shows the voxel-wise Dice scores across different corruption levels for IDH mutated, IDH wild-type, and for the whole tumor segmentation (IDH mutated + IDH wild-type).

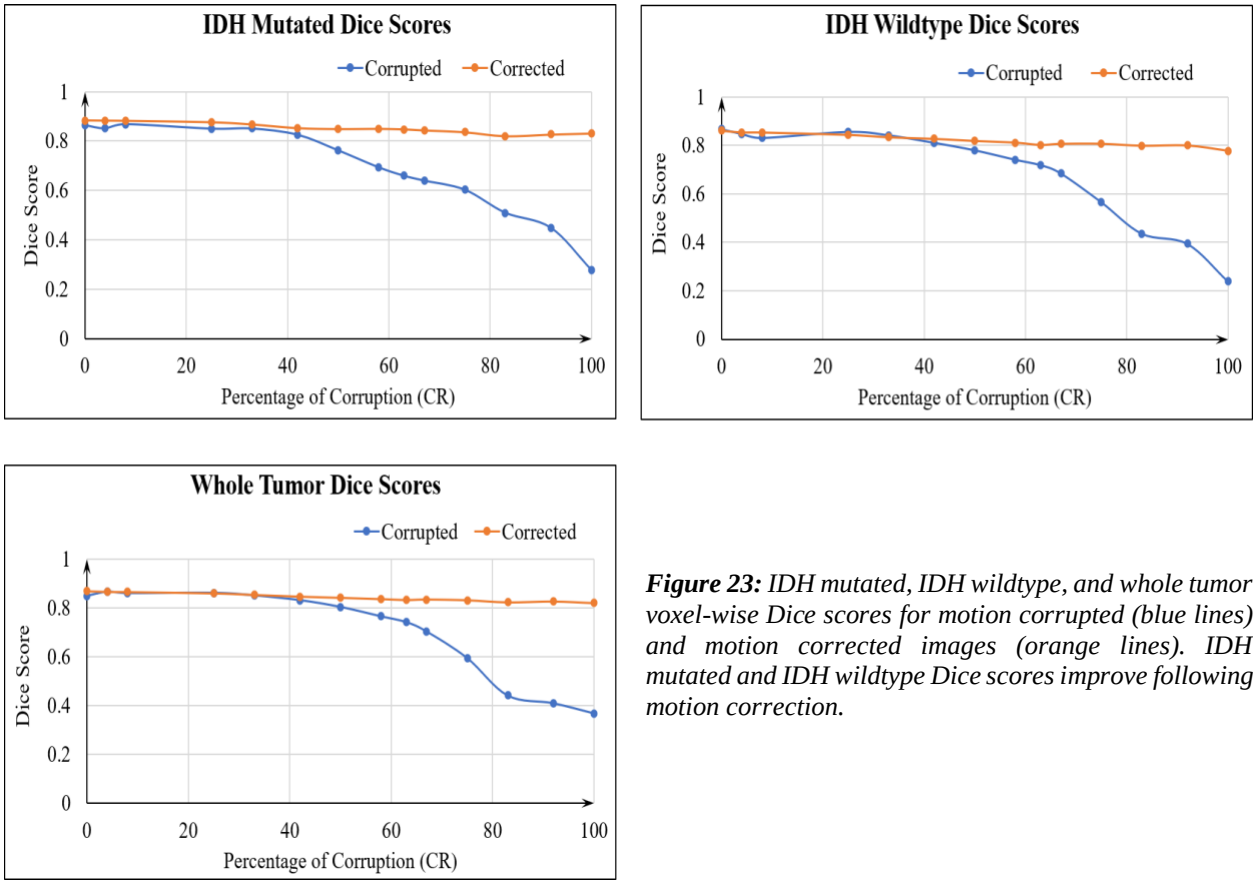

Figure 23: *IDH mutated, IDH wildtype, and whole tumor voxel-wise Dice scores for motion corrupted (blue lines) and motion corrected images (orange lines). IDH mutated and IDH wildtype Dice scores improve following motion correction.*

6.1.3.3. ROC analysis

The ROC curves for IDH mutation status, 1p/19q co-deletion status and MGMT promoter status on ground truth images are provided in Figure 24. After motion correction, the T2-net yielded higher classification accuracy and improved ROC curve. However, the performance of 1p/19q-net before and after motion correction was similar. Although the classification accuracy of MGMT-net could not be fully recovered after motion correction, the network demonstrated improved ROC performance with a higher AUC value.

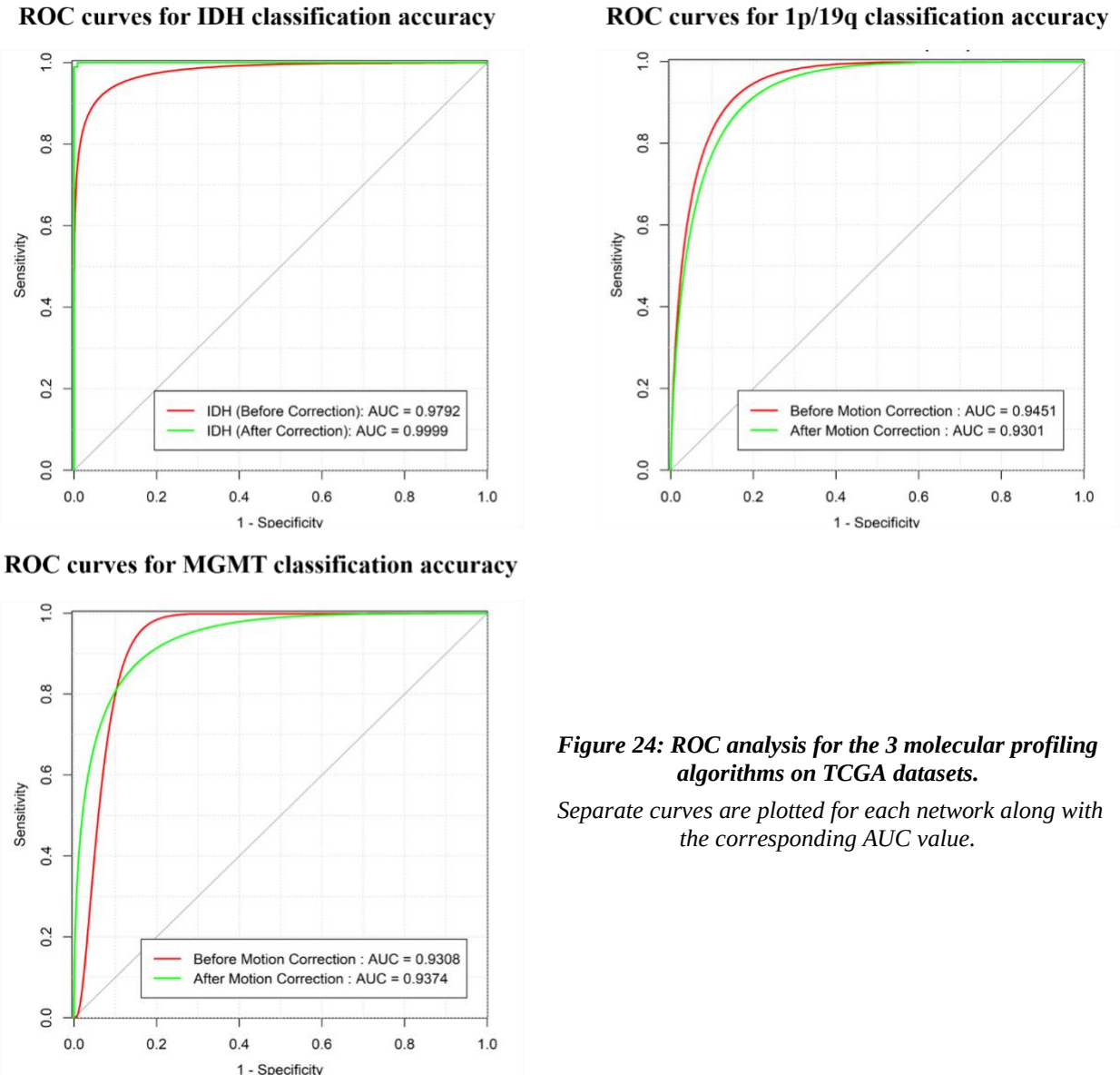

Figure 24: ROC analysis for the 3 molecular profiling algorithms on TCGA datasets.

Separate curves are plotted for each network along with the corresponding AUC value.

6.1.4. Discussion

The motion correction study demonstrates that the performance of the molecular profiling algorithms (IDH mutation, 1p/19q co-deletion, and MGMT methylation) were adversely affected by motion corruption. Although it was expected that the molecular classification accuracy would be degraded due motion corruption, the molecular profiling algorithms were resilient to motion corruption and retained their original accuracies up to & beyond 40% corruption levels. However, the algorithms demonstrated progressive loss in accuracy with increasing motion corruption. Although the networks never saw any motion corrected imaging or tumor features during its training, the classification accuracies could still be recovered or significantly improved after applying a deep learning-based motion correction, even at very high levels of motion corruption. In the case of IDH classification, an accuracy of 99% was achieved following motion correction, exceeding the performance of IDH algorithms on native ground truth images.[11]

The TCIA dataset used to train the networks (i) represents one of the largest publicly available brain tumor databases, (ii) surpasses the size of the training datasets used in any other molecular profiling and/or motion correction studies, (iii) has a variety of gliomas with different biological behaviors, and (iv) has multi-institutional representation using different MRI vendor platforms with a variety of image acquisition parameters. Additionally, in contrast to prior motion correction studies which used a fixed or limited sets of motion corruption levels (Duffy et al.[130] limited corruption to 30 lines of k-space), our motion correction network was trained using a broad range of motion corruption levels, from minimal (4%) to severely distorted (100% of k-space lines affected). This approach better captures real-world conditions where there is a mixture of motion artifacts, from mild motion that largely preserves diagnostic information to more severe cases that are effectively uninterpretable. Furthermore, the molecular profiling algorithms were trained on

the TCIA datasets which included both relatively motion/artifact free images (~90% of the data), and images with visible level of the motion/artifact (~10% of the data). All these factors together account for the robustness of the molecular profiling algorithms in retaining the classification accuracy up to a corruption level of CR=42% and the improved performance of IDH algorithm on motion corrected ground truth images.

The IDH algorithm had misclassified 6 cases before motion correction. An important observation in the IDH motion correction study was that none of the images with visible motion/artifact were misclassified before motion correction, and all the 6 misclassified cases had no visible motion/artifact. After motion correction, all the 6 misclassified cases were correctly classified. However, the IDH network misclassified 2 new cases out of which 1 case belonged to the group of images with visible level of motion/artifact. Reduction in the number of misclassified cases after motion correction is a serendipitous observation that the motion correction network boosted the IDH classification accuracy to an astounding 99%, representing a new benchmark for IDH classification. This also suggests that the presence of latent image artifacts within some of the ground truth images may have obscured important image features for classification of IDH status, which were then removed by the motion correction algorithm. There was also an improvement in IDH mutant voxel-wise Dice scores following motion-correction compared to the uncorrupted native images, providing increased confidence for the subject-wise classification. This also points to a potential new strategy for boosting deep learning classifier performance using motion or artifact correction networks, even where there is no visible motion.

While deep-learning motion correction can be regarded as a preprocessing step in the classification pipeline, an alternative approach would be to intentionally train the molecular classifier networks using corrupted imaging data. A potential caveat for such a strategy is that it

could lead to the networks erroneously learning incorrect imaging features (in the form of motion corrupted imaging features or the motion artifacts themselves) as the basis for classifying the molecular markers. As such, deep learning image-based classification studies have excluded data with significant artifacts from their training database.[108,131,132] Alternatively, conventional non-machine-learning based motion correction strategies could be utilized before applying the molecular classification algorithms. However, a key advantage to our deep learning approach is that it may be applied retrospectively to any previously acquired image without the need for any additional acquisition time, special scanner preparatory steps, or additional input data.

The TCIA dataset has a variety of gliomas with different biological behaviors, including glioblastoma, anaplastic astrocytoma, low-grade glioma, and oligodendroglioma, with their associated variations in IDH mutation, 1p/19q co-deletion, and MGMT methylation status. Importantly, the motion correction network was able to not only remove the motion artifacts but also preserve the key MR imaging features of the tumors necessary for accurate classification. This was evidenced by the full recovery of classification accuracy for the IDH network extending out to a corruption level of 92%, and markedly improved accuracies for 1p/19q co-deletion and MGMT methylation networks following the application of the motion correction algorithm. These compelling results support the routine use of a deep learning-based image artifact removal step for imaging-based deep learning applications to classify glioma molecular profiles. We demonstrated that this implementation enhances the robustness of the classification pipeline to real-world challenges, which facilitates its potential clinical feasibility and implementation.

6.1.5. Conclusion

The effect of simulated translational motion artifacts on glioma molecular classification networks and the ability of rudimentary motion correction networks to recover classification

accuracy was evaluated. This work demonstrates that high-performing classification networks for IDH mutation status, 1p/19q co-deletion, and MGMT methylation progressively lose accuracy with increasing motion-related image degradation. However, by incorporating motion correction prior to the classification step, recovery of classification network accuracy was possible even at the highest degrees of motion disruption, indicating that not only was the network successful at removing artifacts but also in recovering crucial imaging features of the tumors. After training the motion correction network on a larger dataset composed of all three glioma markers, an accuracy of 99% was achieved for IDH classification, representing a new benchmark in non-invasive image based IDH classification performance. More remarkably, classification accuracy was boosted even in the absence of added simulated motion in the native images. This provides a potential new strategy for boosting deep learning classifier performance by including the use of motion or artifact correction networks, even where there is no visible motion.

6.2. Clinical translation of the molecular profiling algorithms.

6.2.1. Background and Purpose

Automated brain tumor segmentation and classification algorithms generally perform well only on specific datasets.[133] Clinical translation of such automated algorithms has the potential to improve speed and response to therapy, reducing interobserver variability, and improving treatment planning.[133] Although these automated algorithms perform very well on specific training sets, their generalization to clinical datasets have been poor, preventing easy clinical translation.[133] The purpose of this study was to evaluate the performance of our molecular profiling algorithms (IDH, 1p/19q and MGMT) on clinically acquired MR images.

6.2.2. Material and Methods

6.2.2.1. Data and Pre-processing

The UT southwestern glioma database consists of approximately 500 clinical MRI studies acquired between 2008-2018. Most of the MR images were acquired with anisotropic voxels, typically used in routine clinical 2D images, characterized by high in-plane resolution (0.6 – 1.0 mm) and low through-plane resolution (slice thickness varying between 3-5 mm).

Ground truth molecular status was obtained from the UT Southwestern electronic health records. The final datasets included 234 cases (77 IDH mutant & 167 IDH wild-type) with multi-contrast MRI, 283 T2w MR images (93 IDH mutant & 190 IDH wild-type), 79 T2w MR images (40 1p/19q co-deleted & 39 1p/19q non co-deleted), and 57 T2w MR images (16 MGMT methylated & 41 MGMT unmethylated). Data preprocessing included (a) ANTs affine co-registration[28] to the SRI24 template[71], (b) skull stripping using the Brain Extraction Tool (BET)[72] from FSL[72-75], (c) removal of RF inhomogeneity using N4BiasCorrection[29], and (d) normalizing

signal intensity to zero-mean and unit variance. The pre-processing took approximately 5 minutes per dataset.

6.2.2.2. Testing and segmentation times

Molecular classification accuracies for IDH, 1p/19q, and MGMT promoter status were evaluated using the pre-trained networks on the TCGA data. The clinical data were then provided to the pre-trained motion correction algorithm from section 6.1 and molecular classification accuracies were re-evaluated. The trained networks took approximately seven minutes to pre-process the data, segment the whole tumor, implement DVF and profile the molecular markers for each subject.

Each molecular profiling algorithm yields two segmentation volumes. A majority voting over the voxel-wise classes of the two volumes provided a single molecular marker status for each subject. The dual-volume fusion (DVF) approach was used to combine the 2 segmentation volumes, and the largest connected component was obtained using the 3D connected component algorithm in MATLAB[I]. The combined volumes provided a single tumor segmentation map.

6.2.2.3. Statistical Analysis

Statistical analysis was performed in R for all the algorithms. The accuracy of the networks was evaluated with majority voting (*i.e.* voxel-wise cutoff of 50%). This threshold was then used to calculate the accuracy, sensitivity, and specificity of the algorithms. A Receiver Operating Characteristic (ROC) curve was also calculated separately for each network.

6.2.3. Results

6.2.3.1. Classification of IDH mutation status

6.2.3.1.1. Multi-contrast TS-net

The multi-contrast TS-net achieved a testing accuracy of 90.17%. The sensitivity, specificity, PPV, NPV and AUC for TS-net was 0.86, 0.92, 0.85, 0.93 and 0.90, respectively.

6.2.3.1.2. T2-net : Before Motion correction

Before motion correction, the T2-net achieved a testing accuracy of 91.52%. The sensitivity, specificity, PPV, NPV and AUC for T2-net was 0.84, 0.95, 0.90, 0.92 and 0.91, respectively.

6.2.3.1.3. T2-net : After Motion correction

After motion correction, the T2-net achieved a testing accuracy of 92.23%. The sensitivity, specificity, PPV, NPV and AUC for T2-net was 0.90, 0.93, 0.86, 0.95 and 0.90, respectively.

Table 8 : IDH classification accuracies for multi-contrast TS-net, T2-net before motion correction and T2-net after motion correction

Network type	Accuracy	Sensitivity	Specificity	PPV	NPV	AUC
Multi-contrast TS-net	90.17%	0.86	0.92	0.85	0.93	0.90
T2-net (Before motion correction)	91.52%	0.84	0.95	0.90	0.92	0.91
T2-net (After motion correction)	92.23%	0.90	0.93	0.86	0.95	0.90

6.2.3.2. Classification of 1p/19q co-deletion status

6.2.3.2.1. 1p/19q-net: Before motion correction

1p/19q-net achieved a testing accuracy of 89.87%. The sensitivity, specificity, PPV, NPV and AUC for TS-net was 0.82, 0.97, 0.97, 0.84 and 0.86, respectively.

6.2.3.2.2. 1p/19q-net: After motion correction

After motion correction, 1p/19q-net achieved a testing accuracy of 91.14%. The sensitivity, specificity, PPV, NPV and AUC for TS-net was 0.93, 0.90, 0.90, 0.92 and 0.90, respectively.

Table 9: 1p/19q classification accuracies before and after motion correction

Network type	Accuracy	Sensitivity	Specificity	PPV	NPV	AUC
1p/19q-net (Before motion correction)	89.87%	0.82	0.97	0.97	0.84	0.86
1p/19q-net (After motion correction)	91.14%	0.93	0.90	0.90	0.92	0.90

6.2.3.3. Classification of MGMT promoter status

6.2.3.3.1. MGMT-net: Before motion correction

MGMT-net achieved a testing accuracy of 89.74%. The sensitivity, specificity, PPV, NPV and AUC for TS-net was 0.81, 0.92, 0.81, 0.93 and 0.82, respectively.

6.2.3.3.2. MGMT-net: Before motion correction

After motion-correction MGMT-net achieved a testing accuracy of 89.74%. The sensitivity, specificity, PPV, NPV and AUC for TS-net was 0.81, 0.92, 0.81, 0.93 and 0.82, respectively.

Table 10: MGMT classification accuracies before and after motion correction

Network type	Accuracy	Sensitivity	Specificity	PPV	NPV	AUC
MGMT-net (Before motion correction)	89.47 %	0.81	0.93	0.91	0.93	0.82
MGMT-net (After motion correction)	89.47%	0.88	0.90	0.78	0.95	0.82

6.2.3.4. ROC analysis

The ROC curves for the 3 classification networks and the clinical data are provided in Figure 25.

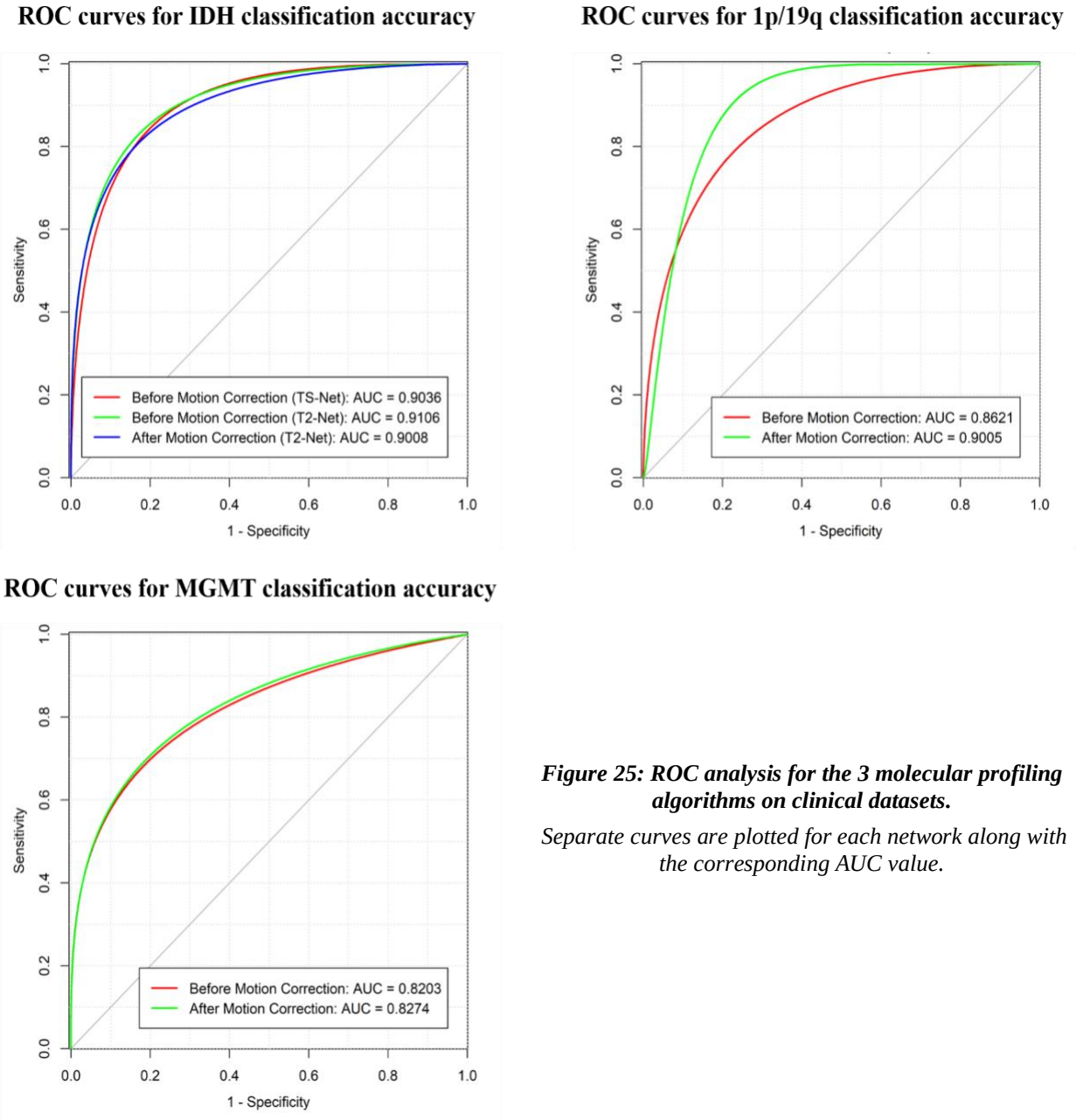

Figure 25: ROC analysis for the 3 molecular profiling algorithms on clinical datasets.

Separate curves are plotted for each network along with the corresponding AUC value.

6.2.4 Discussion

The IDH classification algorithms achieved classification accuracies of 90.17% (TS-net) and 91.52% (T2-net) on the clinical data. The 1p/19q-net and MGMT-net achieved classification accuracies of 89.87% and 89.47% respectively before motion correction. After motion correction, the classification accuracies of T2-net (IDH) and 1p/19q-net improved to 92.23% and 91.14%. However, the performance of MGMT-net before and after motion correction remained the same.

Although the IDH T2-net after motion correction yielded higher classification accuracy, the ROC curves remained similar both before and after motion correction and compared to TS-net. TS-net was not evaluated after motion correction as we did not train a multi-contrast motion algorithm. The 1p/19q-net after motion correction demonstrated improved classification accuracy, a better ROC curve and higher AUC. Although the classification accuracy of MGMT-net remained constant for before & after motion correction, the after-motion correction demonstrated an improved ROC curve with a higher AUC.

For IDH and 1p/19q classification, the motion correction step improved the performance of T2-net & 1p/19q-net on the clinical data. The network trained on the TCIA database (for both classification and motion correction) provided high accuracy with the clinical data. This further supports the idea that latent image artifacts within the native images can obscure important image features required for molecular profiling, which can be removed by a motion correction algorithm. The implementation of these algorithms is retrospective in nature and therefore does not require novel any change in MR acquisition. These approaches represent significant advancements which may ultimately improve clinical workflow and patient care while reducing overall costs.

6.2.5 Conclusion

This study demonstrates that by incorporating a motion correction algorithm prior to the classification step, it is possible to improve the molecular classification accuracy in gliomas. The motion correction can be retrospectively applied and does not require additional scan time or change in image acquisition, which further facilitates potential clinical implementation.

Chapter 7

Limitations and Future work

Deep learning studies typically require a very large amount of data to achieve good performance. The number of subjects with MR images and ground truth molecular marker statuses available from the TCIA is relatively small compared to the sample-sizes typically required for deep learning. Despite this caveat, the TCIA data are representative of real-world clinical experience, with multi-parametric MR images from multiple institutions and is one of the largest publicly available brain tumor databases. Additionally, the acquisition parameters and imaging vendor platforms are diverse across the imaging centers contributing data to the TCIA dataset. This may is a desirable aspect for the generalizability of the approach. Our current classification approach uses a largest connected component step to limit false positives. As a consequence, multifocal tumors represent a potential limitation. Despite these caveats our algorithms demonstrated high classification accuracy in profiling the molecular markers approaching tissue-level performance.

Although the results show promise for clinical translation, performance of these algorithms will need to be further evaluated on larger clinical datasets. This study provides a framework for training, evaluating, and benchmarking any new artifact-correction architectures for potential insertion into a workflow. However, before using this approach in an actual clinical environment, it will be essential to train and validate the algorithms using additional independent datasets. It is important to note that the motion correction study was an initial evaluation and not meant to be an exhaustive study of artifacts and artifact correction networks on molecular classifier performance. For this initial proof-of-principle, the focus was on the effect of translational motion artifacts in MR images on deep learning molecular classification, although it is recognized that other artifacts such as rotational motion artifacts, magnetic field inhomogeneity, Gaussian noise, and

radiofrequency spikes can also affect MR image quality. Similarly, the motion correction networks were only trained to recover translational motion for this proof-of-principle. Adapting this approach to address these artifacts would not require significant modifications, and many of these can be simulated retrospectively on previously acquired imaging data for training.

Although the IDH molecular profiling algorithm performed better using motion-corrected images compared to motion-corrupted images, the classification accuracies of the 1p/19q and MGMT algorithms could not be restored fully. These findings indicate that the three classification algorithms differed in terms of their resilience to motion artifact. Both the 1p/19q and MGMT networks were based on the trained IDH network architecture, with fine-tuning to the decoder part of the network to adjust classification weightings without changes to the encoder part. This led to faster training and resultant excellent classification accuracies using uncorrupted images but, appears to have also rendered the networks less robust to image corruption compared to the fully trained IDH network. While the motion correction network achieved superior results compared to previous studies, subtle residual artifacts within the image appear to have been sufficient to affect the molecular classification performance. It is possible that performance could be enhanced with modifications to the motion correction network architecture. A 2D network design was chosen due to the associated lower computational resource demands, as well as the fact that the TCIA database contained 2D T2w images. However, recent advances in deep learning network using 3D architectures, could be adapted in the future.

The molecular profiling algorithms were trained on skull-stripped and pre-processed data in template space (SRI24). The motion simulated data, the ground truth data for training and testing the motion corruption network was also in template space. However, in a real-world scenario, a motion corrupted MR image in native space may fail the pre-processing steps itself before it gets

to the point of either skull stripping, motion correction or molecular profiling. Furthermore, the pre-processing steps of co-registration to template space introduces changes to the raw data. To address these issues, a multi-dimensional input 2D/3D segmentation and motion correction algorithm can be developed. Such a network would deal with the raw native T2w images, with skull, which essentially gives the network raw information to train on.

REFERENCES

1. Yogananda CGB, Shah BR, Vejdani-Jahromi M, et al. A Fully automated deep learning network for brain tumor segmentation. *Tomography*. 2020; 6(2):186.

2. Yogananda CGB, Wagner B, Nalawade SS, et al. Fully Automated Brain Tumor Segmentation and Survival Prediction of Gliomas using Deep Learning and MRI. Paper presented at: International MICCAI Brainlesion Workshop2019.

3. Menze BH, Jakab A, Bauer S, et al. The Multimodal Brain Tumor Image Segmentation Benchmark (BRATS). *IEEE Trans Med Imaging*. 2015; 34(10):1993-2024.

4. V S, Pankajakshan, Vinod A deep learning architecture for brain tumor segmentation in MRI images. *2017 IEEE 19th International Workshop on Multimedia Signal Processing (MMSP), Luton, 2017*. 2017:1-6.

5. Pei L, Reza SMS, Li W, Davatzikos C, Iftekharuddin KM. Improved brain tumor segmentation by utilizing tumor growth model in longitudinal brain MRI. *Proc SPIE Int Soc Opt Eng*. 2017; 10134.

6. K. Kamnitsas WB, E. Ferrante, S. McDonagh, M. Sinclair, N. Pawlowski, M. Rajchl, M. Lee, B. Kainz, D. Rueckert, B. Glocker. Ensembles of Multiple Models and Architectures for Robust Brain Tumour Segmentation. *BrainLes 2017, LNCS 10670, pp. 450–462, 2018. https://doi.org/10.1007/978-3-319-75238-9_38*. 2018.

7. Bakas S, Akbari H, Sotiras A, et al. Advancing The Cancer Genome Atlas glioma MRI collections with expert segmentation labels and radiomic features. *Sci Data*. 2017; 4:170117.

8. Yogananda CGB, Shah, Bhavya R., Yu, Frank F., et al. A novel fully automated MRI-based deep learning method for classification of 1p/19q co-deletion status in brain gliomas. *Neuro-Oncology Advances (in press)*. 2020.

9. Louis DN, Perry A, Reifenberger G, et al. The 2016 World Health Organization classification of tumors of the central nervous system: a summary. *Acta neuropathologica*. 2016; 131(6):803-820.

10. Brito C, Azevedo A, Esteves S, et al. Clinical insights gained by refining the 2016 WHO classification of diffuse gliomas with: EGFR amplification, TERT mutations, PTEN deletion and MGMT methylation. *BMC Cancer*. 2019; 19(1):968.

11. Bangalore Yogananda CG, Shah BR, Vejdani-Jahromi M, et al. A novel fully automated MRI-based deep-learning method for classification of IDH mutation status in brain gliomas. *Neuro-oncology*. 2020; 22(3):402-411.

12. Soeda A, Hara A, Kunisada T, Yoshimura S-i, Iwama T, Park DMJSr. The evidence of glioblastoma heterogeneity. 2015; 5:7979.

13. Shboul ZA, Vidyaratne L, Alam M, Iftekharuddin KM. Glioblastoma and survival prediction. Paper presented at: International MICCAI Brainlesion Workshop2017.

14. Wang GL, Wenqi & Ourselin, Sebastien & Vercauteren, Tom. Automatic Brain Tumor Segmentation using Cascaded Anisotropic Convolutional Neural Networks. *MICCAI Brats Challenge 2017*. 2017.

15. Funke J, Martel JN, Gerhard S, et al. Candidate sampling for neuron reconstruction from anisotropic electron microscopy volumes. *Med Image Comput Comput Assist Interv*. 2014; 17(Pt 1):17-24.

16. Pereira S, Pinto A, Alves V, Silva CA. Brain Tumor Segmentation Using Convolutional Neural Networks in MRI Images. *IEEE Transactions on Medical Imaging*. 2016; 35(5):1240-1251.

17. Kamnitsas K, Ledig C, Newcombe VFJ, et al. Efficient multi-scale 3D CNN with fully connected CRF for accurate brain lesion segmentation. *Medical Image Analysis*. 2017; 36:61-78.

18. Dvorak P MB. Structured prediction with convolutional neural networks for multimodal brain tumor segmentation. *In: Menze BH, Reyes M, Farahani K, Kalpathy-Cramer J, Kown D, eds. Proceedings of the Multimodal Brain Tumor Segmentation Challenge (MICCAI-BRATS). Munich, Germany: Springer, 2015:13–24* 2015.

19. Havaei M, Davy A, Warde-Farley D, et al. Brain tumor segmentation with Deep Neural Networks. *Medical Image Analysis.* 2017; 35:18-31.

20. Zhuge Y, Krauze AV, Ning H, et al. Brain tumor segmentation using holistically nested neural networks in MRI images. *Medical physics.* 2017; 44(10):5234-5243.

21. Zikic D, Ioannou Y, Brown M, Criminisi A. *Segmentation of Brain Tumor Tissues with Convolutional Neural Networks*2014.

22. Menze BH, Jakab A, Bauer S, et al. The Multimodal Brain Tumor Image Segmentation Benchmark (BRATS). *IEEE transactions on medical imaging.* 2015; 34(10):1993-2024.

23. Bakas S, Akbari H, Sotiras A, et al. Advancing The Cancer Genome Atlas glioma MRI collections with expert segmentation labels and radiomic features. *Scientific data.* 2017; 4:170117-170117.

24. Taha AA, Hanbury A. Metrics for evaluating 3D medical image segmentation: analysis, selection, and tool. *BMC Med Imaging.* 2015; 15:29.

25. Rohlfing T, Zahr NM, Sullivan EV, Pfefferbaum A. The SRI24 multichannel atlas of normal adult human brain structure. *Human brain mapping.* 2010; 31(5):798-819.

26. Emblem KE, Pinho MC, Zollner FG, et al. A generic support vector machine model for preoperative glioma survival associations. *Radiology.* 2015; 275(1):228-234.

27. Emblem KE, Due-Tonnessen P, Hald JK, et al. Machine learning in preoperative glioma MRI: survival associations by perfusion-based support vector machine outperforms traditional MRI. *J Magn Reson Imaging.* 2014; 40(1):47-54.

28. Avants BB, Tustison NJ, Song G, Cook PA, Klein A, Gee JC. A reproducible evaluation of ANTs similarity metric performance in brain image registration. *Neuroimage.* 2011; 54(3):2033-2044.

29. Tustison NJ, Cook PA, Klein A, et al. Large-scale evaluation of ANTs and FreeSurfer cortical thickness measurements. *Neuroimage.* 2014; 99:166-179.

30. Jegou S, Drozdzal, Michal., Vazquez, David., Romero, Adriana., Bengio, Yoshua. The One Hundred Layers Tiramisu: Fully Convolutional DenseNets for Semantic Segmentation. 2017.

31. Wegmayr V AS, Buhmann J, Nicholas Petrick; Kensaku Mori, Editor(s). Classification of brain MRI with big data and deep 3D convolutional neural networks. *Published in SPIE Proceedings, Medical Imaging 2018: Computer-Aided Diagnosis.* 2018; 1057501.

32. Xinyang Feng JY, Zachary C Lipton, Scott A Small, Frank A Provenzano. Deep Learning on MRI Affirms the Prominence of the Hippocampal Formation in Alzheimer's Disease Classification. *bioRxiv.* 2018; 2018:456277.

33. Abadi M, et al.,. Tensorflow: A system for large-scale machine learning. *OSDI.* 2016; pp. 265-284.

34. Charles PWD. Keras. *GitHub repository* 2013.

35. Kingma DP, Ba, J.L.,. Adam: A method for stochastic optimization. . *ICLR.* 2015.

36. Yan H, Parsons DW, Jin G, et al. IDH1 and IDH2 mutations in gliomas. *New England Journal of Medicine.* 2009; 360(8):765-773.

37. Pope WB, Prins RM, Thomas MA, et al. Non-invasive detection of 2-hydroxyglutarate and other metabolites in IDH1 mutant glioma patients using magnetic resonance spectroscopy. *Journal of neuro-oncology.* 2012; 107(1):197-205.

38. Choi C, Ganji SK, DeBerardinis RJ, et al. 2-hydroxyglutarate detection by magnetic resonance spectroscopy in IDH-mutated patients with gliomas. *Nature medicine.* 2012; 18(4):624.

39. de la Fuente MI, Young RJ, Rubel J, et al. Integration of 2-hydroxyglutarate-proton magnetic resonance spectroscopy into clinical practice for disease monitoring in isocitrate dehydrogenase-mutant glioma. *Neuro-oncology.* 2015; 18(2):283-290.

40. Tietze A, Choi C, Mickey B, et al. Noninvasive assessment of isocitrate dehydrogenase mutation status in cerebral gliomas by magnetic resonance spectroscopy in a clinical setting. *Journal of neurosurgery.* 2017; 128(2):391-398.

41. Suh CH, Kim HS, Paik W, et al. False-Positive Measurement at 2-Hydroxyglutarate MR Spectroscopy in Isocitrate Dehydrogenase Wild-Type Glioblastoma: A Multifactorial Analysis. *Radiology.* 2019; 291(3):752-762.

42. SongTao Q, Lei Y, Si G, et al. IDH mutations predict longer survival and response to temozolomide in secondary glioblastoma. *Cancer Sci.* 2012; 103(2):269-273.
43. Okita Y, Narita Y, Miyakita Y, et al. IDH1/2 mutation is a prognostic marker for survival and predicts response to chemotherapy for grade II gliomas concomitantly treated with radiation therapy. *Int J Oncol.* 2012; 41(4):1325-1336.
44. Mohrenz IV, Antonietti P, Pusch S, et al. Isocitrate dehydrogenase 1 mutant R132H sensitizes glioma cells to BCNU-induced oxidative stress and cell death. *Apoptosis.* 2013; 18(11):1416-1425.
45. Molenaar RJ, Botman D, Smits MA, et al. Radioprotection of IDH1-Mutated Cancer Cells by the IDH1-Mutant Inhibitor AGI-5198. *Cancer Res.* 2015; 75(22):4790-4802.
46. Sulkowski PL, Corso CD, Robinson ND, et al. 2-Hydroxyglutarate produced by neomorphic IDH mutations suppresses homologous recombination and induces PARP inhibitor sensitivity. *Sci Transl Med.* 2017; 9(375).
47. Beiko J, Suki D, Hess KR, et al. IDH1 mutant malignant astrocytomas are more amenable to surgical resection and have a survival benefit associated with maximal surgical resection. *Neuro Oncol.* 2014; 16(1):81-91.
48. Cancer Genome Atlas Research N. Comprehensive genomic characterization defines human glioblastoma genes and core pathways. *Nature.* 2008; 455(7216):1061-1068.
49. Zhang M, Pan Y, Qi X, et al. Identification of New Biomarkers Associated With IDH Mutation and Prognosis in Astrocytic Tumors Using NanoString nCounter Analysis System. *Appl Immunohistochem Mol Morphol.* 2018; 26(2):101-107.
50. Zhang B, Chang K, Ramkissoon S, et al. Multimodal MRI features predict isocitrate dehydrogenase genotype in high-grade gliomas. *Neuro Oncol.* 2017; 19(1):109-117.
51. Chang P, Grinband J, Weinberg BD, et al. Deep-Learning Convolutional Neural Networks Accurately Classify Genetic Mutations in Gliomas. *AJNR Am J Neuroradiol.* 2018; 39(7):1201-1207.
52. Nyberg E, Sandhu GS, Jesberger J, et al. Comparison of brain MR images at 1.5T using BLADE and rectilinear techniques for patients who move during data acquisition. *AJNR Am J Neuroradiol.* 2012; 33(1):77-82.
53. Clark K, Vendt B, Smith K, et al. The Cancer Imaging Archive (TCIA): maintaining and operating a public information repository. *J Digit Imaging.* 2013; 26(6):1045-1057.
54. Ceccarelli M, Barthel FP, Malta TM, et al. Molecular Profiling Reveals Biologically Discrete Subsets and Pathways of Progression in Diffuse Glioma. *Cell.* 2016; 164(3):550-563.
55. Cryan JB, Haidar S, Ramkissoon LA, et al. Clinical multiplexed exome sequencing distinguishes adult oligodendroglial neoplasms from astrocytic and mixed lineage gliomas. *Oncotarget.* 2014; 5(18):8083-8092.
56. Gutman DA, Dunn WD, Jr., Grossmann P, et al. Somatic mutations associated with MRI-derived volumetric features in glioblastoma. *Neuroradiology.* 2015; 57(12):1227-1237.
57. McKinley R, Meier R, Wiest R. Ensembles of Densely-Connected CNNs with Label-Uncertainty for Brain Tumor Segmentation. Paper presented at: Brainlesion: Glioma, Multiple Sclerosis, Stroke and Traumatic Brain Injuries; 2019//, 2019; Cham.
58. Delfanti RL, Piccioni DE, Handwerker J, et al. Imaging correlates for the 2016 update on WHO classification of grade II/III gliomas: implications for IDH, 1p/19q and ATRX status. *J Neurooncol.* 2017; 135(3):601-609.
59. Chang K, Bai HX, Zhou H, et al. Residual Convolutional Neural Network for the Determination of IDH Status in Low- and High-Grade Gliomas from MR Imaging. *Clin Cancer Res.* 2018; 24(5):1073-1081.
60. Pusch S, Sahm F, Meyer J, Mittelbronn M, Hartmann C, von Deimling A. Glioma IDH1 mutation patterns off the beaten track. *Neuropathol Appl Neurobiol.* 2011; 37(4):428-430.
61. Lee D, Suh YL, Kang SY, Park TI, Jeong JY, Kim SH. IDH1 mutations in oligodendroglial tumors: comparative analysis of direct sequencing, pyrosequencing, immunohistochemistry, nested PCR and PNA-mediated clamping PCR. *Brain Pathol.* 2013; 23(3):285-293.

62. Agarwal S, Sharma MC, Jha P, et al. Comparative study of IDH1 mutations in gliomas by immunohistochemistry and DNA sequencing. *Neuro Oncol.* 2013; 15(6):718-726.

63. Preusser M, Wohrer A, Stary S, Hoftberger R, Streubel B, Hainfellner JA. Value and limitations of immunohistochemistry and gene sequencing for detection of the IDH1-R132H mutation in diffuse glioma biopsy specimens. *J Neuropathol Exp Neurol.* 2011; 70(8):715-723.

64. Tanboon J, Williams EA, Louis DN. The Diagnostic Use of Immunohistochemical Surrogates for Signature Molecular Genetic Alterations in Gliomas. *Journal of Neuropathology & Experimental Neurology*. 2015; 75(1):4-18.

65. Horbinski C. What do we know about IDH1/2 mutations so far, and how do we use it? *Acta Neuropathol.* 2013; 125(5):621-636.

66. Wall JD, Tang LF, Zerbe B, et al. Estimating genotype error rates from high-coverage next-generation sequence data. *Genome Res.* 2014; 24(11):1734-1739.

67. Korfiatis P, Kline TL, Coufalova L, et al. MRI texture features as biomarkers to predict MGMT methylation status in glioblastomas. *Med Phys.* 2016; 43(6):2835-2844.

68. Polivka J, Jr., Polivka J, Repik T, Rohan V, Hes O, Topolcan O. Co-deletion of 1p/19q as Prognostic and Predictive Biomarker for Patients in West Bohemia with Anaplastic Oligodendroglioma. *Anticancer Res.* 2016; 36(1):471-476.

69. Yogananda CGB, Shah BR, Vejdani-Jahromi M, et al. A Novel Fully Automated Mri-Based Deep Learning Method for Classification of Idh Mutation Status in Brain Gliomas. *Neuro Oncol.* 2019.

70. Erickson BA, Zeynettin; Sedlar, Jiri; Korfiatis, Panagiotis. Data From LGG-1p19qDeletion. The Cancer Imaging Archive. . 2017.

71. Rohlfing T, Zahr NM, Sullivan EV, Pfefferbaum A. The SRI24 multichannel atlas of normal adult human brain structure. *Hum Brain Mapp.* 2010; 31(5):798-819.

72. Smith SM. Fast robust automated brain extraction. *Hum Brain Mapp.* 2002; 17(3):143-155.

73. Smith SM, Jenkinson M, Woolrich MW, et al. Advances in functional and structural MR image analysis and implementation as FSL. *Neuroimage.* 2004; 23 Suppl 1:S208-219.

74. Woolrich MW, Jbabdi S, Patenaude B, et al. Bayesian analysis of neuroimaging data in FSL. *Neuroimage.* 2009; 45(1 Suppl):S173-186.

75. Jenkinson M, Beckmann CF, Behrens TE, Woolrich MW, Smith SM. Fsl. *Neuroimage.* 2012; 62(2):782-790.

76. Chollet F. Keras. *https://keras.io*. 2015.

77. Jegou S, Drozdzal, Michal., Vazquez, David., Romero, Adriana., Bengio, Yoshua. The One Hundred Layers Tiramisu: Fully Convolutional DenseNets for Semantic Segmentation. *2017 IEEE Conference on Computer Vision and Pattern Recognition Workshops (CVPRW).* 2017(1175-1183).

78. Akkus Z, Ali I, Sedlar J, et al. Predicting Deletion of Chromosomal Arms 1p/19q in Low-Grade Gliomas from MR Images Using Machine Intelligence. *J Digit Imaging.* 2017; 30(4):469-476.

79. van der Voort SR, Incekara F, Wijnenga MMJ, et al. Predicting the 1p/19q Codeletion Status of Presumed Low-Grade Glioma with an Externally Validated Machine Learning Algorithm. *Clin Cancer Res.* 2019; 25(24):7455-7462.

80. Matsui Y, Maruyama T, Nitta M, et al. Prediction of lower-grade glioma molecular subtypes using deep learning. *J Neurooncol.* 2020; 146(2):321-327.

81. Wang G, Li W, Ourselin S, Vercauteren T. Automatic Brain Tumor Segmentation Based on Cascaded Convolutional Neural Networks With Uncertainty Estimation. *Front Comput Neurosci.* 2019; 13:56-56.

82. Woehrer A, Sander P, Haberler C, et al. FISH-based detection of 1p 19q codeletion in oligodendroglial tumors: procedures and protocols for neuropathological practice - a publication under the auspices of the Research Committee of the European Confederation of Neuropathological Societies (Euro-CNS). *Clin Neuropathol.* 2011; 30(2):47-55.

83. Senetta R, Verdun di Cantogno L, Chiusa L, et al. A "weighted" fluorescence in situ hybridization strengthens the favorable prognostic value of 1p/19q codeletion in pure and mixed oligodendroglial tumors. *J Neuropathol Exp Neurol.* 2013; 72(5):432-441.

84. Nikiforova MN, Hamilton RL. Molecular diagnostics of gliomas. *Arch Pathol Lab Med.* 2011; 135(5):558-568.
85. Woehrer A, Hainfellner JA. Molecular diagnostics: techniques and recommendations for 1p/19q assessment. *CNS Oncol.* 2015; 4(5):295-306.
86. Hegi ME, Diserens AC, Gorlia T, et al. MGMT gene silencing and benefit from temozolomide in glioblastoma. *N Engl J Med.* 2005; 352(10):997-1003.
87. Chen R, Smith-Cohn M, Cohen AL, Colman H. Glioma Subclassifications and Their Clinical Significance. *Neurotherapeutics.* 2017; 14(2):284-297.
88. Stupp R, Hegi ME, Mason WP, et al. Effects of radiotherapy with concomitant and adjuvant temozolomide versus radiotherapy alone on survival in glioblastoma in a randomised phase III study: 5-year analysis of the EORTC-NCIC trial. *Lancet Oncol.* 2009; 10(5):459-466.
89. Suh CH, Kim HS, Jung SC, Choi CG, Kim SJ. Clinically Relevant Imaging Features for MGMT Promoter Methylation in Multiple Glioblastoma Studies: A Systematic Review and Meta-Analysis. *AJNR Am J Neuroradiol.* 2018; 39(8):1439-1445.
90. Drabycz S, Roldan G, de Robles P, et al. An analysis of image texture, tumor location, and MGMT promoter methylation in glioblastoma using magnetic resonance imaging. *Neuroimage.* 2010; 49(2):1398-1405.
91. Moon WJ, Choi JW, Roh HG, Lim SD, Koh YC. Imaging parameters of high grade gliomas in relation to the MGMT promoter methylation status: the CT, diffusion tensor imaging, and perfusion MR imaging. *Neuroradiology.* 2012; 54(6):555-563.
92. Ahn SS, Shin NY, Chang JH, et al. Prediction of methylguanine methyltransferase promoter methylation in glioblastoma using dynamic contrast-enhanced magnetic resonance and diffusion tensor imaging. *J Neurosurg.* 2014; 121(2):367-373.
93. Kanas VG, Zacharaki EI, Thomas GA, Zinn PO, Megalooikonomou V, Colen RR. Learning MRI-based classification models for MGMT methylation status prediction in glioblastoma. *Comput Methods Programs Biomed.* 2017; 140:249-257.
94. Sasaki T, Kinoshita M, Fujita K, et al. Radiomics and MGMT promoter methylation for prognostication of newly diagnosed glioblastoma. *Sci Rep.* 2019; 9(1):14435.
95. Wei J, Yang G, Hao X, et al. A multi-sequence and habitat-based MRI radiomics signature for preoperative prediction of MGMT promoter methylation in astrocytomas with prognostic implication. *Eur Radiol.* 2019; 29(2):877-888.
96. Yogananda CGB, Shah, Bhavya R., Yu, Frank F., et al. A novel fully automated MRI-based deep learning method for classification of 1p/19q co-deletion status in brain gliomas. *Neuro-Oncology Advances (accepted pending minor revisions).* 2020.
97. Puchalski RB, Shah N, Miller J, et al. An anatomic transcriptional atlas of human glioblastoma. *Science.* 2018; 360(6389):660-663.
98. Korfiatis P, Kline TL, Lachance DH, Parney IF, Buckner JC, Erickson BJ. Residual Deep Convolutional Neural Network Predicts MGMT Methylation Status. *J Digit Imaging.* 2017; 30(5):622-628.
99. Han L, Kamdar MR. MRI to MGMT: predicting methylation status in glioblastoma patients using convolutional recurrent neural networks. *Pac Symp Biocomput.* 2018; 23:331-342.
100. Everhard S, Tost J, El Abdalaoui H, et al. Identification of regions correlating MGMT promoter methylation and gene expression in glioblastomas. *Neuro Oncol.* 2009; 11(4):348-356.
101. Cankovic M, Nikiforova MN, Snuderl M, et al. The role of MGMT testing in clinical practice: a report of the association for molecular pathology. *J Mol Diagn.* 2013; 15(5):539-555.
102. Estival A, Sanz C, Ramirez JL, et al. Pyrosequencing versus methylation-specific PCR for assessment of MGMT methylation in tumor and blood samples of glioblastoma patients. *Sci Rep.* 2019; 9(1):11125.
103. Poulin M, Zhou JY, Yan L, Shioda T. Pyrosequencing Methylation Analysis. *Methods Mol Biol.* 2018; 1856:283-296.

104. Bady P, Sciuscio D, Diserens AC, et al. MGMT methylation analysis of glioblastoma on the Infinium methylation BeadChip identifies two distinct CpG regions associated with gene silencing and outcome, yielding a prediction model for comparisons across datasets, tumor grades, and CIMP-status. *Acta Neuropathol.* 2012; 124(4):547-560.
105. Parsons DW, Jones S, Zhang X, et al. An Integrated Genomic Analysis of Human Glioblastoma Multiforme. *Science.* 2008; 321(5897):1807-1812.
106. Van Den Bent MJ, Brandes AA, Taphoorn MJB, et al. Adjuvant Procarbazine, Lomustine, and Vincristine Chemotherapy in Newly Diagnosed Anaplastic Oligodendroglioma: Long-Term Follow-Up of EORTC Brain Tumor Group Study 26951. *Journal of Clinical Oncology.* 2013; 31(3):344-350.
107. Hegi ME, Diserens A-C, Gorlia T, et al. MGMTGene Silencing and Benefit from Temozolomide in Glioblastoma. *New England Journal of Medicine.* 2005; 352(10):997-1003.
108. Nalawade S, Murugesan GK, Vejdani-Jahromi M, et al. Classification of brain tumor isocitrate dehydrogenase status using MRI and deep learning. 2019; 6(4 %J Journal of Medical Imaging):1-13, 13.
109. Zhang X, Tian Q, Wang L, et al. Radiomics strategy for molecular subtype stratification of lower-grade glioma: detecting IDH and TP53 mutations based on multimodal MRI. 2018; 48(4):916-926.
110. Korfiatis P, Kline TL, Coufalova L, et al. MRI texture features as biomarkers to predict MGMT methylation status in glioblastomas. *Medical physics.* 2016; 43(6Part1):2835-2844.
111. Meraj T, Rauf HT, Zahoor S, et al. Lung nodules detection using semantic segmentation and classification with optimal features. *Neural Computing and Applications.* 2020.
112. Villanueva-Meyer JE, Wood MD, Choi BS, et al. MRI features and IDH mutational status of grade II diffuse gliomas: impact on diagnosis and prognosis. *American Journal of Roentgenology.* 2018; 210(3):621-628.
113. Sirunyan AM, Tumasyan A, Adam W, et al. Observation of tt[over]H Production. *Phys Rev Lett.* 2018; 120(23):231801.
114. Korfiatis P, Kline TL, Lachance DH, Parney IF, Buckner JC, Erickson BJ. Residual deep convolutional neural network predicts MGMT methylation status. *Journal of digital imaging.* 2017; 30(5):622-628.
115. Yogananda CGB, Shah BR, Yu FF, et al. A novel fully automated MRI-based deep learning method for classification of 1p/19q co-deletion status in brain gliomas. *Neuro-Oncology Advances (in press).* 2020.
116. Enzmann DR, O'Donohue J, Rubin JB, Shuer L, Cogen P, Silverberg G. CSF pulsations within nonneoplastic spinal cord cysts. *American Journal of Roentgenology.* 1987; 149(1):149-157.
117. Kjos BO, Ehman RL, Brant-Zawadzki M, Kelly WM, Norman D, Newton TH. Reproducibility of relaxation times and spin density calculated from routine MR imaging sequences: clinical study of the CNS. *American Journal of Roentgenology.* 1985; 144(6):1165-1170.
118. Zaitsev M, Maclaren J, Herbst M. Motion artifacts in MRI: A complex problem with many partial solutions. *Journal of Magnetic Resonance Imaging.* 2015; 42(4):887-901.
119. Maclaren J, Herbst M, Speck O, Zaitsev M. Prospective motion correction in brain imaging: a review. *Magnetic resonance in medicine.* 2013; 69(3):621-636.
120. Yogananda CGB, Shah BR, Yu FF, et al. A novel fully automated MRI-based deep-learning method for classification of 1p/19q co-deletion status in brain gliomas. *Neuro-oncology advances.* 2020; 2(1):vdaa066.
121. Clark K, Vendt B, Smith K, et al. The Cancer Imaging Archive (TCIA): maintaining and operating a public information repository. 2013; 26(6):1045-1057.
122. Ceccarelli M, Barthel FP, Malta TM, et al. Molecular profiling reveals biologically discrete subsets and pathways of progression in diffuse glioma. 2016; 164(3):550-563.
123. Avants BB, Tustison NJ, Song G, Cook PA, Klein A, Gee JC. A reproducible evaluation of ANTs similarity metric performance in brain image registration. *Neuroimage.* 2011; 54(3):2033-2044.
124. Smith SM. Fast robust automated brain extraction. *Human brain mapping.* 2002; 17(3):143-155.

125. Gallagher TA, Nemeth AJ, Hacein-Bey L. An introduction to the Fourier transform: relationship to MRI. *American journal of roentgenology*. 2008; 190(5):1396-1405.
126. Duffy BA, Zhang W, Tang H, et al. Retrospective correction of motion artifact affected structural MRI images using deep learning of simulated motion. *1st Conference on Medical Imaging with Deep Learning (MIDL 2018), Amsterdam, The Netherlands.* 2018.
127. Jégou S, Drozdzal M, Vazquez D, Romero A, Bengio Y. The one hundred layers tiramisu: Fully convolutional densenets for semantic segmentation. Paper presented at: Proceedings of the IEEE conference on computer vision and pattern recognition workshops2017.
128. Huang G, Liu Z, Van Der Maaten L, Weinberger KQ. Densely connected convolutional networks. Paper presented at: Proceedings of the IEEE conference on computer vision and pattern recognition2017.
129. Abadi M, Barham P, Chen J, et al. Tensorflow: A system for large-scale machine learning. Paper presented at: 12th {USENIX} symposium on operating systems design and implementation ({OSDI} 16)2016.
130. Duffy BA, Zhang W, Tang H, et al. Retrospective correction of motion artifact affected structural MRI images using deep learning of simulated motion. 2018.
131. Bahrami N, Hartman SJ, Chang Y-H, et al. Molecular classification of patients with grade II/III glioma using quantitative MRI characteristics. *Journal of neuro-oncology*. 2018; 139(3):633-642.
132. Zhang X, Tian Q, Wang L, et al. Radiomics strategy for molecular subtype stratification of lower-grade glioma: detecting IDH and TP53 mutations based on multimodal MRI. *Journal of Magnetic Resonance Imaging.* 2018; 48(4):916-926.
133. Isensee F, Jaeger PF, Kohl SAA, Petersen J, Maier-Hein KH. nnU-Net: a self-configuring method for deep learning-based biomedical image segmentation. *Nat Methods.* 2020.

SUPPLEMENTARY DATA

Supplementary Table 1: Subject wise IDH mutation status, clinical variables, and group membership for each fold of the cross-validation.

SUBJECT ID	Age	Gender	Histology	Grade	IDH status	IDH Allele	1p/19q co-deletion	Survival (months)	Karnofsky Performance score	Cross-validation group
TCGA-02-0003	50	male	glioblastoma	G4	WT	N/A	non-codel	4.7311	100	1
TCGA-02-0006	56	female	glioblastoma	G4	WT	N/A	non-codel	18.333	80	3
TCGA-02-0009	61	female	glioblastoma	G4	WT	N/A	non-codel	10.5793	80	1
TCGA-02-0011	18	female	glioblastoma	G4	WT	N/A	non-codel	20.6986	80	1
TCGA-02-0027	33	female	glioblastoma	G4	WT	N/A	non-codel	12.1563	100	2
TCGA-02-0033	54	male	glioblastoma	G4	WT	N/A	non-codel	2.8255	100	1
TCGA-02-0034	60	male	glioblastoma	G4	WT	N/A	non-codel	14.1276	80	3
TCGA-02-0037	74	female	glioblastoma	G4	WT	N/A	non-codel	3.614	80	1
TCGA-02-0046	61	male	glioblastoma	G4	WT	N/A	non-codel	6.8667	60	1
TCGA-02-0047	78	male	glioblastoma	G4	WT	N/A	non-codel	14.719	80	1
TCGA-02-0048	80	male	glioblastoma	G4	WT	N/A	non-codel	3.2198	NaN	2
TCGA-02-0054	44	female	glioblastoma	G4	WT	N/A	non-codel	6.5381	80	3
TCGA-02-0060	66	female	glioblastoma	G4	WT	N/A	non-codel	6.0124	80	1
TCGA-02-0064	50	male	glioblastoma	G4	WT	N/A	non-codel	19.7129	100	3
TCGA-02-0068	57	male	glioblastoma	G4	WT	N/A	non-codel	26.4153	80	1
TCGA-02-0069	31	female	glioblastoma	G4	WT	N/A	non-codel	28.6823	80	2
TCGA-02-0070	70	male	glioblastoma	G4	WT	N/A	non-codel	25.0354	80	2
TCGA-02-0075	63	male	glioblastoma	G4	WT	N/A	non-codel	20.83	80	2
TCGA-02-0085	63	female	glioblastoma	G4	WT	N/A	non-codel	51.2865	80	3
TCGA-02-0086	45	female	glioblastoma	G4	WT	N/A	non-codel	8.8051	100	1
TCGA-02-0102	42	male	glioblastoma	G4	WT	N/A	non-codel	27.0067	100	1
TCGA-06-0119	81	female	glioblastoma	G4	WT	N/A	non-codel	2.6941	NaN	2
TCGA-06-0122	84	female	glioblastoma	G4	WT	N/A	non-codel	6.1439	NaN	3
TCGA-06-0127	67	male	glioblastoma	G4	WT	N/A	non-codel	3.9754	60	1
TCGA-06-0128	66	male	glioblastoma	G4	Mutant	IDH1	non-codel	22.7027	80	1
TCGA-06-0129	30	male	glioblastoma	G4	Mutant	IDH1	non-codel	33.6434	100	1
TCGA-06-0130	54	male	glioblastoma	G4	WT	N/A	non-codel	12.9448	80	3
TCGA-06-0132	49	male	glioblastoma	G4	WT	N/A	non-codel	25.3311	NaN	3
TCGA-06-0133	64	male	glioblastoma	G4	WT	N/A	non-codel	14.2919	NaN	1
TCGA-06-0137	63	female	glioblastoma	G4	WT	N/A	non-codel	26.6782	NaN	3
TCGA-06-0138	43	male	glioblastoma	G4	WT	N/A	non-codel	24.2141	80	1
TCGA-06-0139	40	male	glioblastoma	G4	WT	N/A	non-codel	11.8935	60	1
TCGA-06-0142	81	male	glioblastoma	G4	WT	N/A	non-codel	2.2013	NaN	2
TCGA-06-0143	58	male	glioblastoma	G4	WT	N/A	non-codel	11.7292	60	2

TCGA-06-0145	53	female	glioblastoma	G4	WT	N/A	non-codel	2.3327	NaN	3
TCGA-06-0147	51	female	glioblastoma	G4	WT	N/A	non-codel	17.7745	NaN	2
TCGA-06-0154	54	male	glioblastoma	G4	WT	N/A	non-codel	13.9305	100	2
TCGA-06-0157	63	female	glioblastoma	G4	WT	N/A	non-codel	3.1869	40	2
TCGA-06-0158	73	male	glioblastoma	G4	WT	N/A	non-codel	10.8093	80	1
TCGA-06-0166	51	male	glioblastoma	G4	WT	N/A	non-codel	5.8482	NaN	1
TCGA-06-0168	59	female	glioblastoma	G4	WT	N/A	non-codel	19.6472	100	2
TCGA-06-0174	54	male	glioblastoma	G4	WT	N/A	non-codel	3.2198	80	2
TCGA-06-0176	34	male	glioblastoma	G4	WT	N/A	non-codel	51.3194	80	2
TCGA-06-0184	63	male	glioblastoma	G4	WT	N/A	non-codel	40.3458	80	2
TCGA-06-0185	54	male	glioblastoma	G4	WT	N/A	non-codel	36.9946	100	3
TCGA-06-0187	69	male	glioblastoma	G4	WT	N/A	non-codel	27.2039	60	3
TCGA-06-0188	71	male	glioblastoma	G4	WT	N/A	non-codel	28.4523	100	1
TCGA-06-0189	55	male	glioblastoma	G4	WT	N/A	non-codel	15.4089	NaN	1
TCGA-06-0190	62	male	glioblastoma	G4	WT	N/A	non-codel	10.415	80	2
TCGA-06-0192	58	male	glioblastoma	G4	WT	N/A	non-codel	18.3002	100	3
TCGA-06-0213	55	female	glioblastoma	G4	WT	N/A	non-codel	0.52568	NaN	3
TCGA-06-0237	75	female	glioblastoma	G4	WT	N/A	non-codel	13.6348	NaN	1
TCGA-06-0238	46	male	glioblastoma	G4	WT	N/A	non-codel	13.3062	80	2
TCGA-06-0241	65	female	glioblastoma	G4	WT	N/A	non-codel	14.949	100	1
TCGA-06-0644	71	male	glioblastoma	G4	WT	N/A	non-codel	12.3206	80	1
TCGA-06-0645	55	female	glioblastoma	G4	WT	N/A	non-codel	5.7496	NaN	3
TCGA-06-0646	60	male	glioblastoma	G4	WT	N/A	non-codel	5.7496	80	2
TCGA-06-0648	77	male	glioblastoma	G4	WT	N/A	non-codel	9.7908	80	3
TCGA-06-0649	73	female	glioblastoma	G4	WT	N/A	non-codel	2.1027	NaN	3
TCGA-06-1806	47	male	glioblastoma	G4	WT	N/A	non-codel	15.3104	90	2
TCGA-06-2570	21	female	glioblastoma	G4	Mutant	IDH1	non-codel	9.3636	100	1
TCGA-06-5408	54	female	glioblastoma	G4	WT	N/A	non-codel	11.7292	80	3
TCGA-06-5412	78	female	glioblastoma	G4	WT	N/A	non-codel	4.534	80	2
TCGA-06-5413	67	male	glioblastoma	G4	WT	N/A	non-codel	8.8051	60	3
TCGA-06-5417	45	female	glioblastoma	G4	Mutant	IDH1	NA	5.0925	80	2
TCGA-06-6389	49	female	glioblastoma	G4	Mutant	IDH1	non-codel	7.7866	100	2
TCGA-08-0390	69	male	glioblastoma	G4	WT	N/A	non-codel	13.9633	60	3
TCGA-12-0616	36	female	glioblastoma	G4	WT	N/A	non-codel	14.719	100	2
TCGA-12-0829	75	male	glioblastoma	G4	WT	N/A	non-codel	20.5672	80	2
TCGA-12-1093	66	female	glioblastoma	G4	WT	N/A	non-codel	15.9675	80	3
TCGA-12-1598	75	female	glioblastoma	G4	WT	N/A	non-codel	15.6389	NaN	2
TCGA-12-1601	NaN	NA	glioblastoma	NA	WT	N/A	NA	NaN	NaN	1
TCGA-12-1602	58	male	glioblastoma	G4	WT	N/A	non-codel	6.7681	60	1
TCGA-12-3650	46	male	glioblastoma	G4	WT	N/A	non-codel	10.9407	80	1
TCGA-14-0789	54	male	glioblastoma	G4	WT	N/A	non-codel	11.2364	40	3

TCGA-14-1456	23	male	glioblastoma	G4	Mutant	IDH1	non-codel	40.9372	80	2
TCGA-14-1794	59	male	glioblastoma	G4	WT	N/A	non-codel	0.98565	NaN	3
TCGA-14-1829	57	male	glioblastoma	G4	WT	N/A	non-codel	7.1624	60	2
TCGA-14-3477	38	female	glioblastoma	G4	WT	N/A	non-codel	3.7783	80	1
TCGA-19-1388	58	male	glioblastoma	G4	WT	N/A	non-codel	12.9448	NaN	1
TCGA-19-1390	63	female	glioblastoma	G4	WT	N/A	non-codel	25.364	60	1
TCGA-19-1789	69	female	glioblastoma	G4	WT	N/A	non-codel	3.2526	60	2
TCGA-19-2624	51	male	glioblastoma	G4	WT	N/A	non-codel	0.16427	NaN	3
TCGA-19-2631	74	female	glioblastoma	G4	WT	N/A	non-codel	6.9981	60	2
TCGA-19-5954	72	female	glioblastoma	G4	WT	N/A	non-codel	7.9509	60	3
TCGA-19-5958	56	male	glioblastoma	G4	WT	N/A	non-codel	5.3882	80	2
TCGA-27-1835	53	female	glioblastoma	G4	WT	N/A	non-codel	21.29	80	2
TCGA-27-1838	59	female	glioblastoma	G4	WT	N/A	non-codel	11.4992	80	2
TCGA-76-4926	68	male	glioblastoma	G4	WT	N/A	non-codel	4.534	80	3
TCGA-76-4932	50	female	glioblastoma	G4	WT	N/A	NA	47.9024	80	2
TCGA-76-4934	66	female	glioblastoma	G4	WT	N/A	non-codel	2.5298	80	3
TCGA-76-4935	52	female	glioblastoma	G4	WT	N/A	non-codel	10.7764	80	3
TCGA-76-6191	57	male	glioblastoma	G4	WT	N/A	non-codel	16.6903	80	1
TCGA-76-6192	74	male	glioblastoma	G4	WT	N/A	non-codel	3.2855	80	1
TCGA-76-6193	78	male	glioblastoma	G4	WT	N/A	non-codel	2.6941	60	1
TCGA-76-6280	57	male	glioblastoma	G4	WT	N/A	non-codel	11.3678	80	2
TCGA-76-6282	63	male	glioblastoma	G4	WT	N/A	non-codel	17.0517	80	2
TCGA-76-6285	64	female	glioblastoma	G4	WT	N/A	non-codel	8.3451	80	2
TCGA-76-6656	66	male	glioblastoma	G4	WT	N/A	non-codel	4.8297	60	3
TCGA-76-6657	74	male	glioblastoma	G4	WT	N/A	non-codel	5.0268	80	1
TCGA-76-6661	54	male	glioblastoma	G4	WT	N/A	non-codel	0.22998	60	3
TCGA-76-6662	58	male	glioblastoma	G4	WT	N/A	non-codel	9.2651	80	1
TCGA-76-6663	44	female	glioblastoma	G4	WT	N/A	non-codel	7.7209	80	1
TCGA-76-6664	49	female	glioblastoma	G4	WT	N/A	non-codel	7.7866	80	1
TCGA-CS-4941	67	male	astrocytoma	G3	WT	N/A	non-codel	7.688	90	3
TCGA-CS-4942	44	female	astrocytoma	G3	Mutant	IDH1	non-codel	43.8613	90	2
TCGA-CS-4943	37	male	astrocytoma	G3	Mutant	IDH1	non-codel	18.1359	50	3
TCGA-CS-4944	50	male	astrocytoma	G2	Mutant	IDH1	non-codel	10.6121	90	1
TCGA-CS-5393	39	male	astrocytoma	G3	Mutant	IDH1	non-codel	40.1487	100	2
TCGA-CS-5395	43	male	oligodendroglioma	G2	WT	N/A	non-codel	20.9943	90	3
TCGA-CS-5396	53	female	oligodendroglioma	G3	Mutant	IDH1	codel	9.955	90	2
TCGA-CS-5397	54	female	astrocytoma	G3	WT	N/A	non-codel	6.3739	80	2
TCGA-CS-6186	58	male	oligoastrocytoma	G3	WT	N/A	non-codel	17.6759	90	3
TCGA-CS-6188	48	male	astrocytoma	G3	WT	N/A	non-codel	23.8198	90	3
TCGA-CS-6290	31	male	astrocytoma	G3	Mutant	IDH1	non-codel	17.9388	90	2
TCGA-CS-6665	51	female	astrocytoma	G3	Mutant	IDH1	non-codel	12.4192	90	3

TCGA-CS-6666	22	male	astrocytoma	G3	Mutant	IDH1	non-codel	8.4766	90	1
TCGA-CS-6667	39	female	astrocytoma	G2	Mutant	IDH1	non-codel	7.5566	90	1
TCGA-CS-6668	57	female	oligodendroglioma	G2	Mutant	IDH1	codel	8.0166	90	1
TCGA-CS-6669	26	female	oligodendroglioma	G2	WT	N/A	non-codel	7.3924	90	1
TCGA-DU-5849	48	male	oligodendroglioma	G2	Mutant	IDH1	codel	14.5547	NaN	2
TCGA-DU-5851	40	female	oligoastrocytoma	G3	Mutant	IDH1	non-codel	17.446	90	3
TCGA-DU-5852	61	female	oligoastrocytoma	G3	WT	N/A	non-codel	6.7353	80	2
TCGA-DU-5853	29	male	oligoastrocytoma	G2	Mutant	IDH1	non-codel	13.3719	100	1
TCGA-DU-5854	57	female	astrocytoma	G3	WT	N/A	non-codel	8.4437	90	1
TCGA-DU-5855	49	female	oligoastrocytoma	G3	Mutant	IDH1	non-codel	6.801	100	2
TCGA-DU-5871	37	female	oligoastrocytoma	G2	Mutant	IDH1	non-codel	18.9244	100	3
TCGA-DU-5872	43	female	oligoastrocytoma	G2	Mutant	IDH1	non-codel	17.4788	NaN	1
TCGA-DU-5874	62	female	oligodendroglioma	G2	Mutant	IDH1	codel	15.1461	100	1
TCGA-DU-6395	31	male	oligoastrocytoma	G2	Mutant	IDH1	non-codel	48.9867	NaN	1
TCGA-DU-6397	45	male	oligodendroglioma	G3	Mutant	IDH1	codel	46.0297	NaN	3
TCGA-DU-6399	54	male	oligodendroglioma	G2	Mutant	IDH1	non-codel	65.7098	NaN	1
TCGA-DU-6400	66	female	oligodendroglioma	G2	Mutant	IDH1	codel	1.2156	NaN	3
TCGA-DU-6401	31	female	oligodendroglioma	G2	Mutant	IDH1	non-codel	87.394	NaN	1
TCGA-DU-6404	24	female	oligodendroglioma	G3	WT	N/A	non-codel	133.6537	100	3
TCGA-DU-6405	51	female	astrocytoma	G3	WT	N/A	non-codel	19.8772	90	1
TCGA-DU-6407	35	female	oligodendroglioma	G2	Mutant	IDH1	non-codel	94.4578	90	2
TCGA-DU-6408	23	female	oligodendroglioma	G3	Mutant	IDH1	non-codel	114.0065	90	2
TCGA-DU-6542	25	male	oligoastrocytoma	G3	Mutant	IDH1	non-codel	7.7209	NaN	1
TCGA-DU-7008	41	female	oligodendroglioma	G2	Mutant	IDH1	non-codel	156.1265	NaN	3
TCGA-DU-7010	58	female	astrocytoma	G3	Mutant	IDH1	non-codel	14.9818	NaN	2
TCGA-DU-7015	41	female	oligodendroglioma	G2	Mutant	IDH1	non-codel	90.7124	90	1
TCGA-DU-7018	57	female	oligodendroglioma	G3	Mutant	IDH1	codel	30.6536	90	2
TCGA-DU-7019	39	male	oligoastrocytoma	G3	Mutant	IDH1	non-codel	26.2839	100	3
TCGA-DU-7294	53	female	oligodendroglioma	G2	Mutant	IDH1	codel	94.2607	100	3
TCGA-DU-7298	38	female	astrocytoma	G3	Mutant	IDH1	non-codel	18.9244	80	2
TCGA-DU-7299	33	male	astrocytoma	G3	Mutant	IDH1	non-codel	43.9927	90	3
TCGA-DU-7300	53	female	oligodendroglioma	G3	Mutant	IDH1	codel	61.9643	90	3
TCGA-DU-7301	53	male	oligodendroglioma	G2	Mutant	IDH1	non-codel	25.8897	100	1
TCGA-DU-7302	48	female	oligodendroglioma	G3	Mutant	IDH1	codel	60.2559	90	2
TCGA-DU-7304	43	male	oligoastrocytoma	G3	Mutant	IDH1	non-codel	23.2941	80	2
TCGA-DU-7306	67	male	oligoastrocytoma	G2	Mutant	IDH1	non-codel	41.9557	100	2
TCGA-DU-7309	41	female	oligodendroglioma	G3	Mutant	IDH2	non-codel	2.7598	90	3
TCGA-DU-8162	61	female	oligoastrocytoma	G3	WT	N/A	non-codel	14.5876	80	2
TCGA-DU-8163	29	male	oligoastrocytoma	G3	Mutant	IDH1	non-codel	20.6657	90	3
TCGA-DU-8164	51	male	oligodendroglioma	G2	Mutant	IDH1	codel	21.3885	NaN	3
TCGA-DU-8165	60	female	oligodendroglioma	G3	WT	N/A	non-codel	19.1216	90	3

TCGA-DU-8166	29	female	oligoastrocytoma	G2	Mutant	IDH1	non-codel	16.9531	NaN	3
TCGA-DU-8167	69	female	oligoastrocytoma	G2	Mutant	IDH1	non-codel	15.4747	100	2
TCGA-DU-8168	55	female	oligodendroglioma	G3	Mutant	IDH1	codel	14.1605	70	2
TCGA-DU-A5TP	33	male	astrocytoma	G3	Mutant	IDH1	non-codel	14.2262	70	1
TCGA-DU-A5TR	51	male	oligoastrocytoma	G2	Mutant	IDH1	non-codel	12.5834	90	1
TCGA-DU-A5TS	42	male	oligodendroglioma	G2	Mutant	IDH1	non-codel	15.1133	100	2
TCGA-DU-A5TT	70	male	oligodendroglioma	G3	WT	N/A	non-codel	4.9611	NaN	1
TCGA-DU-A5TU	62	female	astrocytoma	G2	Mutant	IDH1	non-codel	3.6469	50	1
TCGA-DU-A5TW	33	female	astrocytoma	G3	Mutant	IDH1	non-codel	5.651	100	1
TCGA-DU-A5TY	46	female	astrocytoma	G3	WT	N/A	non-codel	12.1892	NaN	2
TCGA-DU-A6S2	37	female	oligodendroglioma	G2	Mutant	IDH1	codel	8.6408	70	3
TCGA-DU-A6S3	60	male	oligodendroglioma	G2	Mutant	IDH1	codel	2.6941	NaN	3
TCGA-DU-A6S6	35	female	oligoastrocytoma	G2	Mutant	IDH1	codel	77.9318	90	1
TCGA-DU-A6S7	27	female	astrocytoma	G3	Mutant	IDH1	non-codel	7.2281	90	1
TCGA-DU-A6S8	74	female	oligodendroglioma	G3	Mutant	IDH1	codel	5.9796	90	3
TCGA-FG-5964	62	male	oligodendroglioma	G2	Mutant	IDH1	codel	34.3334	NaN	3
TCGA-FG-6688	59	female	astrocytoma	G3	WT	N/A	non-codel	18.7601	80	2
TCGA-FG-6689	30	male	astrocytoma	G2	Mutant	IDH1	non-codel	14.9161	70	3
TCGA-FG-6690	70	male	oligodendroglioma	G2	Mutant	IDH1	non-codel	24.9697	90	2
TCGA-FG-6691	23	female	astrocytoma	G2	Mutant	IDH1	non-codel	23.9512	100	2
TCGA-FG-6692	63	male	oligodendroglioma	G3	WT	N/A	non-codel	18.4316	NaN	3
TCGA-FG-7634	28	male	oligodendroglioma	G2	Mutant	IDH1	codel	15.3432	NaN	3
TCGA-FG-7643	49	female	oligoastrocytoma	G2	WT	N/A	non-codel	20.0743	NaN	2
TCGA-FG-8189	33	female	oligodendroglioma	G2	Mutant	IDH2	non-codel	11.8606	70	2
TCGA-FG-A4MT	27	female	oligodendroglioma	G2	Mutant	IDH1	non-codel	38.2431	100	1
TCGA-FG-A6IZ	60	male	oligodendroglioma	G2	Mutant	IDH1	codel	4.2054	NaN	2
TCGA-FG-A713	74	female	oligoastrocytoma	G2	Mutant	IDH1	codel	5.2239	60	3
TCGA-HT-7473	28	male	oligoastrocytoma	G2	Mutant	IDH1	non-codel	16.526	NaN	1
TCGA-HT-7475	67	male	oligoastrocytoma	G3	Mutant	IDH1	non-codel	17.4131	70	2
TCGA-HT-7602	21	male	oligodendroglioma	G2	Mutant	IDH1	non-codel	29.8322	NaN	3
TCGA-HT-7604	50	male	astrocytoma	G2	Mutant	IDH1	non-codel	107.8626	NaN	1
TCGA-HT-7605	38	male	oligodendroglioma	G2	Mutant	IDH1	codel	4.5668	NaN	1
TCGA-HT-7608	61	male	oligoastrocytoma	G2	Mutant	IDH1	codel	22.0456	NaN	3
TCGA-HT-7616	75	male	oligodendroglioma	G3	Mutant	IDH1	codel	0.22998	NaN	3
TCGA-HT-7680	32	female	astrocytoma	G2	WT	N/A	non-codel	0.75566	NaN	3
TCGA-HT-7686	29	female	astrocytoma	G3	Mutant	IDH1	non-codel	42.7114	NaN	3
TCGA-HT-7690	29	male	oligoastrocytoma	G3	Mutant	IDH1	non-codel	0.098565	NaN	2
TCGA-HT-7692	43	male	oligoastrocytoma	G2	Mutant	IDH1	codel	2.9569	100	2
TCGA-HT-7693	51	female	oligodendroglioma	G2	Mutant	IDH1	non-codel	17.5117	90	1
TCGA-HT-7694	60	male	oligodendroglioma	G3	Mutant	IDH1	codel	6.8995	90	3
TCGA-HT-7855	39	male	astrocytoma	G3	Mutant	IDH1	non-codel	19.2201	NaN	2

TCGA-HT-7856	35	male	oligodendroglioma	G3	Mutant	IDH2	codel	39.0645	NaN	2
TCGA-HT-7860	60	female	astrocytoma	G3	WT	N/A	non-codel	0.49282	NaN	2
TCGA-HT-7874	41	female	oligodendroglioma	G3	Mutant	IDH1	codel	37.126	NaN	3
TCGA-HT-7879	31	male	oligoastrocytoma	G3	Mutant	IDH1	non-codel	3.6797	NaN	3
TCGA-HT-7882	66	male	oligodendroglioma	G3	WT	N/A	non-codel	3.7126	NaN	1
TCGA-HT-7884	44	female	astrocytoma	G2	Mutant	IDH1	non-codel	11.2692	80	1
TCGA-HT-8018	40	female	oligoastrocytoma	G2	Mutant	IDH1	non-codel	21.4871	NaN	3
TCGA-HT-8105	54	male	oligodendroglioma	G3	Mutant	IDH1	codel	6.2424	NaN	2
TCGA-HT-8106	53	male	astrocytoma	G3	Mutant	IDH1	non-codel	0.098565	NaN	1
TCGA-HT-8107	62	male	oligodendroglioma	G2	WT	N/A	non-codel	0.45997	NaN	3
TCGA-HT-8111	32	male	oligoastrocytoma	G3	Mutant	IDH1	non-codel	0.22998	NaN	3
TCGA-HT-8113	49	female	oligodendroglioma	G2	Mutant	IDH2	non-codel	29.5694	NaN	1
TCGA-HT-8114	36	male	oligoastrocytoma	G3	Mutant	IDH1	non-codel	3.8769	NaN	1
TCGA-HT-8563	30	female	astrocytoma	G3	Mutant	IDH1	non-codel	16.0332	NaN	2
TCGA-HT-A5RC	70	female	astrocytoma	G3	WT	N/A	non-codel	5.3225	40	3
TCGA-HT-A61A	20	female	oligodendroglioma	G2	Mutant	IDH1	non-codel	6.3739	80	1

Supplementary Table 2: Subject wise 1p/19q co-deletion status, clinical variables, and group membership for each fold of the cross-validation.

SUBJECT ID	Age	Gender	Histology	Grade	Data Collection	IDH Status	IDH Allele	1p/19q co-deletion	Cross-validation group
TCGA-02-0003	50	male	glioblastoma	G4	HGG	WT	N/A	non-codel	2
TCGA-02-0006	56	female	glioblastoma	G4	HGG	WT	N/A	non-codel	3
TCGA-02-0009	61	female	glioblastoma	G4	HGG	WT	N/A	non-codel	1
TCGA-02-0011	18	female	glioblastoma	G4	HGG	WT	N/A	non-codel	1
TCGA-02-0027	33	female	glioblastoma	G4	HGG	WT	N/A	non-codel	1
TCGA-02-0033	54	male	glioblastoma	G4	HGG	WT	N/A	non-codel	1
TCGA-02-0034	60	male	glioblastoma	G4	HGG	WT	N/A	non-codel	3
TCGA-02-0037	74	female	glioblastoma	G4	HGG	WT	N/A	non-codel	2
TCGA-02-0046	61	male	glioblastoma	G4	HGG	WT	N/A	non-codel	2
TCGA-02-0047	78	male	glioblastoma	G4	HGG	WT	N/A	non-codel	3
TCGA-02-0048	80	male	glioblastoma	G4	HGG	WT	N/A	non-codel	3
TCGA-02-0054	44	female	glioblastoma	G4	HGG	WT	N/A	non-codel	1
TCGA-02-0060	66	female	glioblastoma	G4	HGG	WT	N/A	non-codel	3
TCGA-02-0064	50	male	glioblastoma	G4	HGG	WT	N/A	non-codel	3
TCGA-02-0068	57	male	glioblastoma	G4	HGG	WT	N/A	non-codel	2
TCGA-02-0069	31	female	glioblastoma	G4	HGG	WT	N/A	non-codel	1
TCGA-02-0070	70	male	glioblastoma	G4	HGG	WT	N/A	non-codel	2
TCGA-02-0075	63	male	glioblastoma	G4	HGG	WT	N/A	non-codel	2

TCGA-02-0085	63	female	glioblastoma	G4	HGG	WT	N/A	non-codel	3
TCGA-02-0086	45	female	glioblastoma	G4	HGG	WT	N/A	non-codel	1
TCGA-02-0102	42	male	glioblastoma	G4	HGG	WT	N/A	non-codel	2
TCGA-06-0119	81	female	glioblastoma	G4	HGG	WT	N/A	non-codel	2
TCGA-06-0122	84	female	glioblastoma	G4	HGG	WT	N/A	non-codel	3
TCGA-06-0127	67	male	glioblastoma	G4	HGG	WT	N/A	non-codel	1
TCGA-06-0128	66	male	glioblastoma	G4	HGG	Mutant	IDH1	non-codel	1
TCGA-06-0129	30	male	glioblastoma	G4	HGG	Mutant	IDH1	non-codel	3
TCGA-06-0132	49	male	glioblastoma	G4	HGG	WT	N/A	non-codel	2
TCGA-06-0133	64	male	glioblastoma	G4	HGG	WT	N/A	non-codel	3
TCGA-06-0137	63	female	glioblastoma	G4	HGG	WT	N/A	non-codel	2
TCGA-06-0138	43	male	glioblastoma	G4	HGG	WT	N/A	non-codel	2
TCGA-06-0139	40	male	glioblastoma	G4	HGG	WT	N/A	non-codel	2
TCGA-06-0142	81	male	glioblastoma	G4	HGG	WT	N/A	non-codel	3
TCGA-06-0143	58	male	glioblastoma	G4	HGG	WT	N/A	non-codel	3
TCGA-06-0145	53	female	glioblastoma	G4	HGG	WT	N/A	non-codel	3
TCGA-06-0147	51	female	glioblastoma	G4	HGG	WT	N/A	non-codel	1
TCGA-06-0154	54	male	glioblastoma	G4	HGG	WT	N/A	non-codel	2
TCGA-06-0157	63	female	glioblastoma	G4	HGG	WT	N/A	non-codel	1
TCGA-06-0158	73	male	glioblastoma	G4	HGG	WT	N/A	non-codel	3
TCGA-06-0166	51	male	glioblastoma	G4	HGG	WT	N/A	non-codel	1
TCGA-06-0168	59	female	glioblastoma	G4	HGG	WT	N/A	non-codel	1
TCGA-06-0174	54	male	glioblastoma	G4	HGG	WT	N/A	non-codel	2
TCGA-06-0176	34	male	glioblastoma	G4	HGG	WT	N/A	non-codel	2
TCGA-06-0184	63	male	glioblastoma	G4	HGG	WT	N/A	non-codel	3
TCGA-06-0185	54	male	glioblastoma	G4	HGG	WT	N/A	non-codel	1
TCGA-06-0187	69	male	glioblastoma	G4	HGG	WT	N/A	non-codel	3
TCGA-06-0188	71	male	glioblastoma	G4	HGG	WT	N/A	non-codel	3
TCGA-06-0189	55	male	glioblastoma	G4	HGG	WT	N/A	non-codel	1
TCGA-06-0190	62	male	glioblastoma	G4	HGG	WT	N/A	non-codel	2
TCGA-06-0192	58	male	glioblastoma	G4	HGG	WT	N/A	non-codel	1
TCGA-06-0213	55	female	glioblastoma	G4	HGG	WT	N/A	non-codel	2
TCGA-06-0237	75	female	glioblastoma	G4	HGG	WT	N/A	non-codel	2
TCGA-06-0238	46	male	glioblastoma	G4	HGG	WT	N/A	non-codel	2
TCGA-06-0241	65	female	glioblastoma	G4	HGG	WT	N/A	non-codel	1
TCGA-06-0644	71	male	glioblastoma	G4	HGG	WT	N/A	non-codel	3
TCGA-06-0645	55	female	glioblastoma	G4	HGG	WT	N/A	non-codel	1
TCGA-06-0646	60	male	glioblastoma	G4	HGG	WT	N/A	non-codel	1
TCGA-06-0648	77	male	glioblastoma	G4	HGG	WT	N/A	non-codel	1
TCGA-06-0649	73	female	glioblastoma	G4	HGG	WT	N/A	non-codel	2
TCGA-06-1806	47	male	glioblastoma	G4	HGG	WT	N/A	non-codel	2

TCGA-06-2570	21	female	glioblastoma	G4	HGG	Mutant	IDH1	non-codel	1
TCGA-06-5408	54	female	glioblastoma	G4	HGG	WT	N/A	non-codel	2
TCGA-06-5412	78	female	glioblastoma	G4	HGG	WT	N/A	non-codel	3
TCGA-06-5413	67	male	glioblastoma	G4	HGG	WT	N/A	non-codel	1
TCGA-06-6389	49	female	glioblastoma	G4	HGG	Mutant	IDH1	non-codel	2
TCGA-08-0390	69	male	glioblastoma	G4	HGG	WT	N/A	non-codel	3
TCGA-12-0616	36	female	glioblastoma	G4	HGG	WT	N/A	non-codel	1
TCGA-12-0829	75	male	glioblastoma	G4	HGG	WT	N/A	non-codel	3
TCGA-12-1093	66	female	glioblastoma	G4	HGG	WT	N/A	non-codel	2
TCGA-12-1598	75	female	glioblastoma	G4	HGG	WT	N/A	non-codel	2
TCGA-12-1602	58	male	glioblastoma	G4	HGG	WT	N/A	non-codel	2
TCGA-12-3650	46	male	glioblastoma	G4	HGG	WT	N/A	non-codel	3
TCGA-14-0789	54	male	glioblastoma	G4	HGG	WT	N/A	non-codel	3
TCGA-14-1456	23	male	glioblastoma	G4	HGG	Mutant	IDH1	non-codel	2
TCGA-14-1794	59	male	glioblastoma	G4	HGG	WT	N/A	non-codel	3
TCGA-14-1829	57	male	glioblastoma	G4	HGG	WT	N/A	non-codel	1
TCGA-14-3477	38	female	glioblastoma	G4	HGG	WT	N/A	non-codel	2
TCGA-19-1388	58	male	glioblastoma	G4	HGG	WT	N/A	non-codel	1
TCGA-19-1390	63	female	glioblastoma	G4	HGG	WT	N/A	non-codel	1
TCGA-19-1789	69	female	glioblastoma	G4	HGG	WT	N/A	non-codel	2
TCGA-19-2624	51	male	glioblastoma	G4	HGG	WT	N/A	non-codel	3
TCGA-19-2631	74	female	glioblastoma	G4	HGG	WT	N/A	non-codel	1
TCGA-19-5954	72	female	glioblastoma	G4	HGG	WT	N/A	non-codel	3
TCGA-19-5958	56	male	glioblastoma	G4	HGG	WT	N/A	non-codel	1
TCGA-27-1835	53	female	glioblastoma	G4	HGG	WT	N/A	non-codel	3
TCGA-27-1838	59	female	glioblastoma	G4	HGG	WT	N/A	non-codel	2
TCGA-76-4926	68	male	glioblastoma	G4	HGG	WT	N/A	non-codel	3
TCGA-76-4934	66	female	glioblastoma	G4	HGG	WT	N/A	non-codel	2
TCGA-76-4935	52	female	glioblastoma	G4	HGG	WT	N/A	non-codel	3
TCGA-76-6191	57	male	glioblastoma	G4	HGG	WT	N/A	non-codel	3
TCGA-76-6192	74	male	glioblastoma	G4	HGG	WT	N/A	non-codel	1
TCGA-76-6193	78	male	glioblastoma	G4	HGG	WT	N/A	non-codel	3
TCGA-76-6280	57	male	glioblastoma	G4	HGG	WT	N/A	non-codel	2
TCGA-76-6282	63	male	glioblastoma	G4	HGG	WT	N/A	non-codel	2
TCGA-76-6285	64	female	glioblastoma	G4	HGG	WT	N/A	non-codel	2
TCGA-76-6656	66	male	glioblastoma	G4	HGG	WT	N/A	non-codel	3
TCGA-76-6657	74	male	glioblastoma	G4	HGG	WT	N/A	non-codel	1
TCGA-76-6661	54	male	glioblastoma	G4	HGG	WT	N/A	non-codel	1
TCGA-76-6662	58	male	glioblastoma	G4	HGG	WT	N/A	non-codel	1
TCGA-76-6663	44	female	glioblastoma	G4	HGG	WT	N/A	non-codel	1
TCGA-76-6664	49	female	glioblastoma	G4	HGG	WT	N/A	non-codel	2

TCGA-CS-4941	67	male	astrocytoma	G3	LGG	WT	N/A	non-codel	2
TCGA-CS-4942	44	female	astrocytoma	G3	LGG	Mutant	IDH1	non-codel	2
TCGA-CS-4943	37	male	astrocytoma	G3	LGG	Mutant	IDH1	non-codel	2
TCGA-CS-4944	50	male	astrocytoma	G2	LGG	Mutant	IDH1	non-codel	3
TCGA-CS-5393	39	male	astrocytoma	G3	LGG	Mutant	IDH1	non-codel	3
TCGA-CS-5395	43	male	oligodendroglioma	G2	LGG	WT	N/A	non-codel	2
TCGA-CS-5396	53	female	oligodendroglioma	G3	LGG	Mutant	IDH1	codel	2
TCGA-CS-5397	54	female	astrocytoma	G3	LGG	WT	N/A	non-codel	3
TCGA-CS-6186	58	male	oligoastrocytoma	G3	LGG	WT	N/A	non-codel	1
TCGA-CS-6188	48	male	astrocytoma	G3	LGG	WT	N/A	non-codel	1
TCGA-CS-6290	31	male	astrocytoma	G3	LGG	Mutant	IDH1	non-codel	3
TCGA-CS-6665	51	female	astrocytoma	G3	LGG	Mutant	IDH1	non-codel	2
TCGA-CS-6666	22	male	astrocytoma	G3	LGG	Mutant	IDH1	non-codel	3
TCGA-CS-6667	39	female	astrocytoma	G2	LGG	Mutant	IDH1	non-codel	1
TCGA-CS-6668	57	female	oligodendroglioma	G2	LGG	Mutant	IDH1	codel	2
TCGA-CS-6669	26	female	oligodendroglioma	G2	LGG	WT	N/A	non-codel	1
TCGA-DU-5849	48	male	oligodendroglioma	G2	LGG	Mutant	IDH1	codel	1
TCGA-DU-5851	40	female	oligoastrocytoma	G3	LGG	Mutant	IDH1	non-codel	3
TCGA-DU-5852	61	female	oligoastrocytoma	G3	LGG	WT	N/A	non-codel	1
TCGA-DU-5853	29	male	oligoastrocytoma	G2	LGG	Mutant	IDH1	non-codel	3
TCGA-DU-5854	57	female	astrocytoma	G3	LGG	WT	N/A	non-codel	2
TCGA-DU-5855	49	female	oligoastrocytoma	G3	LGG	Mutant	IDH1	non-codel	1
TCGA-DU-5871	37	female	oligoastrocytoma	G2	LGG	Mutant	IDH1	non-codel	2
TCGA-DU-5872	43	female	oligoastrocytoma	G2	LGG	Mutant	IDH1	non-codel	1
TCGA-DU-5874	62	female	oligodendroglioma	G2	LGG	Mutant	IDH1	codel	2
TCGA-DU-6395	31	male	oligoastrocytoma	G2	LGG	Mutant	IDH1	non-codel	1
TCGA-DU-6397	45	male	oligodendroglioma	G3	LGG	Mutant	IDH1	codel	2
TCGA-DU-6399	54	male	oligodendroglioma	G2	LGG	Mutant	IDH1	non-codel	2
TCGA-DU-6400	66	female	oligodendroglioma	G2	LGG	Mutant	IDH1	codel	1
TCGA-DU-6401	31	female	oligodendroglioma	G2	LGG	Mutant	IDH1	non-codel	3
TCGA-DU-6404	24	female	oligodendroglioma	G3	LGG	WT	N/A	non-codel	3
TCGA-DU-6405	51	female	astrocytoma	G3	LGG	WT	N/A	non-codel	3
TCGA-DU-6407	35	female	oligodendroglioma	G2	LGG	Mutant	IDH1	non-codel	3
TCGA-DU-6408	23	female	oligodendroglioma	G3	LGG	Mutant	IDH1	non-codel	3
TCGA-DU-7008	41	female	oligodendroglioma	G2	LGG	Mutant	IDH1	non-codel	2
TCGA-DU-7010	58	female	astrocytoma	G3	LGG	Mutant	IDH1	non-codel	1
TCGA-DU-7015	41	female	oligodendroglioma	G2	LGG	Mutant	IDH1	non-codel	3
TCGA-DU-7018	57	female	oligodendroglioma	G3	LGG	Mutant	IDH1	codel	1
TCGA-DU-7019	39	male	oligoastrocytoma	G3	LGG	Mutant	IDH1	non-codel	2
TCGA-DU-7294	53	female	oligodendroglioma	G2	LGG	Mutant	IDH1	codel	2
TCGA-DU-7298	38	female	astrocytoma	G3	LGG	Mutant	IDH1	non-codel	1

TCGA-DU-7299	33	male	astrocytoma	G3	LGG	Mutant	IDH1	non-codel	1
TCGA-DU-7300	53	female	oligodendroglioma	G3	LGG	Mutant	IDH1	codel	3
TCGA-DU-7301	53	male	oligodendroglioma	G2	LGG	Mutant	IDH1	non-codel	2
TCGA-DU-7302	48	female	oligodendroglioma	G3	LGG	Mutant	IDH1	codel	3
TCGA-DU-7304	43	male	oligoastrocytoma	G3	LGG	Mutant	IDH1	non-codel	1
TCGA-DU-7306	67	male	oligoastrocytoma	G2	LGG	Mutant	IDH1	non-codel	1
TCGA-DU-7309	41	female	oligodendroglioma	G3	LGG	Mutant	IDH2	non-codel	3
TCGA-DU-8162	61	female	oligoastrocytoma	G3	LGG	WT	N/A	non-codel	2
TCGA-DU-8163	29	male	oligoastrocytoma	G3	LGG	Mutant	IDH1	non-codel	3
TCGA-DU-8164	51	male	oligodendroglioma	G2	LGG	Mutant	IDH1	codel	1
TCGA-DU-8165	60	female	oligodendroglioma	G3	LGG	WT	N/A	non-codel	3
TCGA-DU-8166	29	female	oligoastrocytoma	G2	LGG	Mutant	IDH1	non-codel	2
TCGA-DU-8167	69	female	oligoastrocytoma	G2	LGG	Mutant	IDH1	non-codel	2
TCGA-DU-8168	55	female	oligodendroglioma	G3	LGG	Mutant	IDH1	codel	3
TCGA-DU-A5TP	33	male	astrocytoma	G3	LGG	Mutant	IDH1	non-codel	2
TCGA-DU-A5TR	51	male	oligoastrocytoma	G2	LGG	Mutant	IDH1	non-codel	2
TCGA-DU-A5TS	42	male	oligodendroglioma	G2	LGG	Mutant	IDH1	non-codel	1
TCGA-DU-A5TT	70	male	oligodendroglioma	G3	LGG	WT	N/A	non-codel	2
TCGA-DU-A5TU	62	female	astrocytoma	G2	LGG	Mutant	IDH1	non-codel	2
TCGA-DU-A5TW	33	female	astrocytoma	G3	LGG	Mutant	IDH1	non-codel	2
TCGA-DU-A5TY	46	female	astrocytoma	G3	LGG	WT	N/A	non-codel	2
TCGA-DU-A6S2	37	female	oligodendroglioma	G2	LGG	Mutant	IDH1	codel	2
TCGA-DU-A6S3	60	male	oligodendroglioma	G2	LGG	Mutant	IDH1	codel	3
TCGA-DU-A6S6	35	female	oligoastrocytoma	G2	LGG	Mutant	IDH1	codel	1
TCGA-DU-A6S7	27	female	astrocytoma	G3	LGG	Mutant	IDH1	non-codel	3
TCGA-DU-A6S8	74	female	oligodendroglioma	G3	LGG	Mutant	IDH1	codel	1
TCGA-FG-5964	62	male	oligodendroglioma	G2	LGG	Mutant	IDH1	codel	2
TCGA-FG-6688	59	female	astrocytoma	G3	LGG	WT	N/A	non-codel	1
TCGA-FG-6689	30	male	astrocytoma	G2	LGG	Mutant	IDH1	non-codel	1
TCGA-FG-6690	70	male	oligodendroglioma	G2	LGG	Mutant	IDH1	non-codel	3
TCGA-FG-6691	23	female	astrocytoma	G2	LGG	Mutant	IDH1	non-codel	1
TCGA-FG-6692	63	male	oligodendroglioma	G3	LGG	WT	N/A	non-codel	3
TCGA-FG-7634	28	male	oligodendroglioma	G2	LGG	Mutant	IDH1	codel	2
TCGA-FG-7643	49	female	oligoastrocytoma	G2	LGG	WT	N/A	non-codel	1
TCGA-FG-8189	33	female	oligodendroglioma	G2	LGG	Mutant	IDH2	non-codel	2
TCGA-FG-A4MT	27	female	oligodendroglioma	G2	LGG	Mutant	IDH1	non-codel	2
TCGA-FG-A6IZ	60	male	oligodendroglioma	G2	LGG	Mutant	IDH1	codel	3
TCGA-FG-A713	74	female	oligoastrocytoma	G2	LGG	Mutant	IDH1	codel	1
TCGA-HT-7473	28	male	oligoastrocytoma	G2	LGG	Mutant	IDH1	non-codel	3
TCGA-HT-7475	67	male	oligoastrocytoma	G3	LGG	Mutant	IDH1	non-codel	3
TCGA-HT-7602	21	male	oligodendroglioma	G2	LGG	Mutant	IDH1	non-codel	3

TCGA-HT-7604	50	male	astrocytoma	G2	LGG	Mutant	IDH1	non-codel	1
TCGA-HT-7605	38	male	oligodendroglioma	G2	LGG	Mutant	IDH1	codel	3
TCGA-HT-7608	61	male	oligoastrocytoma	G2	LGG	Mutant	IDH1	codel	3
TCGA-HT-7616	75	male	oligodendroglioma	G3	LGG	Mutant	IDH1	codel	2
TCGA-HT-7680	32	female	astrocytoma	G2	LGG	WT	N/A	non-codel	1
TCGA-HT-7686	29	female	astrocytoma	G3	LGG	Mutant	IDH1	non-codel	2
TCGA-HT-7690	29	male	oligoastrocytoma	G3	LGG	Mutant	IDH1	non-codel	3
TCGA-HT-7692	43	male	oligoastrocytoma	G2	LGG	Mutant	IDH1	codel	3
TCGA-HT-7693	51	female	oligodendroglioma	G2	LGG	Mutant	IDH1	non-codel	1
TCGA-HT-7694	60	male	oligodendroglioma	G3	LGG	Mutant	IDH1	codel	1
TCGA-HT-7855	39	male	astrocytoma	G3	LGG	Mutant	IDH1	non-codel	1
TCGA-HT-7856	35	male	oligodendroglioma	G3	LGG	Mutant	IDH2	codel	1
TCGA-HT-7860	60	female	astrocytoma	G3	LGG	WT	N/A	non-codel	1
TCGA-HT-7874	41	female	oligodendroglioma	G3	LGG	Mutant	IDH1	codel	1
TCGA-HT-7879	31	male	oligoastrocytoma	G3	LGG	Mutant	IDH1	non-codel	3
TCGA-HT-7882	66	male	oligodendroglioma	G3	LGG	WT	N/A	non-codel	2
TCGA-HT-7884	44	female	astrocytoma	G2	LGG	Mutant	IDH1	non-codel	1
TCGA-HT-8018	40	female	oligoastrocytoma	G2	LGG	Mutant	IDH1	non-codel	1
TCGA-HT-8105	54	male	oligodendroglioma	G3	LGG	Mutant	IDH1	codel	3
TCGA-HT-8106	53	male	astrocytoma	G3	LGG	Mutant	IDH1	non-codel	3
TCGA-HT-8107	62	male	oligodendroglioma	G2	LGG	WT	N/A	non-codel	3
TCGA-HT-8111	32	male	oligoastrocytoma	G3	LGG	Mutant	IDH1	non-codel	2
TCGA-HT-8113	49	female	oligodendroglioma	G2	LGG	Mutant	IDH2	non-codel	2
TCGA-HT-8114	36	male	oligoastrocytoma	G3	LGG	Mutant	IDH1	non-codel	2
TCGA-HT-8563	30	female	astrocytoma	G3	LGG	Mutant	IDH1	non-codel	3
TCGA-HT-A5RC	70	female	astrocytoma	G3	LGG	WT	N/A	non-codel	3
TCGA-HT-A61A	20	female	oligodendroglioma	G2	LGG	Mutant	IDH1	non-codel	1
LGG-104	NaN	NaN	Oligoastrocytoma	G3	LGG	NaN	NaN	codel	1
LGG-203	NaN	NaN	Astrocytoma	G3	LGG	NaN	NaN	non-codel	1
LGG-210	NaN	NaN	Oligoastrocytoma	G2	LGG	NaN	NaN	non-codel	1
LGG-216	NaN	NaN	Oligoastrocytoma	G2	LGG	NaN	NaN	codel	2
LGG-218	NaN	NaN	Oligodendroglioma	G2	LGG	NaN	NaN	codel	1
LGG-219	NaN	NaN	Astrocytoma	G3	LGG	NaN	NaN	non-codel	3
LGG-220	NaN	NaN	Oligodendroglioma	G2	LGG	NaN	NaN	codel	1
LGG-223	NaN	NaN	Oligodendroglioma	G3	LGG	NaN	NaN	codel	1
LGG-225	NaN	NaN	Oligoastrocytoma	G2	LGG	NaN	NaN	codel	2
LGG-229	NaN	NaN	Oligodendroglioma	G2	LGG	NaN	NaN	codel	2
LGG-231	NaN	NaN	Oligoastrocytoma	G3	LGG	NaN	NaN	codel	1
LGG-233	NaN	NaN	Oligodendroglioma	G2	LGG	NaN	NaN	codel	3
LGG-234	NaN	NaN	Oligodendroglioma	G3	LGG	NaN	NaN	non-codel	3
LGG-240	NaN	NaN	Astrocytoma	G3	LGG	NaN	NaN	non-codel	3

LGG-241	NaN	NaN	Oligoastrocytoma	G2	LGG	NaN	NaN	non-codel	2
LGG-246	NaN	NaN	Oligoastrocytoma	G3	LGG	NaN	NaN	codel	3
LGG-249	NaN	NaN	Oligodendroglioma	G2	LGG	NaN	NaN	codel	3
LGG-254	NaN	NaN	Oligodendroglioma	G3	LGG	NaN	NaN	codel	2
LGG-260	NaN	NaN	Oligodendroglioma	G3	LGG	NaN	NaN	codel	1
LGG-261	NaN	NaN	Oligodendroglioma	G2	LGG	NaN	NaN	codel	1
LGG-263	NaN	NaN	Oligoastrocytoma	G3	LGG	NaN	NaN	non-codel	3
LGG-269	NaN	NaN	Oligodendroglioma	G3	LGG	NaN	NaN	codel	3
LGG-273	NaN	NaN	Oligoastrocytoma	G3	LGG	NaN	NaN	non-codel	1
LGG-274	NaN	NaN	Oligoastrocytoma	G2	LGG	NaN	NaN	codel	2
LGG-277	NaN	NaN	Astrocytoma	G2	LGG	NaN	NaN	non-codel	3
LGG-278	NaN	NaN	Oligoastrocytoma	G2	LGG	NaN	NaN	codel	2
LGG-280	NaN	NaN	Oligoastrocytoma	G2	LGG	NaN	NaN	non-codel	3
LGG-282	NaN	NaN	Oligoastrocytoma	G3	LGG	NaN	NaN	codel	2
LGG-285	NaN	NaN	Oligoastrocytoma	G2	LGG	NaN	NaN	non-codel	2
LGG-286	NaN	NaN	Oligodendroglioma	G2	LGG	NaN	NaN	non-codel	1
LGG-288	NaN	NaN	Oligoastrocytoma	G3	LGG	NaN	NaN	codel	1
LGG-289	NaN	NaN	Oligodendroglioma	G2	LGG	NaN	NaN	codel	2
LGG-293	NaN	NaN	Oligoastrocytoma	G2	LGG	NaN	NaN	non-codel	3
LGG-295	NaN	NaN	Oligoastrocytoma	G3	LGG	NaN	NaN	codel	3
LGG-296	NaN	NaN	Oligodendroglioma	G2	LGG	NaN	NaN	codel	2
LGG-297	NaN	NaN	Oligoastrocytoma	G2	LGG	NaN	NaN	non-codel	3
LGG-298	NaN	NaN	Oligoastrocytoma	G3	LGG	NaN	NaN	codel	3
LGG-303	NaN	NaN	Oligodendroglioma	G2	LGG	NaN	NaN	codel	1
LGG-304	NaN	NaN	Oligodendroglioma	G2	LGG	NaN	NaN	codel	3
LGG-305	NaN	NaN	Oligodendroglioma	G2	LGG	NaN	NaN	codel	3
LGG-306	NaN	NaN	Astrocytoma	G3	LGG	NaN	NaN	non-codel	3
LGG-307	NaN	NaN	Oligoastrocytoma	G3	LGG	NaN	NaN	codel	2
LGG-308	NaN	NaN	Oligodendroglioma	G2	LGG	NaN	NaN	codel	3
LGG-310	NaN	NaN	Oligoastrocytoma	G2	LGG	NaN	NaN	codel	2
LGG-311	NaN	NaN	Astrocytoma	G2	LGG	NaN	NaN	non-codel	3
LGG-313	NaN	NaN	Oligoastrocytoma	G2	LGG	NaN	NaN	non-codel	2
LGG-314	NaN	NaN	Oligoastrocytoma	G2	LGG	NaN	NaN	non-codel	1
LGG-315	NaN	NaN	Oligodendroglioma	G2	LGG	NaN	NaN	codel	2
LGG-316	NaN	NaN	Oligodendroglioma	G3	LGG	NaN	NaN	codel	1
LGG-320	NaN	NaN	Oligoastrocytoma	G2	LGG	NaN	NaN	codel	1
LGG-321	NaN	NaN	Oligoastrocytoma	G2	LGG	NaN	NaN	non-codel	2
LGG-325	NaN	NaN	Oligoastrocytoma	G2	LGG	NaN	NaN	codel	3
LGG-326	NaN	NaN	Oligoastrocytoma	G2	LGG	NaN	NaN	codel	1
LGG-327	NaN	NaN	Oligoastrocytoma	G2	LGG	NaN	NaN	non-codel	3
LGG-330	NaN	NaN	Oligoastrocytoma	G3	LGG	NaN	NaN	codel	3

LGG-331	NaN	NaN	Oligodendroglioma	G2	LGG	NaN	NaN	codel	2
LGG-333	NaN	NaN	Oligoastrocytoma	G3	LGG	NaN	NaN	codel	2
LGG-334	NaN	NaN	Oligoastrocytoma	G2	LGG	NaN	NaN	non-codel	2
LGG-337	NaN	NaN	Oligoastrocytoma	G2	LGG	NaN	NaN	codel	1
LGG-338	NaN	NaN	Oligoastrocytoma	G3	LGG	NaN	NaN	non-codel	3
LGG-341	NaN	NaN	Oligoastrocytoma	G3	LGG	NaN	NaN	codel	2
LGG-343	NaN	NaN	Oligoastrocytoma	G2	LGG	NaN	NaN	non-codel	2
LGG-344	NaN	NaN	Oligodendroglioma	G2	LGG	NaN	NaN	codel	1
LGG-345	NaN	NaN	Oligoastrocytoma	G3	LGG	NaN	NaN	codel	3
LGG-346	NaN	NaN	Astrocytoma	G3	LGG	NaN	NaN	non-codel	2
LGG-348	NaN	NaN	Oligoastrocytoma	G2	LGG	NaN	NaN	codel	1
LGG-350	NaN	NaN	Oligoastrocytoma	G2	LGG	NaN	NaN	codel	1
LGG-351	NaN	NaN	Oligoastrocytoma	G2	LGG	NaN	NaN	non-codel	1
LGG-352	NaN	NaN	Oligodendroglioma	G2	LGG	NaN	NaN	codel	2
LGG-354	NaN	NaN	Oligoastrocytoma	G3	LGG	NaN	NaN	non-codel	1
LGG-355	NaN	NaN	Astrocytoma	G3	LGG	NaN	NaN	codel	1
LGG-357	NaN	NaN	Oligoastrocytoma	G2	LGG	NaN	NaN	codel	1
LGG-359	NaN	NaN	Oligodendroglioma	G2	LGG	NaN	NaN	codel	3
LGG-360	NaN	NaN	Oligodendroglioma	G2	LGG	NaN	NaN	codel	3
LGG-361	NaN	NaN	Oligoastrocytoma	G2	LGG	NaN	NaN	codel	1
LGG-363	NaN	NaN	Oligoastrocytoma	G2	LGG	NaN	NaN	non-codel	2
LGG-365	NaN	NaN	Oligoastrocytoma	G3	LGG	NaN	NaN	codel	3
LGG-367	NaN	NaN	Oligoastrocytoma	G2	LGG	NaN	NaN	codel	3
LGG-371	NaN	NaN	Astrocytoma	G3	LGG	NaN	NaN	non-codel	1
LGG-373	NaN	NaN	Oligoastrocytoma	G3	LGG	NaN	NaN	codel	2
LGG-374	NaN	NaN	Oligoastrocytoma	G2	LGG	NaN	NaN	non-codel	3
LGG-375	NaN	NaN	Oligoastrocytoma	G2	LGG	NaN	NaN	non-codel	2
LGG-377	NaN	NaN	Oligodendroglioma	G3	LGG	NaN	NaN	codel	1
LGG-380	NaN	NaN	Oligoastrocytoma	G3	LGG	NaN	NaN	codel	1
LGG-383	NaN	NaN	Oligoastrocytoma	G2	LGG	NaN	NaN	codel	3
LGG-385	NaN	NaN	Oligoastrocytoma	G3	LGG	NaN	NaN	codel	2
LGG-387	NaN	NaN	Oligoastrocytoma	G3	LGG	NaN	NaN	codel	2
LGG-388	NaN	NaN	Oligoastrocytoma	G2	LGG	NaN	NaN	codel	1
LGG-391	NaN	NaN	Oligoastrocytoma	G2	LGG	NaN	NaN	non-codel	1
LGG-394	NaN	NaN	Oligodendroglioma	G3	LGG	NaN	NaN	codel	3
LGG-395	NaN	NaN	Oligoastrocytoma	G3	LGG	NaN	NaN	codel	1
LGG-396	NaN	NaN	Oligoastrocytoma	G2	LGG	NaN	NaN	codel	1
LGG-492	NaN	NaN	Oligoastrocytoma	G2	LGG	NaN	NaN	codel	2
LGG-500	NaN	NaN	Oligoastrocytoma	G2	LGG	NaN	NaN	non-codel	1
LGG-506	NaN	NaN	Oligoastrocytoma	G2	LGG	NaN	NaN	non-codel	1
LGG-515	NaN	NaN	Oligoastrocytoma	G2	LGG	NaN	NaN	codel	3

LGG-516	NaN	NaN	Oligoastrocytoma	G3	LGG	NaN	NaN	non-codel	2
LGG-518	NaN	NaN	Astrocytoma	G3	LGG	NaN	NaN	non-codel	3
LGG-519	NaN	NaN	Oligoastrocytoma	G2	LGG	NaN	NaN	non-codel	1
LGG-520	NaN	NaN	Oligodendroglioma	G2	LGG	NaN	NaN	codel	2
LGG-525	NaN	NaN	Oligodendroglioma	G2	LGG	NaN	NaN	codel	2
LGG-527	NaN	NaN	Oligoastrocytoma	G2	LGG	NaN	NaN	codel	3
LGG-532	NaN	NaN	Oligoastrocytoma	G3	LGG	NaN	NaN	non-codel	3
LGG-533	NaN	NaN	Oligoastrocytoma	G2	LGG	NaN	NaN	non-codel	1
LGG-537	NaN	NaN	Oligoastrocytoma	G2	LGG	NaN	NaN	non-codel	2
LGG-545	NaN	NaN	Oligoastrocytoma	G2	LGG	NaN	NaN	non-codel	1
LGG-547	NaN	NaN	Oligodendroglioma	G2	LGG	NaN	NaN	codel	2
LGG-550	NaN	NaN	Oligoastrocytoma	G3	LGG	NaN	NaN	codel	3
LGG-552	NaN	NaN	Astrocytoma	G3	LGG	NaN	NaN	non-codel	2
LGG-558	NaN	NaN	Oligoastrocytoma	G2	LGG	NaN	NaN	non-codel	1
LGG-561	NaN	NaN	Oligoastrocytoma	G3	LGG	NaN	NaN	codel	2
LGG-563	NaN	NaN	Oligodendroglioma	G2	LGG	NaN	NaN	codel	2
LGG-565	NaN	NaN	Oligoastrocytoma	G2	LGG	NaN	NaN	codel	3
LGG-566	NaN	NaN	Oligoastrocytoma	G2	LGG	NaN	NaN	codel	3
LGG-570	NaN	NaN	Oligoastrocytoma	G2	LGG	NaN	NaN	codel	2
LGG-572	NaN	NaN	Astrocytoma	G3	LGG	NaN	NaN	codel	3
LGG-573	NaN	NaN	Oligoastrocytoma	G2	LGG	NaN	NaN	codel	1
LGG-574	NaN	NaN	Oligodendroglioma	G2	LGG	NaN	NaN	non-codel	1
LGG-576	NaN	NaN	Oligoastrocytoma	G2	LGG	NaN	NaN	codel	1
LGG-579	NaN	NaN	Oligoastrocytoma	G2	LGG	NaN	NaN	codel	1
LGG-581	NaN	NaN	Oligoastrocytoma	G2	LGG	NaN	NaN	codel	2
LGG-582	NaN	NaN	Oligodendroglioma	G2	LGG	NaN	NaN	codel	2
LGG-585	NaN	NaN	Astrocytoma	G2	LGG	NaN	NaN	non-codel	3
LGG-587	NaN	NaN	Oligodendroglioma	G3	LGG	NaN	NaN	codel	3
LGG-589	NaN	NaN	Oligoastrocytoma	G2	LGG	NaN	NaN	non-codel	2
LGG-590	NaN	NaN	Oligoastrocytoma	G2	LGG	NaN	NaN	codel	1
LGG-591	NaN	NaN	Astrocytoma	G3	LGG	NaN	NaN	non-codel	1
LGG-593	NaN	NaN	Oligodendroglioma	G3	LGG	NaN	NaN	codel	1
LGG-594	NaN	NaN	Oligoastrocytoma	G3	LGG	NaN	NaN	non-codel	2
LGG-597	NaN	NaN	Oligoastrocytoma	G2	LGG	NaN	NaN	codel	1
LGG-600	NaN	NaN	Oligoastrocytoma	G3	LGG	NaN	NaN	codel	3
LGG-601	NaN	NaN	Astrocytoma	G3	LGG	NaN	NaN	non-codel	3
LGG-604	NaN	NaN	Oligoastrocytoma	G2	LGG	NaN	NaN	codel	2
LGG-607	NaN	NaN	Oligodendroglioma	G2	LGG	NaN	NaN	codel	3
LGG-609	NaN	NaN	Oligoastrocytoma	G2	LGG	NaN	NaN	non-codel	2
LGG-610	NaN	NaN	Oligoastrocytoma	G2	LGG	NaN	NaN	non-codel	3
LGG-612	NaN	NaN	Oligodendroglioma	G2	LGG	NaN	NaN	codel	2

LGG-613	NaN	NaN	Oligoastrocytoma	G2	LGG	NaN	NaN	non-codel	1
LGG-614	NaN	NaN	Oligodendroglioma	G2	LGG	NaN	NaN	codel	3
LGG-616	NaN	NaN	Oligoastrocytoma	G2	LGG	NaN	NaN	codel	3
LGG-620	NaN	NaN	Oligodendroglioma	G2	LGG	NaN	NaN	codel	3
LGG-622	NaN	NaN	Oligoastrocytoma	G2	LGG	NaN	NaN	non-codel	2
LGG-624	NaN	NaN	Oligoastrocytoma	G3	LGG	NaN	NaN	non-codel	2
LGG-625	NaN	NaN	Oligoastrocytoma	G2	LGG	NaN	NaN	non-codel	2
LGG-626	NaN	NaN	Astrocytoma	G3	LGG	NaN	NaN	codel	2
LGG-630	NaN	NaN	Oligodendroglioma	G2	LGG	NaN	NaN	codel	3
LGG-631	NaN	NaN	Oligoastrocytoma	G2	LGG	NaN	NaN	non-codel	1
LGG-632	NaN	NaN	Oligoastrocytoma	G2	LGG	NaN	NaN	codel	2
LGG-634	NaN	NaN	Oligodendroglioma	G3	LGG	NaN	NaN	codel	2
LGG-637	NaN	NaN	Oligodendroglioma	G2	LGG	NaN	NaN	codel	1
LGG-639	NaN	NaN	Oligoastrocytoma	G2	LGG	NaN	NaN	codel	1
LGG-642	NaN	NaN	Oligodendroglioma	G3	LGG	NaN	NaN	codel	2
LGG-647	NaN	NaN	Oligoastrocytoma	G2	LGG	NaN	NaN	non-codel	3
LGG-648	NaN	NaN	Astrocytoma	G2	LGG	NaN	NaN	codel	3
LGG-651	NaN	NaN	Oligodendroglioma	G2	LGG	NaN	NaN	codel	3
LGG-658	NaN	NaN	Oligodendroglioma	G3	LGG	NaN	NaN	codel	3

Supplementary Table 3: Subject wise MGMT promoter status, clinical variables, and group membership for each fold of the cross-validation.

Subject ID	Age	Gender	Histology	Grade	TCGA Data Collection	IDH mutation Status	1p/19q co-deletion status	MGMT promoter status	Cross-validation group
TCGA-02-0003	50	male	glioblastoma	G4	TCGA-GBM	WT	non-codel	Unmethylated	2
TCGA-02-0006	56	female	glioblastoma	G4	TCGA-GBM	WT	non-codel	Unmethylated	2
TCGA-02-0009	61	female	glioblastoma	G4	TCGA-GBM	WT	non-codel	Unmethylated	2
TCGA-02-0011	18	female	glioblastoma	G4	TCGA-GBM	WT	non-codel	Methylated	2
TCGA-02-0027	33	female	glioblastoma	G4	TCGA-GBM	WT	non-codel	Unmethylated	2
TCGA-02-0033	54	male	glioblastoma	G4	TCGA-GBM	WT	non-codel	Methylated	1
TCGA-02-0034	60	male	glioblastoma	G4	TCGA-GBM	WT	non-codel	Unmethylated	1
TCGA-02-0037	74	female	glioblastoma	G4	TCGA-GBM	WT	non-codel	Unmethylated	1
TCGA-02-0046	61	male	glioblastoma	G4	TCGA-GBM	WT	non-codel	Methylated	1
TCGA-02-0047	78	male	glioblastoma	G4	TCGA-GBM	WT	non-codel	Unmethylated	1
TCGA-02-0060	66	female	glioblastoma	G4	TCGA-GBM	WT	non-codel	Methylated	2
TCGA-02-0064	50	male	glioblastoma	G4	TCGA-GBM	WT	non-codel	Methylated	3
TCGA-02-0069	31	female	glioblastoma	G4	TCGA-GBM	WT	non-codel	Methylated	2
TCGA-02-0075	63	male	glioblastoma	G4	TCGA-GBM	WT	non-codel	Methylated	2
TCGA-02-0086	45	female	glioblastoma	G4	TCGA-GBM	WT	non-codel	Unmethylated	2

TCGA-02-0102	42	male	glioblastoma	G4	TCGA-GBM	WT	non-codel	Unmethylated	1
TCGA-06-0119	81	female	glioblastoma	G4	TCGA-GBM	WT	non-codel	Methylated	2
TCGA-06-0122	84	female	glioblastoma	G4	TCGA-GBM	WT	non-codel	Unmethylated	2
TCGA-06-0128	66	male	glioblastoma	G4	TCGA-GBM	Mutant	non-codel	Methylated	3
TCGA-06-0129	30	male	glioblastoma	G4	TCGA-GBM	Mutant	non-codel	Methylated	1
TCGA-06-0133	64	male	glioblastoma	G4	TCGA-GBM	WT	non-codel	Unmethylated	2
TCGA-06-0137	63	female	glioblastoma	G4	TCGA-GBM	WT	non-codel	Unmethylated	2
TCGA-06-0142	81	male	glioblastoma	G4	TCGA-GBM	WT	non-codel	Unmethylated	1
TCGA-06-0143	58	male	glioblastoma	G4	TCGA-GBM	WT	non-codel	Unmethylated	1
TCGA-06-0145	53	female	glioblastoma	G4	TCGA-GBM	WT	non-codel	Methylated	1
TCGA-06-0147	51	female	glioblastoma	G4	TCGA-GBM	WT	non-codel	Methylated	2
TCGA-06-0148	76	male	glioblastoma	G4	TCGA-GBM	WT	non-codel	Unmethylated	1
TCGA-06-0881	50	male	glioblastoma	G4	TCGA-GBM	WT	non-codel	Unmethylated	1
TCGA-06-1806	47	male	glioblastoma	G4	TCGA-GBM	WT	non-codel	Unmethylated	2
TCGA-06-2570	21	female	glioblastoma	G4	TCGA-GBM	Mutant	non-codel	Methylated	1
TCGA-06-5408	54	female	glioblastoma	G4	TCGA-GBM	WT	non-codel	Unmethylated	3
TCGA-06-5412	78	female	glioblastoma	G4	TCGA-GBM	WT	non-codel	Methylated	2
TCGA-06-5413	67	male	glioblastoma	G4	TCGA-GBM	WT	non-codel	Unmethylated	1
TCGA-06-5417	45	female	glioblastoma	G4	TCGA-GBM	Mutant	NA	Methylated	3
TCGA-06-6389	49	female	glioblastoma	G4	TCGA-GBM	Mutant	non-codel	Methylated	3
TCGA-12-0829	75	male	glioblastoma	G4	TCGA-GBM	WT	non-codel	Methylated	2
TCGA-12-1093	66	female	glioblastoma	G4	TCGA-GBM	WT	non-codel	Unmethylated	1
TCGA-12-1598	75	female	glioblastoma	G4	TCGA-GBM	WT	non-codel	Methylated	3
TCGA-12-1601	NaN	NA	NA	NA	TCGA-GBM	WT	NA	Unmethylated	2
TCGA-12-1602	58	male	glioblastoma	G4	TCGA-GBM	WT	non-codel	Methylated	2
TCGA-12-3650	46	male	glioblastoma	G4	TCGA-GBM	WT	non-codel	Unmethylated	3
TCGA-14-0789	54	male	glioblastoma	G4	TCGA-GBM	WT	non-codel	Methylated	2
TCGA-14-1456	23	male	glioblastoma	G4	TCGA-GBM	Mutant	non-codel	Unmethylated	3
TCGA-14-1794	59	male	glioblastoma	G4	TCGA-GBM	WT	non-codel	Unmethylated	2
TCGA-14-1829	57	male	glioblastoma	G4	TCGA-GBM	WT	non-codel	Unmethylated	2
TCGA-14-3477	38	female	glioblastoma	G4	TCGA-GBM	WT	non-codel	Unmethylated	3
TCGA-19-1390	63	female	glioblastoma	G4	TCGA-GBM	WT	non-codel	Methylated	1
TCGA-19-1789	69	female	glioblastoma	G4	TCGA-GBM	WT	non-codel	Methylated	2
TCGA-19-1791	82	female	glioblastoma	G4	TCGA-GBM	WT	non-codel	Unmethylated	1
TCGA-19-2620	70	male	glioblastoma	G4	TCGA-GBM	WT	non-codel	Methylated	3
TCGA-19-2624	51	male	glioblastoma	G4	TCGA-GBM	WT	non-codel	Unmethylated	1
TCGA-19-2631	74	female	glioblastoma	G4	TCGA-GBM	WT	non-codel	Methylated	3
TCGA-19-5953	58	male	glioblastoma	G4	TCGA-GBM	WT	non-codel	Methylated	1
TCGA-19-5954	72	female	glioblastoma	G4	TCGA-GBM	WT	non-codel	Methylated	3

TCGA-19-5958	56	male	glioblastoma	G4	TCGA-GBM	WT	non-codel	Unmethylated	1
TCGA-27-1830	57	male	glioblastoma	G4	TCGA-GBM	WT	non-codel	Unmethylated	2
TCGA-27-1835	53	female	glioblastoma	G4	TCGA-GBM	WT	non-codel	Methylated	1
TCGA-27-1836	33	female	glioblastoma	G4	TCGA-GBM	WT	non-codel	Methylated	1
TCGA-27-1838	59	female	glioblastoma	G4	TCGA-GBM	WT	non-codel	Unmethylated	3
TCGA-76-4925	76	male	glioblastoma	G4	TCGA-GBM	WT	non-codel	Methylated	2
TCGA-76-4926	68	male	glioblastoma	G4	TCGA-GBM	WT	non-codel	Unmethylated	3
TCGA-76-4927	58	male	glioblastoma	G4	TCGA-GBM	WT	NA	Unmethylated	2
TCGA-76-4928	85	female	glioblastoma	G4	TCGA-GBM	WT	non-codel	Methylated	1
TCGA-76-4929	76	female	glioblastoma	G4	TCGA-GBM	WT	non-codel	Methylated	3
TCGA-76-4931	70	female	glioblastoma	G4	TCGA-GBM	WT	non-codel	Unmethylated	3
TCGA-76-4932	50	female	glioblastoma	G4	TCGA-GBM	WT	NA	Methylated	3
TCGA-76-4934	66	female	glioblastoma	G4	TCGA-GBM	WT	non-codel	Methylated	1
TCGA-76-4935	52	female	glioblastoma	G4	TCGA-GBM	WT	non-codel	Methylated	2
TCGA-76-6191	57	male	glioblastoma	G4	TCGA-GBM	WT	non-codel	Unmethylated	3
TCGA-76-6192	74	male	glioblastoma	G4	TCGA-GBM	WT	non-codel	Unmethylated	2
TCGA-76-6193	78	male	glioblastoma	G4	TCGA-GBM	WT	non-codel	Unmethylated	2
TCGA-76-6280	57	male	glioblastoma	G4	TCGA-GBM	WT	non-codel	Methylated	1
TCGA-76-6282	63	male	glioblastoma	G4	TCGA-GBM	WT	non-codel	Unmethylated	2
TCGA-76-6285	64	female	glioblastoma	G4	TCGA-GBM	WT	non-codel	Unmethylated	3
TCGA-76-6286	60	male	glioblastoma	G4	TCGA-GBM	WT	non-codel	Unmethylated	1
TCGA-76-6656	66	male	glioblastoma	G4	TCGA-GBM	WT	non-codel	Methylated	3
TCGA-76-6657	74	male	glioblastoma	G4	TCGA-GBM	WT	non-codel	Methylated	2
TCGA-76-6661	54	male	glioblastoma	G4	TCGA-GBM	WT	non-codel	Unmethylated	3
TCGA-76-6662	58	male	glioblastoma	G4	TCGA-GBM	WT	non-codel	Unmethylated	1
TCGA-76-6663	44	female	glioblastoma	G4	TCGA-GBM	WT	non-codel	Unmethylated	3
TCGA-76-6664	49	female	glioblastoma	G4	TCGA-GBM	WT	non-codel	Methylated	3
TCGA-CS-4938	31	female	astrocytoma	G2	TCGA-LGG	Mutant	non-codel	Unmethylated	3
TCGA-CS-4941	67	male	astrocytoma	G3	TCGA-LGG	WT	non-codel	Methylated	1
TCGA-CS-4942	44	female	astrocytoma	G3	TCGA-LGG	Mutant	non-codel	Unmethylated	1
TCGA-CS-4943	37	male	astrocytoma	G3	TCGA-LGG	Mutant	non-codel	Methylated	3
TCGA-CS-4944	50	male	astrocytoma	G2	TCGA-LGG	Mutant	non-codel	Methylated	2
TCGA-CS-5390	47	female	oligodendroglioma	G2	TCGA-LGG	Mutant	codel	Methylated	2
TCGA-CS-5393	39	male	astrocytoma	G3	TCGA-LGG	Mutant	non-codel	Methylated	2
TCGA-CS-5394	40	male	astrocytoma	G3	TCGA-LGG	Mutant	non-codel	Methylated	1
TCGA-CS-5395	43	male	oligodendroglioma	G2	TCGA-LGG	WT	non-codel	Unmethylated	1
TCGA-CS-5396	53	female	oligodendroglioma	G3	TCGA-LGG	Mutant	codel	Methylated	3
TCGA-CS-5397	54	female	astrocytoma	G3	TCGA-LGG	WT	non-codel	Unmethylated	2
TCGA-CS-6186	58	male	oligoastrocytoma	G3	TCGA-LGG	WT	non-codel	Unmethylated	1

TCGA-CS-6188	48	male	astrocytoma	G3	TCGA-LGG	WT	non-codel	Unmethylated	2
TCGA-CS-6290	31	male	astrocytoma	G3	TCGA-LGG	Mutant	non-codel	Methylated	1
TCGA-CS-6665	51	female	astrocytoma	G3	TCGA-LGG	Mutant	non-codel	Methylated	3
TCGA-CS-6666	22	male	astrocytoma	G3	TCGA-LGG	Mutant	non-codel	Methylated	2
TCGA-CS-6667	39	female	astrocytoma	G2	TCGA-LGG	Mutant	non-codel	Methylated	1
TCGA-CS-6668	57	female	oligodendroglioma	G2	TCGA-LGG	Mutant	codel	Methylated	1
TCGA-CS-6669	26	female	oligodendroglioma	G2	TCGA-LGG	WT	non-codel	Unmethylated	3
TCGA-DU-5849	48	male	oligodendroglioma	G2	TCGA-LGG	Mutant	codel	Methylated	1
TCGA-DU-5851	40	female	oligoastrocytoma	G3	TCGA-LGG	Mutant	non-codel	Unmethylated	3
TCGA-DU-5852	61	female	oligoastrocytoma	G3	TCGA-LGG	WT	non-codel	Methylated	3
TCGA-DU-5853	29	male	oligoastrocytoma	G2	TCGA-LGG	Mutant	non-codel	Methylated	2
TCGA-DU-5854	57	female	astrocytoma	G3	TCGA-LGG	WT	non-codel	Unmethylated	2
TCGA-DU-5855	49	female	oligoastrocytoma	G3	TCGA-LGG	Mutant	non-codel	Methylated	2
TCGA-DU-5871	37	female	oligoastrocytoma	G2	TCGA-LGG	Mutant	non-codel	Methylated	3
TCGA-DU-5872	43	female	oligoastrocytoma	G2	TCGA-LGG	Mutant	non-codel	Methylated	2
TCGA-DU-5874	62	female	oligodendroglioma	G2	TCGA-LGG	Mutant	codel	Methylated	3
TCGA-DU-6395	31	male	oligoastrocytoma	G2	TCGA-LGG	Mutant	non-codel	Methylated	1
TCGA-DU-6397	45	male	oligodendroglioma	G3	TCGA-LGG	Mutant	codel	Methylated	2
TCGA-DU-6399	54	male	oligodendroglioma	G2	TCGA-LGG	Mutant	non-codel	Methylated	1
TCGA-DU-6400	66	female	oligodendroglioma	G2	TCGA-LGG	Mutant	codel	Methylated	3
TCGA-DU-6401	31	female	oligodendroglioma	G2	TCGA-LGG	Mutant	non-codel	Methylated	3
TCGA-DU-6404	24	female	oligodendroglioma	G3	TCGA-LGG	WT	non-codel	Unmethylated	3
TCGA-DU-6405	51	female	astrocytoma	G3	TCGA-LGG	WT	non-codel	Methylated	3
TCGA-DU-6407	35	female	oligodendroglioma	G2	TCGA-LGG	Mutant	non-codel	Methylated	3
TCGA-DU-6408	23	female	oligodendroglioma	G3	TCGA-LGG	Mutant	non-codel	Methylated	1
TCGA-DU-7008	41	female	oligodendroglioma	G2	TCGA-LGG	Mutant	non-codel	Methylated	1
TCGA-DU-7010	58	female	astrocytoma	G3	TCGA-LGG	Mutant	non-codel	Methylated	3
TCGA-DU-7013	59	male	astrocytoma	G3	TCGA-LGG	WT	non-codel	Unmethylated	1
TCGA-DU-7015	41	female	oligodendroglioma	G2	TCGA-LGG	Mutant	non-codel	Methylated	2
TCGA-DU-7018	57	female	oligodendroglioma	G3	TCGA-LGG	Mutant	codel	Methylated	1
TCGA-DU-7019	39	male	oligoastrocytoma	G3	TCGA-LGG	Mutant	non-codel	Methylated	1
TCGA-DU-7294	53	female	oligodendroglioma	G2	TCGA-LGG	Mutant	codel	Methylated	1
TCGA-DU-7298	38	female	astrocytoma	G3	TCGA-LGG	Mutant	non-codel	Methylated	2
TCGA-DU-7299	33	male	astrocytoma	G3	TCGA-LGG	Mutant	non-codel	Methylated	3
TCGA-DU-7300	53	female	oligodendroglioma	G3	TCGA-LGG	Mutant	codel	Methylated	3
TCGA-DU-7301	53	male	oligodendroglioma	G2	TCGA-LGG	Mutant	non-codel	Methylated	3
TCGA-DU-7302	48	female	oligodendroglioma	G3	TCGA-LGG	Mutant	codel	Methylated	1
TCGA-DU-7304	43	male	oligoastrocytoma	G3	TCGA-LGG	Mutant	non-codel	Methylated	3
TCGA-DU-7306	67	male	oligoastrocytoma	G2	TCGA-LGG	Mutant	non-codel	Methylated	1

TCGA-DU-7309	41	female	oligodendroglioma	G3	TCGA-LGG	Mutant	non-codel	Methylated	3
TCGA-DU-8158	57	female	astrocytoma	G3	TCGA-LGG	WT	non-codel	Unmethylated	3
TCGA-DU-8162	61	female	oligoastrocytoma	G3	TCGA-LGG	WT	non-codel	Unmethylated	1
TCGA-DU-8164	51	male	oligodendroglioma	G2	TCGA-LGG	Mutant	codel	Methylated	1
TCGA-DU-8165	60	female	oligodendroglioma	G3	TCGA-LGG	WT	non-codel	Unmethylated	1
TCGA-DU-8166	29	female	oligoastrocytoma	G2	TCGA-LGG	Mutant	non-codel	Methylated	2
TCGA-DU-8167	69	female	oligoastrocytoma	G2	TCGA-LGG	Mutant	non-codel	Methylated	3
TCGA-DU-8168	55	female	oligodendroglioma	G3	TCGA-LGG	Mutant	codel	Methylated	3
TCGA-DU-A5TP	33	male	astrocytoma	G3	TCGA-LGG	Mutant	non-codel	Methylated	2
TCGA-DU-A5TR	51	male	oligoastrocytoma	G2	TCGA-LGG	Mutant	non-codel	Methylated	2
TCGA-DU-A5TS	42	male	oligodendroglioma	G2	TCGA-LGG	Mutant	non-codel	Methylated	2
TCGA-DU-A5TT	70	male	oligodendroglioma	G3	TCGA-LGG	WT	non-codel	Methylated	2
TCGA-DU-A5TU	62	female	astrocytoma	G2	TCGA-LGG	Mutant	non-codel	Methylated	1
TCGA-DU-A5TW	33	female	astrocytoma	G3	TCGA-LGG	Mutant	non-codel	Methylated	2
TCGA-DU-A5TY	46	female	astrocytoma	G3	TCGA-LGG	WT	non-codel	Methylated	2
TCGA-DU-A6S2	37	female	oligodendroglioma	G2	TCGA-LGG	Mutant	codel	Methylated	2
TCGA-DU-A6S3	60	male	oligodendroglioma	G2	TCGA-LGG	Mutant	codel	Methylated	3
TCGA-DU-A6S6	35	female	oligoastrocytoma	G2	TCGA-LGG	Mutant	codel	Methylated	1
TCGA-DU-A6S7	27	female	astrocytoma	G3	TCGA-LGG	Mutant	non-codel	Methylated	2
TCGA-DU-A6S8	74	female	oligodendroglioma	G3	TCGA-LGG	Mutant	codel	Methylated	2
TCGA-FG-5963	23	male	astrocytoma	G3	TCGA-LGG	WT	non-codel	Unmethylated	2
TCGA-FG-5964	62	male	oligodendroglioma	G2	TCGA-LGG	Mutant	codel	Methylated	1
TCGA-FG-6688	59	female	astrocytoma	G3	TCGA-LGG	WT	non-codel	Methylated	2
TCGA-FG-6689	30	male	astrocytoma	G2	TCGA-LGG	Mutant	non-codel	Methylated	3
TCGA-FG-6690	70	male	oligodendroglioma	G2	TCGA-LGG	Mutant	non-codel	Methylated	2
TCGA-FG-6691	23	female	astrocytoma	G2	TCGA-LGG	Mutant	non-codel	Unmethylated	3
TCGA-FG-6692	63	male	oligodendroglioma	G3	TCGA-LGG	WT	non-codel	Methylated	1
TCGA-FG-7634	28	male	oligodendroglioma	G2	TCGA-LGG	Mutant	codel	Methylated	1
TCGA-FG-7637	49	male	oligoastrocytoma	G2	TCGA-LGG	Mutant	non-codel	Methylated	1
TCGA-FG-8189	33	female	oligodendroglioma	G2	TCGA-LGG	Mutant	non-codel	Methylated	3
TCGA-FG-A4MT	27	female	oligodendroglioma	G2	TCGA-LGG	Mutant	non-codel	Methylated	2
TCGA-FG-A4MU	58	male	oligoastrocytoma	G3	TCGA-LGG	WT	non-codel	Methylated	1
TCGA-FG-A6IZ	60	male	oligodendroglioma	G2	TCGA-LGG	Mutant	codel	Methylated	3
TCGA-FG-A6J1	44	female	oligodendroglioma	G2	TCGA-LGG	Mutant	codel	Methylated	2
TCGA-FG-A713	74	female	oligoastrocytoma	G2	TCGA-LGG	Mutant	codel	Methylated	3
TCGA-FG-A87N	37	female	astrocytoma	G3	TCGA-LGG	Mutant	non-codel	Methylated	3
TCGA-HT-7468	30	male	oligodendroglioma	G3	TCGA-LGG	Mutant	codel	Methylated	1
TCGA-HT-7469	30	male	oligodendroglioma	G3	TCGA-LGG	WT	non-codel	Methylated	1
TCGA-HT-7471	37	female	oligodendroglioma	G3	TCGA-LGG	Mutant	codel	Methylated	2

TCGA-HT-7472	38	male	oligodendroglioma	G2	TCGA-LGG	Mutant	non-codel	Methylated	1
TCGA-HT-7473	28	male	oligoastrocytoma	G2	TCGA-LGG	Mutant	non-codel	Unmethylated	3
TCGA-HT-7475	67	male	oligoastrocytoma	G3	TCGA-LGG	Mutant	non-codel	Methylated	3
TCGA-HT-7476	26	male	astrocytoma	G2	TCGA-LGG	Mutant	non-codel	Methylated	1
TCGA-HT-7478	36	male	astrocytoma	G2	TCGA-LGG	Mutant	non-codel	Unmethylated	1
TCGA-HT-7481	39	male	oligodendroglioma	G2	TCGA-LGG	Mutant	codel	Methylated	2
TCGA-HT-7602	21	male	oligodendroglioma	G2	TCGA-LGG	Mutant	non-codel	Methylated	2
TCGA-HT-7603	29	male	oligodendroglioma	G2	TCGA-LGG	Mutant	non-codel	Methylated	2
TCGA-HT-7605	38	male	oligodendroglioma	G2	TCGA-LGG	Mutant	codel	Methylated	3
TCGA-HT-7606	30	female	astrocytoma	G2	TCGA-LGG	Mutant	non-codel	Unmethylated	1
TCGA-HT-7608	61	male	oligoastrocytoma	G2	TCGA-LGG	Mutant	codel	Methylated	2
TCGA-HT-7616	75	male	oligodendroglioma	G3	TCGA-LGG	Mutant	codel	Methylated	3
TCGA-HT-7680	32	female	astrocytoma	G2	TCGA-LGG	WT	non-codel	Unmethylated	3
TCGA-HT-7684	58	male	oligoastrocytoma	G3	TCGA-LGG	Mutant	non-codel	Methylated	3
TCGA-HT-7686	29	female	astrocytoma	G3	TCGA-LGG	Mutant	non-codel	Methylated	3
TCGA-HT-7690	29	male	oligoastrocytoma	G3	TCGA-LGG	Mutant	non-codel	Methylated	3
TCGA-HT-7692	43	male	oligoastrocytoma	G2	TCGA-LGG	Mutant	codel	Methylated	1
TCGA-HT-7693	51	female	oligodendroglioma	G2	TCGA-LGG	Mutant	non-codel	Methylated	1
TCGA-HT-7694	60	male	oligodendroglioma	G3	TCGA-LGG	Mutant	codel	Methylated	2
TCGA-HT-7695	29	female	oligodendroglioma	G2	TCGA-LGG	Mutant	codel	Methylated	1
TCGA-HT-7854	62	male	astrocytoma	G2	TCGA-LGG	WT	non-codel	Unmethylated	3
TCGA-HT-7855	39	male	astrocytoma	G3	TCGA-LGG	Mutant	non-codel	Methylated	2
TCGA-HT-7856	35	male	oligodendroglioma	G3	TCGA-LGG	Mutant	codel	Methylated	2
TCGA-HT-7860	60	female	astrocytoma	G3	TCGA-LGG	WT	non-codel	Methylated	2
TCGA-HT-7874	41	female	oligodendroglioma	G3	TCGA-LGG	Mutant	codel	Methylated	1
TCGA-HT-7877	20	female	oligodendroglioma	G2	TCGA-LGG	Mutant	codel	Methylated	3
TCGA-HT-7879	31	male	oligoastrocytoma	G3	TCGA-LGG	Mutant	non-codel	Methylated	1
TCGA-HT-7880	30	male	oligoastrocytoma	G2	TCGA-LGG	Mutant	non-codel	Methylated	3
TCGA-HT-7882	66	male	oligodendroglioma	G3	TCGA-LGG	WT	non-codel	Methylated	2
TCGA-HT-7884	44	female	astrocytoma	G2	TCGA-LGG	Mutant	non-codel	Methylated	1
TCGA-HT-7902	30	female	oligoastrocytoma	G2	TCGA-LGG	Mutant	non-codel	Methylated	3
TCGA-HT-8010	64	female	oligodendroglioma	G2	TCGA-LGG	Mutant	codel	Methylated	3
TCGA-HT-8013	37	female	oligoastrocytoma	G2	TCGA-LGG	Mutant	non-codel	Methylated	1
TCGA-HT-8015	21	male	astrocytoma	G2	TCGA-LGG	WT	non-codel	Unmethylated	1
TCGA-HT-8018	40	female	oligoastrocytoma	G2	TCGA-LGG	Mutant	non-codel	Methylated	3
TCGA-HT-8019	34	female	oligodendroglioma	G3	TCGA-LGG	WT	non-codel	Unmethylated	1
TCGA-HT-8105	54	male	oligodendroglioma	G3	TCGA-LGG	Mutant	codel	Methylated	3
TCGA-HT-8106	53	male	astrocytoma	G3	TCGA-LGG	Mutant	non-codel	Methylated	1
TCGA-HT-8107	62	male	oligodendroglioma	G2	TCGA-LGG	WT	non-codel	Methylated	2

TCGA-HT-8108	26	female	oligodendroglioma	G2	TCGA-LGG	Mutant	non-codel	Methylated	1
TCGA-HT-8111	32	male	oligoastrocytoma	G3	TCGA-LGG	Mutant	non-codel	Methylated	2
TCGA-HT-8113	49	female	oligodendroglioma	G2	TCGA-LGG	Mutant	non-codel	Methylated	3
TCGA-HT-8114	36	male	oligoastrocytoma	G3	TCGA-LGG	Mutant	non-codel	Methylated	2
TCGA-HT-8558	29	female	oligodendroglioma	G2	TCGA-LGG	WT	non-codel	Unmethylated	2
TCGA-HT-8563	30	female	astrocytoma	G3	TCGA-LGG	Mutant	non-codel	Unmethylated	3
TCGA-HT-8564	47	male	astrocytoma	G3	TCGA-LGG	WT	non-codel	Unmethylated	2
TCGA-HT-A4DS	55	female	astrocytoma	G3	TCGA-LGG	WT	non-codel	Unmethylated	2
TCGA-HT-A5R5	33	female	oligodendroglioma	G2	TCGA-LGG	Mutant	non-codel	Methylated	2
TCGA-HT-A5RB	24	male	astrocytoma	G2	TCGA-LGG	Mutant	non-codel	Methylated	1
TCGA-HT-A5RC	70	female	astrocytoma	G3	TCGA-LGG	WT	non-codel	Unmethylated	2
TCGA-HT-A616	36	female	astrocytoma	G2	TCGA-LGG	Mutant	non-codel	Methylated	3
TCGA-HT-A61A	20	female	oligodendroglioma	G2	TCGA-LGG	Mutant	non-codel	Methylated	3
TCGA-HT-A61B	NaN	NaN	NaN	NaN	TCGA-LGG	Mutant	non-codel	Methylated	2
W1_19961025	NaN	NaN	NaN	NaN	NaN	NaN	NaN	Unmethylated	2
W10_19970429	NaN	NaN	NaN	NaN	NaN	NaN	NaN	Methylated	1
W12_19970620	NaN	NaN	NaN	NaN	NaN	NaN	NaN	Unmethylated	3
W13_19970822	NaN	NaN	NaN	NaN	NaN	NaN	NaN	Unmethylated	3
W16_19971015	NaN	NaN	NaN	NaN	NaN	NaN	NaN	Unmethylated	1
W18_19971110	NaN	NaN	NaN	NaN	NaN	NaN	NaN	Methylated	1
W2_19961101	NaN	NaN	NaN	NaN	NaN	NaN	NaN	Methylated	3
W20_19970516	NaN	NaN	NaN	NaN	NaN	NaN	NaN	Unmethylated	1
W21_19980105	NaN	NaN	NaN	NaN	NaN	NaN	NaN	Unmethylated	2
W22_19980102	NaN	NaN	NaN	NaN	NaN	NaN	NaN	Methylated	1
W29_19980521	NaN	NaN	NaN	NaN	NaN	NaN	NaN	Unmethylated	3
W30_19980608	NaN	NaN	NaN	NaN	NaN	NaN	NaN	Methylated	2
W31_19980629	NaN	NaN	NaN	NaN	NaN	NaN	NaN	Unmethylated	3
W32_19980701	NaN	NaN	NaN	NaN	NaN	NaN	NaN	Methylated	3
W33_19980704	NaN	NaN	NaN	NaN	NaN	NaN	NaN	Methylated	3
W34_19980713	NaN	NaN	NaN	NaN	NaN	NaN	NaN	Unmethylated	2
W36_19980714	NaN	NaN	NaN	NaN	NaN	NaN	NaN	Unmethylated	1
W38_19980910	NaN	NaN	NaN	NaN	NaN	NaN	NaN	Methylated	2
W39_19980919	NaN	NaN	NaN	NaN	NaN	NaN	NaN	Methylated	1
W5_19961211	NaN	NaN	NaN	NaN	NaN	NaN	NaN	Unmethylated	3
W54_20000902	NaN	NaN	NaN	NaN	NaN	NaN	NaN	Unmethylated	3
W7_19961218	NaN	NaN	NaN	NaN	NaN	NaN	NaN	Methylated	1
W9_19970410	NaN	NaN	NaN	NaN	NaN	NaN	NaN	Unmethylated	3